CELLULAR AND MOLECULAR CONTROL OF SKELETON FORMATION IN FISH: INSIGHTS FROM OSTEOBLAST ABLATION AND FUNCTIONAL CHARACTERIZATION OF LRP5 AND SOST

BERND WILLEMS

(*Diplombiologe*, University of Cologne)

A THESIS SUBMITTED FOR THE DEGREE OF PHILOSOPHIAE DOCTOR (Ph.D.)

DEPARTMENT OF BIOLOGICAL SCIENCES

NATIONAL UNIVERSITY OF SINGAPORE

July 2011

Acknowledgements

Completion of this thesis would not have been possible without tremendous help and support from a variety of people.

First of all I would like to thank Assoc. Prof. Christoph Winkler for giving me the opportunity to pursue the research project in his laboratory as well as for his wonderful mentoring and guidance. His helpful advice and our fruitful discussions helped me a lot to accomplish my candidature. I wish him and his family all the best for the future.

Thanks to all my dear lab mates for the support and the help and the wonderful atmosphere we had throughout the years. I wish them good luck and hope that they stay how they are. I thank Martin for being a great colleague/flatmate/friend and Petra who completed “the lunch bunch” for the great time and a great deal of philosophical and scientific discussion.

Thanks to all collaborators, especially Dr. Ann Huysseune. With her contributions she added a lot of value to my project.

I would like to express my gratitude to the National University of Singapore and the Department of Biological Sciences for my admission into the graduate programme and the generous scholarship. Thanks also for creating an excellent environment and for providing all the resources for successful research. Thanks in particular to Ms. Reena Devi and Ms. Priscilla Li for administrative support as well as Mr. Subhas Balan and Mr. Zeng Qing Hua for taking great care of our fish.

I would also like to extend my gratitude to the Republic of Singapore and its decision making bodies for creating and maintaining this wonderful country in the heart of Southeast Asia which has not only been an excellent place for scientific work but also a great warm and welcoming home away from home for the last four years.

Of course, my friends from inside and outside the University in Singapore, Germany and elsewhere have contributed their part to the unique experience; I thank them all for the wonderful times we spent together and I hope we will manage to keep in touch.

Above all, I thank my family, my brother and my parents, who taught me curiosity form the day I made my first steps and who encouraged me to pursue a scientific career. Their love and support made it possible to go this way.

Thank You all.

Publications

The content of this thesis is described in the following publications:

Willems B, Renn J and Winkler C (2011).

Conditional ablation of osteoblasts in medaka.

Under revision with *Developmental Biology*.

Willems B, Huysseune A, Renn J, Witten E and Winkler C (2011).

Overlapping expression of Lrp5 and its putative inhibitor Sost during brain and cranial skeleton development in zebrafish.

Submitted to *MOD Gene Expression Patterns*.

Willems B, Huysseune A, Renn J, Witten E and Winkler C (2011).

A role for the Wnt co-receptor Lrp5 in morphogenesis of the craniofacial skeleton.

Prepared for submission to *PLoS ONE*

Conference contributions

In the course of my candidature I had been given the chance to present my research as follows:

15th Biological Science Graduate Congress, December 15-17, 2010, Kuala Lumpur, Malaysia:

Poster: Conditional ablation of osteoblasts in Medaka. **Willems B.**, Renn J., Winkler C.W.

(awarded with **price for 2nd best poster** in category Cell Biology and Biochemistry)

Singapore Zebrafish Symposium 2010, September 16, 2010, Singapore, Singapore:

Poster: Lrp5 and its putative inhibitor SOST are required for development of the zebrafish cranial skeleton. **Willems B.**, Renn J., Winkler C.W.

43rd Annual Meeting for the Japanese Society of Developmental Biologists (JSDB), June 20-23, 2010, Kyoto, Japan:

Poster: Lrp5 and its putative inhibitor SOST are required for development of the zebrafish cranial skeleton. **Willems B.**, Renn J., Winkler C.W.

14th Biological Science Graduate Congress, December 10-12, 2009, Bangkok, Thailand:

Oral: Lrp5 and its putative inhibitor Sclerostin are required for development of the zebrafish cranial skeleton AND osx:cfp-ntr transgenic medaka as a model to study osteoblast ablation/regeneration. **Willems B.**, Renn J., Winkler C.W.

6th European Zebrafish Genetics and Development Meeting, July 15-19, 2009, Rome, Italy:

Poster: Lrp5 and its putative inhibitor SOST are required for development of the zebrafish cranial skeleton. **Willems B.**, Renn J., Winkler C.W.

13th Biological Science Graduate Congress, December 10-12, 2008, Singapore, Singapore:

Poster: Fish as a model for human bone disease: Focusing on Wnt signaling. **Willems B.**, Renn J., Winkler C.W.

(awarded with **price for best poster** in category Cell Biology and Biochemistry)

Table of Contents

Summary

A structure common to all vertebrate species is their axial skeleton, which is composed of calcified extracellular matrix deposited by bone forming cells (osteoblasts). In this thesis, I used two laboratory fish models, medaka (*Oryzias latipes*) and zebrafish (*Danio rerio*), to gain better understanding of the cellular and molecular processes involved in skeletal development.

To examine the role of osteoblasts in development of the vertebral column, I created a transgenic *osx:CFP-NTR* medaka line which enables conditional ablation of this cell lineage upon antibiotic treatment. Ablation of a substantial number of osteoblasts, which was evident by reduced reporter expression, enhanced apoptosis in the respective regions and reduced marker gene expression, led to reduced bone mass in the cranial skeleton and the vertebral spines. In contrast, vertebral bodies were found partially fused as a consequence of osteoblast ablation. Thus, I propose an additional function for osteoblasts as growth restricting border cells in development of the segmentally organized vertebral bodies.

In the course of vertebrate development, cranial neural crest cells (CNCCs) undergo epithelial to mesenchymal transition (EMT), delaminate from the neural plate border and migrate in distinct mesenchymal streams to invade the respective cranial regions where they eventually differentiate to form the craniofacial skeleton. Canonical Wnt signaling is one of the essential cascades implicated in this process. Here I show that the frizzled co-receptor low-density-lipoprotein (LDL) receptor-related protein 5 (Lrp5) plays a crucial role in CNCC development and morphogenesis of the cranial skeleton. While Morpholino mediated knock-down of *lrp5* does not affect induction of CNCC, it leads to reduced proliferation of premigratory CNCCs. Additionally, CNCC migration is disturbed as ectopic cells are found in the dorsal neuroepithelium. These defects eventually result in craniofacial skeleton malformations. Interestingly, knock-down of Sost, a putative inhibitor of Lrp5 leads to similar defects suggesting that Wnt signaling levels need to be tightly balanced. To date both factors have mainly been associated with bone metabolism in man and mammals. This is the first report about an involvement in early morphogenetic processes, which might represent a teleost specific function.

List of Figures

List of Tables:

List of Abbreviations:

aa	amino acid
ALC	Alizarin Complexone
AO	Acridine Orange
AP	alkaline phosphatase
APC	adenomatosis polyposis coli
ba	branchial arch
bHLH	basic Helix-Loop-Helix
BMP	Bone morphogenic protein
bp	basepair
br	branchial
BrdU	Bromodeoxyuridine
BSA	bovine serum albumine
cb	ceratobranchial
Cbfa1	Core binding factor a1
Ccnd1	Cyclin D1
cDNA	copy desoxyribonucleinazid
CFP	Cyan fluorescent protein
ch	ceratohyal
CNCC	Cranial Neural Crest Cell
DAB	3,3'-Diaminobenzidine
Dkk	Dickkopf
DIG	Digoxigenin
Dlx2a	Distal-less homeobox 2a
DMSO	dimethylsulfatoxide
DNA	deoxyribonucleic acid
dNTP	deoxynucleosidtriphosphate
dot	days of treatment
dpf	days post fertilisation
dpt	days post treatment
Dsh	Dishevelled
EGF	epidermal growth factor
EMT	Epithelial to mesenchymal transition
Fgf	fibroblast growth factor
Fli1	Friend's leukemia inhibiting factor1
FLU	Fluorescein
Foxd3	Forkhead box d3
Fz	Frizzled
GFP	Green fluorescent protein
GSK3β	Glycogen synthase kinase3β
h	hour
hpf	hours post fertilization
hy	hyoid
Lef1	Lymphoid enhancer-binding factor1
LP	Longpass
Lrp	low density lipoptrotein (LDL) receptor related protein
mc	Meckel's cartilage
md	mandibular
MHB	midbrain-hindbrain boundary
ml	milliliter
mg	milligram
mM	milliMol
µl	microliter
µg	microgram
µM	microMol
Mo	Morpholino oligonucleotide
mRNA	messenger RNA
Mtz	Metronidazole
n	number of specimen/experiment
NCC	Neural Crest Cell
NTR	Nitroreductase
Osc	Osteocalcin
Osx	Osterix
OPPG	osteoporosis pseudoglioma syndrome
PBS	phosphate buffered saline
PBST	phosphate buffered saline + 0.1% Tween-20
PCR	polymerase chain reaction
PFA	paraformaldehyde
pH3	phosphorylated Histone 3
PSM	presomitic mesoderm
RNA	ribonucleic acid
Runx2	Runt-related transcription factor 2
SB	sodium borate
siRNA	small interfering RNA
sFRPs	secreted Frizzled related proteins
SOST	Sclerostin
Sox10	SRY-related HMG-box 10
ss	somite stage
SSC	sodium chloride/sodium citrat
SSCT	SSC + Tween-20
TUNEL	TdT-mediated dUTP-biotin nick end labeling
V	Volt
VEGF	vascular endothelial growth factor
WIF-1	Wnt inhibitory facor-1
WT	wild-type

1. INTRODUCTION

1.1. Osteogenesis

The process of bone development is called osteogenesis. The skeleton derives from three distinct lineages. The somites give rise to the axial skeleton consisting of the vertebral column and the ribs (Tam and Trainor, 1995). The limb skeleton is generated by the lateral plate mesoderm (Cohn and Tickle, 1996) whereas the cranial neural crest is the origin of craniofacial bones such as skull and maxilla (Bronner-Fraser, 1994; Noden, 1991).

Two mechanisms of bone development are distinguishable: Intramembranous and endochondral ossification. Intramembranous ossification, which occurs in the skull for instance, is the direct conversion of mesenchymal tissue into bone. The second process is more complex and comprises an intermediate step of cartilage formation which acts as a mould for subsequent ossification (Horton, 1990; Erlebacher et al., 1995). In more recent vertebrates all mesoderm-derived bones (vertebral column and limbs) are formed by this process.

Mesenchymal cells proliferate as a consequence of interaction with epithelial cells which release differentiation factors such as bone morphogenic protein (BMP)-signals (St Amand et al., 2000). They condensate into compact nodules and subsequently differentiate to osteoblasts. This process is promoted by Core binding factor a1 (Cbfa1) also called Runt-related transcription factor 2 (Runx2) which activates other osteoblast-specific genes encoding extracellular matrix-proteins (Komori et al., 1997). Another key regulator of osteoblast differentiation is the transcription factor Osterix (Osx, Nakashima et al., 2002). By secretion of a collagen-proteoglycan osteoid matrix and embedding of calcium, osteoblasts manage to assemble bone mass. Some oteoblasts become trapped into the calcified matrix and are subsequently called osteocytes. The surrounding mesenchymal cells form a membrane called periosteum. Inside this membrane further osteoblasts deposit matrix to form additional layers of bone.

The skeleton is in an incessant process of remodeling also called bone homeostasis. Bone mass is constantly added by osteoblasts and simultaneously degraded by osteoclasts. These cells derive from macrophage precursors and are translocated via blood vessels to the bones. They solubilize the bone matrix by pumping H^+-Ions out of the cell and thereby acidifying the surrounding material. Osteoblast and osteoclast formation as well as activity is in a sensitive equilibrium.

1.2. Zebrafish and medaka as models for bone research

Most of the previous descriptions are based on experiments in mouse and chicken. More recently, however, zebrafish and medaka have become important models for bone research. It has been shown that key mechanisms and regulators of bone development are highly conserved among vertebrate species including teleosts and tetrapods (reviewed by Renn et al., 2006). The two types of bone development namely intracellular and endochondral/perichondral ossification are present in fish (Langille and Hall, 1987; Bird and Mabee, 2003) as well as the bone remodeling process resulting from the interplay between osteoblasts and osteoclasts (Witten et al., 2000 and 2001). Zebrafish but not medaka seems to develop cellular bone with osteocytes trapped inside the matrix (Ekanayake and Hall, 1987; Witten et al., 2001). The similarities on the cellular level are also reflected on the molecular level. Genes involved in osteogenesis in fish are characterized by a high homology in amino acid sequence and expression pattern with their tetrapod counterparts (reviewed by Renn et al., 2006).

Thus, fish represent an excellent tool for basic research on issues of skeletal development and disease. This is because both medaka and zebrafish provide numerous advantages for this type of research: They frequently produce high numbers of offspring which develop rapidly and allow reproducibility of experimental settings and real-time analysis of development. The transparency of the embryos together with the development of new imaging strategies allow direct *in vivo* observation of developmental processes at the cellular level. The genomes of both species are

almost completely sequenced and publicly available. Although strategies of forward genetics are still challenging, both species are accessible for tools of genetic modification enabling generation of transgenic fish with tissue specific expression of reporters or functional proteins. A growing number of transgenic lines are maintained by the global research community.

1.3. The development of the vertebral column

During embryonic development of mammals and birds, the vertebral column is assembled by populations of mesenchymal cells that migrate around the notochord. They originate from the sclerotome which is part of the embryonic mesodermal somites (Christ et al.,2004). Subsequently, these mesenchymal cells undergo differentiation into chondrocytes and bone forming cells (osteoblasts) and eventually assemble the mineralized vertebrae by endochondral ossification. The vertebra contains the centrum, as well as the neural and hemal arches. Any failure in osteoblast differentiation results in the absence of mineralized vertebrae (Chan et al., 2007; Nakashima et al., 2002). Prior to calcification, a transient cartilage scaffold composed of segmented vertebral bodies (centra) is formed that follows the spatial information established by the somitic boundaries. Experiments in mouse mutants with defects in genes that are crucial for somitogenesis showed that such embryos fail to develop a segmented vertebral column (Chan et al., 2007; Kanda et al., 2007).

In teleosts in contrast, the vertebrae are directly calcified without involvement of a cartilage scaffold, except in the anterior most neural arches that constitute the Weberian apparatus in some species, e.g. zebrafish (Bird and Mabee, 2003). A central role for the notochord in centra mineralization was proposed by Fleming and colleagues (Fleming et al., 2004), who showed that the zebrafish notochord, when isolated and cultured, is capable of secreting mineralized matrix on its own without involvement of recruited osteoblasts. These authors also demonstrated that local ablation of notochord cells resulted in the absence of centra mineralization in this region. For

Atlantic salmon it was reported that notochord cells juxtaposed to forming centra exert Alkaline Phosphatase activity, which is a marker for mineral secreting activity (Grotmol et al., 2005). Inohaya and colleagues (Inohaya et al., 2007) showed that a mineralized chordal centrum is formed from the notochordal sheath, an acellular layer that surrounds the notochord, before differentiation of sclerotome derived osteoblasts. However, they proposed osteoblasts to be the main source of subsequent mineralization.

The teleost vertebral column seems to be pre-patterned independently from somites as suggested by observations made in *fused-somite* (*tbx24*) mutant zebrafish (Nikaido et al., 2002). These mutants are characterized by a disrupted anteroposterior identity of their somites and therefore an unorganized sclerotome pattern. Nevertheless, the centra still organize in a normal fashion while neural and hemal arches grow severely disorganized (van Eeden et al., 1996). This might suggest an instructive property of the notochord with possible contribution from the floor plate (Inohaya et al., 2010). However, the mechanism by which the notochord establishes a possible metameric pattern independently from somitic boundaries, yet in absolute congruence, is unknown.

Osteoblasts are involved in the formation of vertebral bodies in medaka (Inohaya et al., 2007). Sclerotome derived cells around the notochordal sheath differentiate into osteoblasts and secrete extracellular bone matrix to build up the perichordal centrum, the bony layer around the chordal centrum. Osteoblast differentiation also occurs in the intervertebral region. Hence, at least two classes of osteoblasts are hypothesized (Inohaya et al., 2007). Class I cells are osteoblasts at the anterior and posterior edges of the centra, which secrete bone matrix and thereby facilitate rostrocaudal growth of the vertebral bodies. Class II cells in contrast are involved in deposition of the extra elastica matrix and thereby prevent mineralization of the intervertebral regions (Inohaya et al., 2007). However, to date osteoblasts have not been shown to be indispensable for the formation of vertebral bodies in medaka.

Osterix (Osx) is a zinc finger transcription factor and key regulator for the differentiation of pre-

osteoblasts to osteoblasts, first shown in mouse (Nakashima et al., 2002). In medaka, *osx* is expressed in early osteoblasts preceding bone mineralization (Renn and Winkler, 2009). *osx* transgenic expression was observed in advance of mineralization of the neural and hemal arches and at the edges but not the core of the chordal centrum. Therefore, whether and how *osterix*-expressing osteoblasts contribute to the segmentation of vertebral bodies remains unclear.

1.4. Cranial neural crest cells and their derivatives in the craniofacial skeleton

"Of all the major vertebrate embryonic tissues, the neural crest is perhaps the most fascinating." This quotation by Langeland and Kimmel (1997) reflects the astonishing potential of different cell fates this lineage is able to give rise to. Therefore, it is sometimes even called "the fourth germ layer". Mostly depending on the region where the neural crest cells (NCCs) will migrate to, their fate will be to differentiate into different cells and tissues such as neurons of the enteric and peripheral nervous system, endocrine and paraendocrine derivatives and pigment cells. Cells from the cranial neural crest (CNCCs) mostly give rise to facial cartilage, bone and connective tissue. NCCs are specified at the neural plate-epidermis boundary upon induction by several paracrine factors such as BMPs, Wnts and FGFs. These factors trigger expression of a set of transcription factors (TFs) called the "neural plate border specifiers" (Meulemans and Bronner-Fraser, 2004). Their function is to prevent the region from becoming neural plate or epidermis and to activate expression of another set of TFs called "neural crest specifiers". Committed NCCs undergo an epithelial to mesenchymal transition (EMT) and delaminate from the neural plate. Subsequently CNCCs migrate ventrally from regions anterior to hindbrain rhombomere 8 into the pharyngeal arches and the frontonasal process. Three characteristic major streams can thereby be distinguished (Fig. 1AB; reviewed by Kimmel et al., 2001). 1. The mandibular stream: CNCCs from the midbrain and rhombomere 1 and 2 migrate to the first pharyngeal arch (Fig. 1A, blue arrows). These cells will eventually form the most anterior jaw bones, the Meckel's Cartilage and

the palatoquadrate (Fig. 1C, blue elements). 2. The hyoid stream: Cells adjacent to rhombomere 4 migrate into the second pharyngeal arch and will later establish the basihyal, ceratohyal and the hyosymplectic (Fig. 1A, red arrows; C, red elements). 3. The branchial streams: The 3rd till 6th pharyngeal arches are invaded by CNCCs from rhombomeres 6 till 8 (only few in the 7th). Each of these five arches will give rise to one of the five ceratobranchials (Fig. 1A, green/yellow arrows; C, green/yellow elements). The mechanisms behind these complex processes are not yet understood. However, numerous publications indicate an important role of canonical Wnt signaling in this process (see chapter 1.5.).

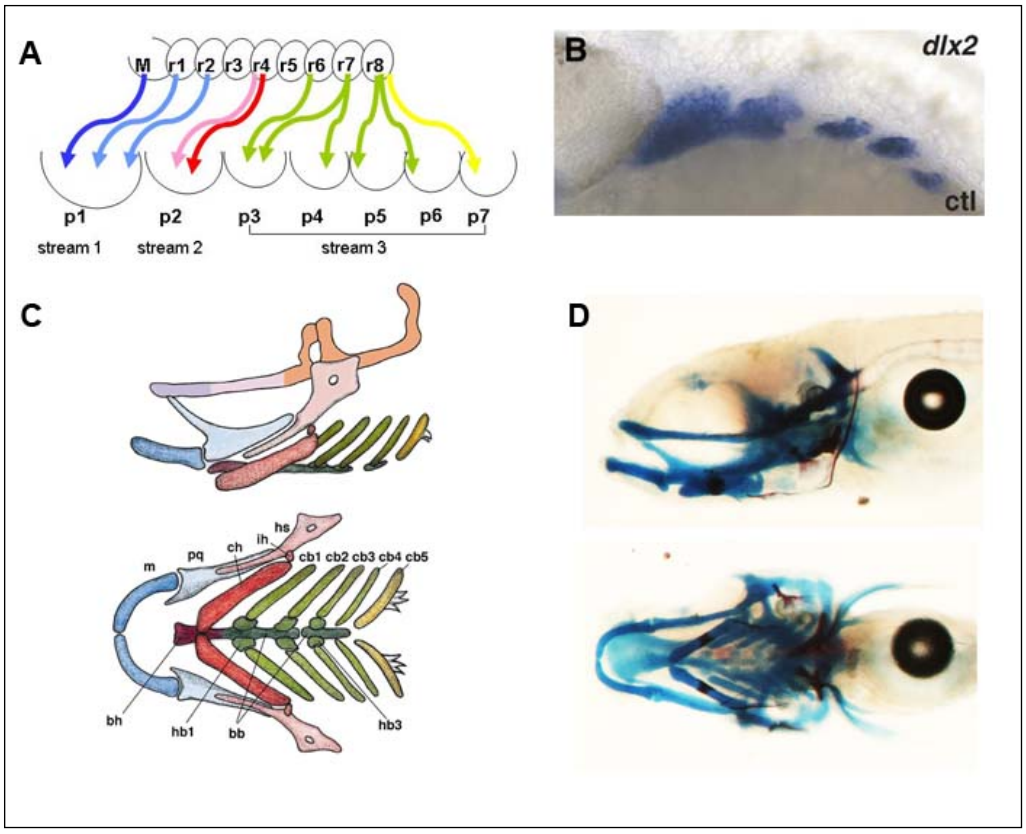

Fig. 1. Cranial neural crest cells and their craniofacial derivatives. (A) Three major streams of migrating CNCCs can be distinguished (drawing courtesy by Cheah Siew Hong). (B) *dlx2a* serves as marker for migrating CNCCs and enables to visualize cells in pharyngeal arches (from Lister et al., 2006). (C) Lateral and ventral schematic drawings of cranial skeleton, the color code matches the originating cells shown in A (from Kimmel et al., 2001). (D) Lateral and ventral views of larvae at 7 dpf stained with Alcian blue (cartilage)/Alizarin red (bone). *Abbreviations*: bb, basibranchial; bh, basihyal; cb, ceratobranchial; ch, ceratohyal; hb, hypobranchial; hs, hyosymplectic; ih, interhyal; M, midbrain; m, Meckel's; pq, palatoquadrate; p, pharyngeal arch;. R, rhombomere. Anterior is to the left in all pictures.

1.4. The molecular basis of canonical Wnt signaling

The family of Wnt molecules comprises several secreted lipid-modified glycoproteins (Willert et al., 2003). So far, 20 different *wnt* homologues have been described; 15 of them are also present in zebrafish (reviewed by Cadigan and Nusse, 2006). They are involved in numerous biological processes in embryonic development (Cadigan and Nusse, 1997; Wodarz and Nusse, 1998; Logan and Nusse, 2004) as well as in mature cell-cell signaling (Pinto and Clevers, 2005; Lowry et al., 2005; Reya et al., 2003; Willert et al., 2003). Reduced activity of Wnt signaling is also associated with osteoporosis (Koay and Brown, 2005; Levasseur et al., 2005). There are several pathways for Wnt signaling (Veeman et al., 2003; Fanto and McNeill, 2004; Kohn and Moon, 2005) but the most important is signaling through β-catenin which is also called the "canonical Wnt pathway" (Fig. 2). Secreted Wnt molecules bind to the seven-transmembrane-span-protein Frizzled (Fz; Vinson et al., 1989). Together with Lrp5 or 6 they form a ternary complex on the cell surface (He et al., 2004; Pinson et al., 2000; Tamai et al., 2000; Wehrli et al., 2000; Zorn, 2001). This heterotrimeric complex leads to activation of Dishevelled (Dsh), a cytoplasmic protein that manages to inactivate the β-catenin destruction complex (Klingensmith et al., 1994).

The detailed mechanism how the Wnt signal is transduced to inactivate the β-catenin destruction complex is not fully understood until now. This complex consists of GSK3β, axin and the tumor suppressor adenomatosis polyposis coli (APC; McCrea et al., 1991; Huber et al., 1997; Wieschaus and Riggleman, 1987).

In the absence of Wnt, GSK3β phosphorylates β-catenin for ubiquitin-mediated degradation in the proteasome (Aberle et al. 1997). In the activated state of Wnt signaling, β-catenin remains stable (Hinck et al. 1994; Van Leeuwen et al. 1994) and translocates into the nucleus to form a complex with the HMG-Box containing transcription factors of the TCF-LEF-family. These factors together with β-catenin eventually activate transcription of Wnt-target genes (Molenaar et al.,

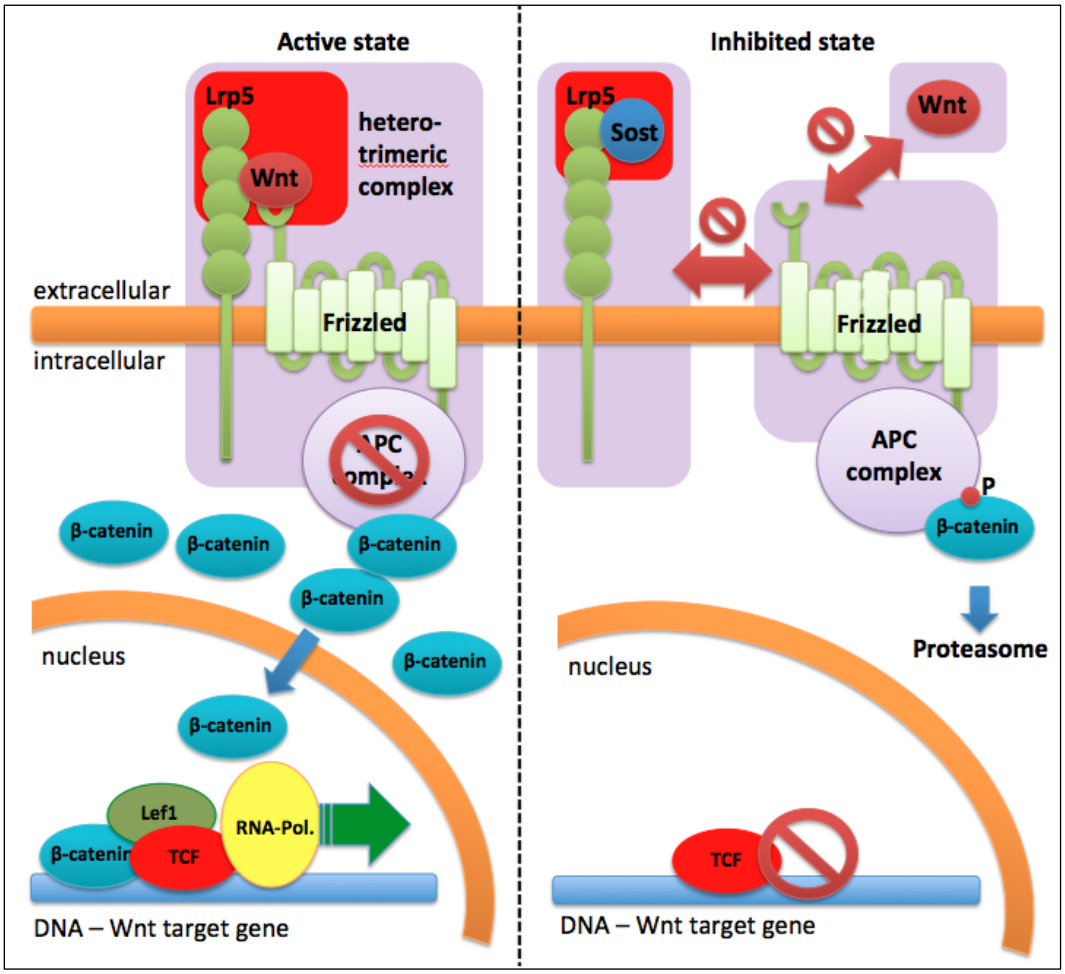

Fig. 2. Schematic representation of canonical Wnt signaling: Left side shows active state by Lrp5 mediated binding of Wnt ligand to Frizzled receptor and the signal transduction pathway. Right side shows Sost mediated inhibition of the pathway (adapted from van Bezooijen et al., 2008).

1996; Korinek et al., 1997; Morin et al., 1997). Regulation of Wnt signaling mostly occurs in the extracellular region. Secreted Frizzled related proteins (sFRPs) as well as Wnt inhibitory factor-1 (WIF-1) molecules both competitively bind to secreted Wnt molecules and therefore disable Wnt binding to Fz (Satoh et al., 2006; St-Arnaud and Moir, 1993). Other secreted inhibitors of Wnt signaling are SOST/sclerostin and Dickkopf (Dkk) (in association with Kremen) that both bind to Lrp5 and 6 and thereby prevent the formation of the heterotrimeric complex of Wnt, Fz and Lrp5/6 (Semenov et al., 2001 and 2005; Li et al., 2002).

1.5 Canonical Wnt signaling in neural crest cells

A number of experiments revealed that canonical Wnt signaling is one of the crucial signal transduction pathways involved in all NCC related processes that take place in the course of development (reviewed by Raible and Ragland, 2005). It was shown that overexpression of several Wnt ligands or activated β-catenin results in expansion of the neural crest in *Xenopus laevis* (Wu et al., 2005 and references therein). In contrast, blocking of Wnt signaling by miss-expression of GSK3β, dominant-negative Wnt8, truncated Tcf3, mutated Dishevelled or Nkd resulted in disruption of neural crest formation. Thus, Wnt signaling is important for induction of NCCs. In zebrafish, Wnt8 Morpholino knock-down blocks early NCC induction and a critical phase for NCC induction has been determined by expression of truncated Tcf under control of an HSP70 heatshock promoter (Lewis et al., 2004). Wnts also regulate proliferation and subsequent delamination of NCCs from the dorsal neuroepithelium (Burstyn-Cohen et al., 2004). A role in migration has also been suggested since $LiCl_2$-mediated GSK3β inhibition prevents cell migration and blocks cell-matrix adhesion in cultured neural crest cells (de Melker et al., 2004). In *Xenopus laevis*, a role for Lrp6 has been suggested for NCC induction since its miss-expression expands the neural crest. Vice versa, excess transcripts of a truncated dominant-negative form of Lrp6 seem to reduce the neural crest (Tamai *et al*., 2000). In contrast, Lrp6 does not seem to have a function for CNCCs in zebrafish as knock-down of this gene affects somitogenesis but does not result in any morphological craniofacial defects (Willems and Gajewski, unpublished; Willems, Diplomathesis, University of Cologne, 2007).

1.6. The Wnt-coreceptor Lrp5 and its putative inhibitory ligand Sost

The single-transmembrane-span-protein Lrp5 together with the closely related Lrp6 forms a new subfamily of low-density lipoprotein (LDL) receptor-related proteins (Nykjaer and Willnow, 2002; Strickland et al., 2002). Arrow is the Drosophila ortholog with a sequence identity of 40%

(Pinson et al., 2000; Tamai et al.,2000; Wehrli et al., 2000). All LDL receptors show structural similarities, which are most prominent in the extracellular portion of the proteins. There are several Cys-rich LDLR binding repeats as well as Cys-rich EGF-repeats with associated spacer domains containing YWTD-propeller motives (Krieger and Herz, 1994). Lrp5 carries five repeats of the PPPSP motif in the intracellular region that are suggested to serve as phosphorylation targets (Zeng et al., 2005). These motives are unique to Lrp5/6 and not found in other receptors of the LDLR family. Lrp5 and 6 serve as co-receptors for Wnt ligands (He et al., 2004; Pinson et al., 2000; Tamai et al., 2000; Wehrli et al., 2000; Zorn, 2001). Recent research on Lrps has led to some new suggestions how the Wnt signal is transduced into inactivation of the β-catenin destruction complex. The Lrp5/6 receptors appear to play a crucial part in this process. It has been shown that the intracellular domain of Lrp5/6 contains Axin2 binding sites (Mao et al., 2001). Thus, binding of Axin might be the trigger for inactivation of the phosphorylation of β-catenin. The binding sites are five reiterated PPPSP motifs mentioned before that need to be phosphorylated for Axin2 recognition (Tamai et al., 2004). A membrane associated form of GSK3β was recently suggested to phosphorylate Lrp5/6 upon stimulation by Fz (Zeng et al., 2005). It was also shown that the intracellular domains of Lrp5/6 alone constitutively activate the pathway suggesting that the extracellular domain exerts a suppressing function (Mao et al., 2001a; Mao et al., 2001b; Liu et al., 2003).

Sost is a secreted ligand that belongs to the family of Cysteine-knot proteins. It was identified as a member of the DAN (differential screening–selected gene aberrant in neuroblastoma) family of glycoproteins (Balemans et al., 2001; Brunkow et al., 2001). Other members of this family have been shown to be BMP antagonists, though in this respect, Sost seems not to be a classical member of this family (van Bezooijen et al., 2004). Sost inhibits Wnt signaling similar to other Dan proteins. In particular, Wise shares high homology with Sost (Ellies et al., 2006). The mechanism how Sost antagonizes Wnt is by binding directly to both Lrp5 and Lrp6 apparently

without competing for binding to Wnt ligands (Li et al., 2005; Semenov et al., 2005; van Bezooijen et al., 2007). One of the three cys-knot loops of Sost carries several positively charged residues, which are predicted to bind to a matching motif with negatively charged residues on the first β-propeller of Lrp5 (Veverka et al., 2009; Weidauer et al., 2009). A predicted Heparin binding site on Sost suggests Heparin mediated surface localization, which might facilitate receptor binding (Veverka et al., 2009).

1.7. The role of Lrp5 and Sost in bone homeostasis of more recent vertebrates

LRP5 appears to play a major role in regulation of bone mass, which is reflected by the finding that mutations in LRP5 are associated with the autosomal recessive osteoporosis-pseudoglioma syndrome (OPPG; Gong et al., 2001). Patients suffering from this syndrome are characterized by an early onset of osteoporosis and therefore high risk of fracture from early childhood on. It was reported in mouse that loss-of-function mutations in *Lrp5* result in reduced proliferation of osteoblast precursors despite normal expression of Cbfa1, a key regulator of osteoblast differentiation (Kato et al., 2002). In contrast, there are several gain of function mutations of *LRP5* that are all located in the first *β*-propeller domain and lead to a high bone mass phenotype (Boyden et al., 2002). The cause of this phenotype was later found to be due to the inability of binding Sost (Li et al., 2005; Semenov et al., 2005).

Patients with loss-of-function mutations in the *SOST* gene suffer from sclerosteosis or van Buchem disease, both progressive sclerosing bone dysplasiae, comparable to gain of function mutations in *LRP5* (Balemans et al., 2001 and 2002).

So far in mammals, no link has been observed between mutations of *LRP5* or *SOST* and severe developmental defects of the craniofacial skeleton. Nonetheless, there are reports about slight cranial bone dysmorphologies in human patients with gain of function mutations in *LRP5*, such as

craniosynostosys (Kwee *et al*., 2005) or a large lobulated torus palatinus and an abnormally thick mandibular ramus already at young age (Boyden *et al*., 2002). Patients suffering from loss-of-function mutations in *SOST* are also characterized by abnormal cranial morphology such as a high forehead and a protruding large chin. However, these traits have been described to appear in a progressive manner over lifetime and do not suggest to be the cause of a developmental malfunction (Balemans *et al.*, 2001).

An earlier report by Yadav et al. (2008) challenged the established idea that LRP5 directly controls bone cells in order to maintain bone mass. These authors presented conclusive evidence that LRP5 exerts its effect on bone mass through regulating biosynthesis of Serotonin in the gut. However, a more recent report (Cui et al, 2010) shows that in mouse osteocyte specific activation of a gain of function variant of Lrp5 leads to high bone mass phenotype in a cell autonomous fashion, thus reverting the attention of Lrp5 function back on bone cells.

A role in craniofacial development of non-mammalian vertebrate species is suggested by the expression pattern of *lrp5* and *lrp6* in Xenopus (Houston and Wylie, 2002). So far, functional studies have only been conducted on *lrp6* in this species (Tamai *et al*., 2000). In the course of my diploma thesis I studied the function of zebrafish *lrp6* which was shown to be indispensable for somitogenesis and trunk development but had no apparent role in craniofacial development (Willems and Gajewski, 2007). Thus, the question about a possible involvement of Lrp5 in zebrafish craniofacial development remained to be answered.

1.8. Aim of the project

The first aim of this project was to investigate the role of osteoblasts for the formation of the teleost vertebral bodies. For this, I generated transgenic medaka fish to express the *nfsB*-gene encoded Nitroreductase (NTR) from Escherichia Coli (Bryant et al., 1991) as a fusion protein with Cyan Fluorescent Protein (CFP) under the control of the *osx*-promoter, which was

characterized earlier in our laboratory (Renn and Winkler, 2009). NTR metabolizes the antibiotic Metronidazole (Mtz) into a DNA-crosslinking cytotoxic product. This approach has been successfully used for cell ablation in various organs in zebrafish, except bone (Curado et al., 2008; Pisharath et al., 2007). By ablating osteoblasts and studying the consequences to the developing larva, I sought to gain new insights into the role of osteoblasts during development of the vertebral column. This study is the first of its kind showing successful application of the nitroreductase cell ablation technique in medaka. Furthermore, it is the first fish model for osteoporosis due to reduced numbers of osteoblasts.

The second aim of the project was to study the function of Lrp5 and Sost during cranial neural crest development in zebrafish. A particular interest was to find out, whether and how these two genes contribute to the formation of the craniofacial skeleton. The functional diversity of Wnt signaling is reflected by a huge set of different ligands (15 Wnts in zebrafish) and receptors (11 Fzs in zebrafish). However, there are only two types of co-receptors (Lrp5 and Lrp6) that are thought to be crucial for the function of canonical Wnt signaling. By knocking-down one of the co-receptors, I intended to abolish Wnt signaling more efficiently than by inhibition of single ligands or receptors. Since Lrp6 has been ruled out to be involved in craniofacial development of zebrafish, it seemed reasonable to analyze the role for Lrp5 in this organism.

The interaction of Sost and Lrp5 has recently become a highly recognized field in bone related research. Due to its inhibitory function in the bone anabolic process and clinical relevance in humans, attempts are being made to target this interaction. By using the experimental advantages of the fish model, such as dose-dependent gene knock-down and dynamic bioimaging, I sought to gain better insight into the function and activities of the two proteins. This might eventually provide clues that could contribute to the overall aim to treat and prevent bone related diseases such as osteoporosis, which have become a major public health concern in our ageing society.

2. MATERIALS AND METHODS

2.1 Materials

2.1.1. Zebrafish and medaka strains and transgenic lines

The medaka OI wild-type strain from the Department of Biological Sciences (DBS) was used as well as transgenic *osx:mCherry* fish (Renn and Winkler 2009). For zebrafish experiments, DBS wild-type fish as well as transgenic *sox10*:GFP (Dutton et al., 2008), *fli1*:EGFP (Lawson and Weinstein, 2002) and TOPdGFP zebrafish (Dorsky et al., 2002) were used. All experiments were performed in accordance with the IACUC protocols of the National University of Singapore (approval numbers 020/08, 014/11).

2.1.2. Morpholino oligonucleotides

For gene knock-down experiments, *lrp5* as well as *sost* splice site Morpholinos were synthesized by Gene Tools (Corvalis, OR). For knock-down of *lrp5,* I designed the "*lrp5*MoUp" Morpholino (5'-AGCTGCTCTTACAGTTTGTAGAGAG-3') to match to the Exon2-Intron2 splice site and the "*lrp5*MoDown" Morpholino (5'-CCTCCTTCATAGCTGCAAAAACAAG-3') to cover the Intron2-Exon3 splice site (see Fig. 16A). A mismatch morpholino with 5 base substitutions "*lrp5*MoUpMM" (5'-AGgTGCTgTTAgAGTTTcTAGAcAG-3') was designed as control. For knock-down of *sost*, the two splice site Morpholinos "*sost*MoUp" (5'-TCACGTTACTTACCATAAGTCCGTG-3') and "*sost*MoDown" (5'-GTTCTGAGGCTCCTGGGAAAGAAAG-3') were designed to match to the splice donor and acceptor site of the only intron in the *sost* gene. Also for *sost* knock-down, a mismatch morpholino with 5 base substitutions "*sost*MoUpMM" (5'-TCACcTTAgTTAgCATAAcTCgGTG-3') was designed as control. Sequence information for p53 control Morpholino (5'-GCGCCATTGCTTTGCAAGAATTG-3') was taken from Robu et

al. (2007). 3 mM stock solutions were prepared by dissolving the lyophilized Morpholinos in 100μl millipore water.

2.1.3. Primers

Primers were designed using the online application Primer3 (v. 0.4.0; http://frodo.wi.mit.edu/primer3/) and synthesized by 1st Base (Singapore). Being delivered in lyophilized condition, primers were dissolved in an appropriate volume of TE buffer to a final concentration of 100 µM. For working solutions, primers were further diluted 1/10 in TE-buffer All used primers are listed in table 2.1.

Table 2.1. List of used primers.

#	Name	Sequence
for subcloning of osx:CFP-NTR (see. 2.3.5.1.)		
1	LinkerBamSmaSalNotA	5'-GATCCCCCGGGAGATACAGTCGACGC-3'
2	LinkerBamSmaSalNotB	5'-GGCCGCGTCGACTGTATCTCCCGGGG-3'
for PCR amplification of riboprobe templates (see 2.3.5.2.)		
3	Lrp5up1	5'-CCATCAAACAGACCTACTACAACCT-3'
4	Lrp5down1	5'-GAATATCATTGACTTGAAGGACGAT-3'
5	Sostup	5'-CCAGATCTCCACCATGCAGGTGTCTCTGGCGCT-3'
6	Sostdown	5'-GGCTCGAGGGTCAGTATGAATTGCTGTTGA-3'
7	crestinup	5'-GCCAAGATGTTCACGCCTAT-3'
8	crestindown	5'-GTTGCATCAAGGTGGTGTTG-3'
for validation of Morpholino mediated knock-down by RT-PCR (see 2.3.5.3.)		
9	Lrp5MoChkup	5'- CAGTGGACTTTCTCTTCTCG-3'
10	Lrp5MoChkdown	5'- GTCTCCGAGTCAGTCCAGTA-3'
11	Lrp5MointronChkdown	5'- CTAAGATTGTGGGTCACAGG-3'
12	SOSTExon1up	5'- TGCTTCAGGGATGTTTCACA-3'
13	SOSTExon2down	5'- CGATTGGTTGTGTTGTCGAG-3'

2.2. Fish treatment

2.2.1. Fish keeping and husbandry

Fish were kept in the department's fish facility. To obtain embryos, fish were kept on a 14h/10h day/night cycle and crossed in mating tanks. Embryos were kept in petri dishes with 1x Danieau's solution (17.4 mM NaCl, 0.21 mM KCl, 0.12 mM $MgSO_4$, 0.18 mM $Ca(NO_3)_2$, 1.5 mM HEPES, pH 7.6). To prevent pigmentation, 0.003% 1-phenyl-2-thiourea (PTU) was added to the medium starting from 8 to 10 hours post fertilization (hpf). Staging was done according to Kimmel et al. (1995).

2.2.2. Morpholino injection

For injections, Morpholino oligonucleotide (Mo) stock solutions were diluted in H_2O with 0.1% Phenol Red. Working solutions were loaded into glass capillaries that were previously prepared with a needle puller (Narishige) to yield a sharp tip. Injection was performed by inserting the needle into the yolk of the embryo at a position slightly underneath the cell. Mo solution was released into the yolk of one- or two-cell stage embryos by means of air pressure supplied from a FemtoJet® Microinjector (Eppendorf).

2.2.3. Mechanical dechorionation of zebrafish

Before fixation, older embryos were mechanically dechorionated to guarantee a straightened body axis for subsequent experiments. Therefore, chorions were carefully opened and removed by means of fine-pointed watchmaker's forceps. Embryos younger than 24 hpf were dechorionated after fixation.

2.2.4. Chemical dechorionation of medaka

To dechorionate embryos before natural hatching, a protocol based on Pronase treatment was carried out (modified from Villalobos et al. 2000). Embryos were incubated in 0.6 mg/ml Pronase® (Boehringer Mannheim, Indianapolis, IN) dissolved in dechorionation buffer (50 mM

glycine, pH 9±0.3, Sigma in 1x Danieau's solution) at 30°C for 3-4 hours. Subsequently, dechorionated embryos were rinsed several times in 1x Danieau's solution. Remaining chorions were removed manually using forceps.

2.2.5. Mtz treatment

For targeted cell ablation, *osx:CFP-NTR* and control medaka were incubated in 10 mM Metronidazole (Sigma) dissolved in Danieau's solution with 0.1% DMSO. Throughout the incubation period, larvae were kept in 6-well plates at 30°C in the dark. Media were replaced once a day. The control larvae were kept in 0.1% DMSO in 1x Danieau's solution.

2.2.6. SU5402 treatment

For SU5402 treatment, zebrafish embryos were manually dechorionated with forceps and placed in 24-well plates. SU5402 stock solution (1.44 mM in DMSO) was dissolved in Danieau's solution to a final concentration of 10µM. Control embryos were kept in the same DMSO concentration (6.9%). Embryos were kept in the solution for 3 hours between 16 hpf (14 somite stage; ss) to 19 hpf (20ss). Subsequently, embryos were rinsed three times in Danieau's solution and fixed in 4% PFA.

2.2.7. Fixation of embryos and larvae

At desired stages, embryos and larvae were fixed in 4% paraformaldehyde (PFA)/phosphate buffered saline (1 M NaCl, 19.5 mM KCl, 59 mM Na_2HPO_4, 11 mM KH_2PO_4) plus 0.1% Tween (PBST) for at least 4 hours or overnight. Subsequently embryos/larvae were washed 3 times for 5 minutes in PBST followed by one wash in methanol and finally storage in methanol at -20°C

2.3. Molecular Biology protocols and applications

2.3.1. RNA extraction

To extract total RNA from zebrafish embryos, the RNeasy-Kit (Qiagen) was used as follows: Around 30 embryos at the desired stage were transferred into a 1.5ml reaction tube and

homogenized with a pestil in 350µl RLT-buffer followed by a centrifugation step. The supernatant was transferred to a new reaction tube and 350µl 70% ethanol were added. The solution was transferred to a spin column and centrifuged at >8,000xg for 15 seconds. The flow through was discarded and after addition of 700µl RW1 buffer a centrifugation was carried out again at >8,000xg for 15 seconds. The flow through was discarded and after addition of 500µl RPE buffer another centrifugation was carried out again at > 8,000xg for 15 seconds. This step was performed twice with a 2 minute centrifugation step before the column was placed into a fresh tube and centrifuged for 2 minutes to discard all traces of liquid. For elution of RNA the column was placed into a new reaction tube and centrifuged 2 times with 30µl RNase-free H_20. To remove traces of genomic DNA 2µl RNase free DNase (Fermentas) were added and the solution was incubated at 37°C for 30 minutes. Subsequently, the RNA was cleaned up by phenol:chloroform extraction.

2.3.2. Phenol:chloroform extraction

Phenol:chloroform extraction was done to remove proteins from nucleic acid solutions. An equal volume of phenol:chloroform was added to the DNA/RNA protein mixture and vigorously vortexed for 30 seconds. It was then centrifuged at 13,000xg for 1 minute. With a glass pasteur pipette, the aqueous phase was transferred into a fresh reaction tube and the organic phase was discarded. Subsequently, an equal volume of chloroform was added to the sample, vortexed for 30 seconds and centrifuged at 13,000xg for 1 minute. Afterwards, the aqueous phase was transferred to a new reaction tube for ethanol precipitation.

2.3.3. Ethanol precipitation

Ethanol precipitation was performed to concentrate the DNA: 1/10 volume 3M NaOAc and 2.5 volumes Ethanol (100%) were added to the solution. The DNA was precipitated for ≥2 hours at -20°C. This was followed by a centrifugation step at 13,000xg for 30 minutes at 4°C. The pellet was washed using 70% ethanol and again centrifuged at 13,000xg for 5 minutes. Then the ethanol

was removed and the pellet was allowed to dry for 5 minutes before it was resuspended in H_20.

2.3.4. cDNA synthesis

cDNA was synthesized from 0.1-5µg extracted and purified total RNA (2.3.1.) using the First Strand cDNA Synthesis Kit (Fermentas). RNA was diluted with H_2O to a volume of 11µl and 1µl of random hexamer primer was added. For annealing the solution was incubated at 70°C for 5 minutes and subsequently chilled on ice to prevent folding of RNA secondary structures. After addition of 4µl 5x reaction buffer, 1µl RNase inhibitor (20 U/µl) and 2µl dNTPs (10 mM) the reaction was incubated at room temperature for 5 minutes. 1ul reverse transcriptase (200U/µl) was added to start the reaction first at room temperature for 10 minutes, then at 42°C for 1h. To stop the reaction, temperature was raised to 70°C for 10 minutes.

2.3.5. Polymerase chain reaction (PCR)

2.3.5.1. General protocol

PCR was carried out to amplify DNA sequences (Mullis et al., 1986). For each reaction 1-100 ng template DNA were used. Furthermore 200 nM primer up, 200 nM primer down, 200 µM desoxy-nucleotide triphosphate (dNTP)-mixture (Fermentas), 1/10 volume 10× reaction buffer (Fermentas) and 0.2µl of Taq DNA Polymerase (Fermentas; 5 units/µl) were added to each reaction. The total volume of the reaction was 25µl.

The reactions were performed in a Veriti^{TM}-96Well Thermal Cycler (Applied Biosystems) or a Tpersonal Thermal Cycler (Biometra) choosing the following conditions: Initial denaturation of DNA took place at 95°C for 5 minutes. At the beginning of a cycle, there were 30 seconds of denaturation at 95°C followed by annealing of the primers for 30 seconds at 55°C (the annealing temperature was adjusted depending on the sequence of the primer used). Extension took place at 72°C for 30 seconds (elongation time was adjusted depending on the expected fragment size; 1 minute/kb). The cycle was repeated 25 times followed by a terminal heat step at 72°C for 7

minutes. The obtained PCR products were then run on an agarose gel.

2.3.5.2. PCR amplification of riboprobe templates

Zebrafish wild-type cDNA was used for riboprobe template cloning. The *lrp5* gene sequence is available at Ensembl (ENSDARG00000006921). According to this sequence, primers "Lrp5up1" and "Lrp5down1" were designed to PCR-amplify a 885 bp fragment. According to a zebrafish *sost* sequence available in Ensembl (ENSDARG00000061259), the full length open reading frame (orf) of *sost* was PCR-amplified with primers "Sostup" and "Sostdown". Crestin antisense probe template was PCR amplified with the primers "crestinup": and "crestindown", which yielded a 802 bp fragment. All other riboprobe templates were provided by colleagues and collaborators.

2.3.5.3. Validation of Morpholino mediated knock-down by RT-PCR

To assess the efficiency of the knock-down approaches at the transcript level, cDNAs from 25 ss wild-type control as well as morphant embryos was used. Correctly spliced transcripts were PCR amplified using the primers "Lrp5MoChkup" and "Lrp5MoChkdown" (Fig. 16A). To amplify transcripts retaining introns due to morpholino mediated splicing deficiency, the primers "Lrp5MoChkup" and "Lrp5MointronChkdown" were used. Likewise, to quantitatively check for correctly spliced *sost* transcripts, the primer combination "SOSTExon1up" and "SOSTExon2down" was used. PCR products were mixed with loading buffer and applied to gel-electrophoresis.

2.3.6. Agarose gel electrophoresis

To separate nucleic acids depending on their size agarose gels were used. Gels were made by dissolving 1% agarose (1st Base) in 0.1M sodium borate (SB) buffer (pH 8.8) with CybrGreen (diluted 1:10,000; Invitrogen) and short boiling in a microwave oven. The solution was poured into a gel casting mold and allowed to harden at room temperature. 1/10 Volume 10× loading-

buffer (Fermentas) was added to the samples which were pipetted into the molds of the gel. The gel was run with a current of 150-300 Volts in a horizontal flat bed gel chamber (BioRad) filled with 1x SB-buffer. Gels were analyzed on a G:BOX gel documentation system (Syngene) with GeneSnap software (Syngene).

2.3.7. Extraction of DNA fragments from agarose gels

After gel electrophoresis, the fragment of interest was cut from the gel using a scalpel and transferred into a 1.5 ml reaction tube. The actual extraction was done using the Gel/PCR DNA Fragments Extraction Kit (GeneAid) according to the manufacturer's protocols.

2.3.8. Restriction enzyme digestion of DNA

Restriction enzyme digestion was used to cut DNA double-strands at defined consensus sequences. Depending on the experiment 1-5µg of DNA were digested in reaction volumes of 20-100µl. Furthermore the reaction consisted of 1/10 Volume reaction buffer and 10-20U of the desired restriction enzyme (Fermentas) and was incubated for at least 2 hours or over night at 37°C. Subsequent recovery of DNA was done by gel extraction (2.3.7) or a phenol:chloroform extraction (2.3.2).

2.3.9. Cloning work

2.3.9.1. General procedures

20-40 ng of the vector DNA was used for ligation and the amount of the insert DNA was adjusted to a molar ratio of 4:1 to the vector. Additionally the ligation reaction contained 2ul 5X DNA Ligase Reaction Buffer, 0.5µl T4 DNA Ligase (1U/µl; New England Biolabs), 1µl ATP (Fermentas) and H_2O to a final volume of 10µl. The reaction was incubated for 1hour at RT and was used afterwards to transform bacteria cells.

2.3.9.2 Cloning of *osx:CFP-NTR* plasmid

The *osx:CFP-NTR* vector was created in two steps. First, *mCherry* was released from the I-SceI-pBSII-SK plasmid containing the 4.1 kb *osx* promoter (Renn and Winkler, 2009) by digestion with *BamHI* and *NotI* and replaced with a short linker insert that contained the two additional restriction sites *SmaI* and *SalI* (after annealing the two oligonucleotides "LinkerBamSmaSalNotA" and "LinkerBamSmaSalNotB"). Then, a fusion construct of the *nfsB* gene and the gene encoding Cyan Fluorescent Protein (CFP) was isolated from the *ins:CFP-NTR* plasmid (kindly provided by D. Stanier; see Curado et al., 2008) by digestion with *SmaI* and *SalI* and ligated into the digested target vector.

2.3.9.3 TOPO/pDrive cloning of riboprobe templates

Purified PCR products of partial *lrp5* and *crestin* transcripts were ligated into the pDrive cloning vector (Qiagen) by adding 100 ng of DNA to 5µl of Ligation Master Mix and 1µl of vector (50 ng) and adjusting the total volume by addition of H_20 to 10µl. After incubation for 30 minutes at 4°C the reaction was ready for transformation.

The *sost* PCR product was cloned into pCRII-TOPO (Invitrogen) by adding 4µl of PCR product (~100 ng) to 1µl of salt solution and 1µl vector (50 ng). After incubation for 5 minutes at room temperature the reaction was ready for transformation.

2.3.10. Transformation of bacteria

The ligation mix was transformed into chemically competent *DH5α* (Invitrogen) by heatshock. For this, aliquots of bacteria (100µl) were thawed on ice and after addition of various amounts of ligation reaction (2.3.9.) incubated on ice for 30 minutes. For the actual heatshock, bacteria were exposed to 42°C in a thermomixer (Eppendorf) for 30 seconds and put back on ice for another 2 minutes. After addition of 900µl LB-medium bacteria were shaken at 37°C at 225 revolutions per minute (rpm) for 1h. Transformed bacteria were then plated on LB-agarose plates carrying the appropriate antibiotic resistance (Ampicilin or Kanamycin at 100 µg/ml) as well as 40µl IPTG

(100 mM) and 80µl X-Gal (20 mg/ml) for blue white selection. The LB-agarose plates were incubated over night at 37°C.

2.3.11 Preparation of plasmid DNA

Using sterile pipette tips single clones were picked from the bacteria plates and transformed to vials containing 5 ml LB-medium with the required antibiotic in a concentration of 50 µg/ml. The culture was incubated overnight at 37°C in a thermoshaker (NFORS). The next day, plasmid preparation was performed using the High-Speed Plasmid Mini Kit (GeneAid) according to the provided manual.

2.3.12 Sequencing of DNA

DNA sequencing was carried out at the department's DNA sequencing laboratory (DSL) with an ABI3130xl sequencer (Applied Biosystems) according to the dideoxy chain termination method (Sanger et al., 1977). Reactions were prepared using the BigDye® Terminator v3.1 Cycle Sequencing Kit (Applied Biosystems) according to the provided manual. Each reaction contained 1-50ng DNA, 1µl Primer (3µM) and 2µl BigDye reaction premix, diluted with H_2O to a total volume of 10µl.

Reaction profile: Initial denaturation of DNA took place at 96°C for 1 minute at the beginning of a cycle. There were 10 seconds of denaturation at 96°C followed by annealing of the sequencing primer for 10 seconds at around 55°C (the exact annealing temperature depends on the sequence of the primer used). Extension took place at 60°C for 4 minutes. This cycle was repeated 25 times. Subsequently, the reaction mix was diluted with H_2O to 20µl and transferred to a 1.5ml reaction tube. For precipitation of DNA, 2µl EDTA (125 mM), 2µl NaOAc (3 M) and 50µl ethanol (100%) were added. After 15 minutes of incubation at room temperature, the tubes were centrifuged at 13,000xg for 30 minutes at 4°C. Then the supernatant was removed to allow the pellet to dry, which was then sent to DSL for the actual sequencing process. The obtained sequence files were analyzed using BioEdit 7.0.5.2.

2.3.13 *In vitro* transcription to produce *in situ* probes

For digoxigenin (DIG) or fluorescein (FLU)-labeled riboprobes, plasmids were linearized with restriction enzymes. Subsequently, *in vitro* transcription was performed with RNA polymerase (Fermentas) and DIG/FLU-RNA labeling Mix (Roche).

The transcription reaction contained 1µg of linearized plasmid DNA, 2µl 10× Labeling Mix, 2µl RNA Polymerase (20 U/µl), 4µl 5x Transcription-buffer and 1µl Ribolock RNase Inhibitor (40 U /µl, *Roche,* Mannheim). The total volume was adjusted to 20µl with H_2O. The reaction was incubated at 37°C for 2 hour and subsequently incubated another 15 min at 37°C with 1µl RNase free DNaseI (10 U/µl; Fermentas) to remove the template DNA. Purification of the transcripts was done by ethanol precipitation with 1/10 Volume $LiCl_2$. The RNA pellet was dissolved in a mixture of 25µl H_20. One μl was used for quality analysis by gel electrophoresis while the other 24µl were dissolved in 76µl hybridization mix and stored at -30°C.

Riboprobes were generated with the following combination of linearizing restriction enzyme and Polymerase: *osc*: BamHI/T7 RNA-Polymerase (FLU labeled; all others DIG labeled); *lrp5*: XhoI/T7 RNA-Polymerase; *sost*: NotI/T7 RNA-Polymerase; *gfp*: HindIII/T7 RNA-Polymerase; *lef1*: NotI/SP6 RNA-Polymerase; *ccnd1*: BamHI/T7 RNA-Polymerase; *dlx2a*: BamHI/T7 RNA-Polymerase; *foxd3*: BamHI/T7 RNA-Polymerase. Additional plasmids were kindly provided by Dr. Joerg Renn (NUS), Dr. Thuy Thanh To (NUS), Dr. Jan Brocher (NUS) and Dr. Cheah Siew Hong (NUH).

2.4. Generation of *osx:CFP-NTR* medaka

To generate transgenic medaka, the circular plasmid was injected into one-cell stage embryos using the ISce-I meganuclease technique (Rembold et al., 2006). Injected fish were selected for osteoblast specific CFP signal, raised and crossed to wild-type fish to identify germline transmitting founders. Intercrossing F1 transgenic fish yielded homozygous F2 embryos according to Mendelian ratios of inheritance.

2.5. Staining assays

2.5.1. Whole-mount *in situ* hybridization

To analyze patterns of gene expression I stained transcripts by means of *in situ* hybridization. Fixed embryos were rehydrated in descending dilutions of methanol in H_2O (75% - 50% - 25%) each step lasting 5 minutes. After a wash in PBST embryos were subjected to Proteinase K treatment to further perforate the cell membranes to ensure best conditions for riboprobe penetration. For this, embryos were incubated in 10 µg/ml Proteinase K (Roche; diluted in PBST). The duration of this step was depending on the developmental stage of the embryos and done according to Thisse and Thisse (2008). The reaction was stopped by two washes in 1x glycine (200 µl 50x glycine/10 ml PBST) and refixation in 4% PFA for 20 minutes. After that, embryos were washed five times for 5 minutes in PBST to remove traces of PFA.

For prehybridization embryos were incubated in hybridization mix (50% formamide, 5x SSC, 150 µg/ml Heparin, 5 mg/ml torula RNA, 0.1% Tween) for 1 hour at 65°C in a waterbath. For the actual hybridization step, embryos were incubated in riboprobes diluted 1:100 in hybridization mix at 65°C in a waterbath over night. The next day, riboprobe solutions were removed and stored for future experiments. Embryos were washed twice for 30 minutes at 65°C in 50% formamide/2x SSCT followed by one wash for 30 minutes at 65°C in 2x SSCT and another two washes for 30 minutes at 65°C in 0.2x SSCT. Then, one wash in PBST for 5 minutes took place at room temperature.

For antibody binding, embryos were blocked for 1 hour in 5% sheep serum/PBST at room temperature before they were incubated for 2 hours in preabsorbed sheep anti-DIG/anti-FLU Fab-fragments coupled with alkaline phosphatase (Roche) diluted 1:2000. After that, embryos were washed at least five times in PBST whereby one wash step was carried out over night to ensure removal of all unbound antibodies.

At the third day, staining was performed by incubating embryos two times for 5 minutes in

prestaining buffer (0.1 M NaCl, 0.05 M $MgCl_2$, 0.1 M Tris-HCl pH9.5, 0.1% Tween) to adjust the conditions for enzymatic reaction of alkaline phosphatase. As substrate BM-Purple (Roche) was used and incubation lasted for several hours in the dark until color reaction was detectable. To stop the reaction embryos were washed several times in PBST and stored in 4%PFA. The procedure was carried out in 24-well plate format according to Thisse and Thisse (2008).

2.5.2. Immunohistochemistry

Immunohistochemistry was carried out by rehydrating fixed embryos in descending dilutions of methanol in H_2O (75% - 50% - 25%). Subsequently, embryos were kept in PBDT (1% DMSO, 1% BSA, 2.5% sheep serum and 0.1% TritonX in PBST) for 1 hour and incubated in primary antibody solution (diluted in PBDT) over night. On the second day, embryos were washed four times for 1 hour in PBST/0.1% TritonX and incubated with the secondary antibody (diluted in PBDT) over night. On the third day, embryos were washed four times for 1 hour in PBST/0.1% TritonX. After binding with fluorescent dye labeled antibodies, embryos were ready for imaging. When stained with biotinylated antibodies, embryos were subjected to further processing following the Vectastain (Vector Laboratories Inc., Burlingame CA) protocol: A mix of 1 drop of solution A and 1 drop of solution B was incubated in PBS for 30 minutes before it was used to incubate embryos for 1 hour at room temperature to bind a peroxidase to the antibody . Subsequently, embryos were washed four times for 30 minutes in PBST/0.1% TritonX. Then embryos were stained with 3,3'-Diaminobenzidine (DAB). A Sigma Fast^{TM} DAB Tablet (Sigma) was dissolved in 5ml H_20 and embryos were pre-incubated with that solution for 30 minutes. Then, a Sigma Fast^{TM} DAB Tablet was diluted in 5ml H_20 together with a Urea/H_2O_2 tablet. Incubation of embryos in this solution yielded a color reaction after few minutes.

To stain for GFP positive cells a monoclonal mouse anti-GFP antibody (diluted 1:1000; Invitrogen) was used in combination with anti-mouse Alexa488 coupled antibody (diluted 1:1000; Invitrogen) or biotinylated anti-mouse antibody from the Vectastain ABC Kit (diluted 1:1000;

Vector Laboratories Inc., Burlingame CA) in combination with Sigma Fast™ 3,3'-Diaminobenzidine (DAB) Tablets (Sigma). To stain for mitotic cells, rabbit derived monoclonal anti-phosho-histone3 (pH3) antibody (diluted 1:1000; Upstate Biotechnology, NY) was used in combination with an anti-rabbit Alexa568 coupled antibody (diluted 1:1000; Invitrogen).

2.5.3. Cell proliferation assay by analysis of BrdU incorporation

To check for nuclei in S-phase, embryos were incubated in 10 mM BrdU for 30 minutes, washed several times and kept another 30 minutes before fixation in 4%PFA over night. On the following day, embryos washed several times in PBST and kept overnight in methanol absolute. For staining, embryos were rehydrated in descending dilutions of methanol in H_2O (75% - 50% - 25%), followed by incubation for 1 hour in 2N HCl at 37°C to expose the DNA. Subsequently, BrdU-positive nuclei were stained by immunohistochemistry (see 2.5.2.) using mouse anti-BrdU antibody (BSHB, Iowa City, IA; diluted 1:500 in PBDT) in combination with anti-mouse Alexa 488 coupled secondary antibody (diluted 1:1000; Invitrogen).

2.5.4. Histological staining

This part was carried out by Dr. Ann Huysseune (Ghent University, Belgium). Embryos or larvae were rinsed in 0.1 M cacodylate buffer with 10% sucrose added, then postfixed for 2 hours in 1% OsO4 in 0.1 M cacodylate buffer to which 8% sucrose is added, rinsed again in 0.1 M cacodylate buffer, dehydrated through a graded series of ethanol, brought into propylene oxide and finally embedded in hard epon (epon A:B mixed 2:3, according to Luft, 1961). Serial transverse sections of 1 µm were prepared using a diamond knive mounted on a Prosan HM 360 microtome, stained with toluidine blue and mounted with DPX mountant (Sigma). They were viewed under transmitted light on a Zeiss AxioImager Z1. Photographs were taken with a Zeiss Axiocam MRc videocamera using Axiovision release 4.8 software.

2.5.5 Cartilage and bone staining

2.5.5.1. Dual-color acid-free cartilage and bone staining

Dual-color acid-free cartilage and bone staining was carried out on 7 days post fertilization (dpf) larvae according to Walker and Kimmel (2007): Larvae were fixed in 4% PFA for 2h, washed in PBST and incubated in 50% ethanol for 10 minutes. Subsequently, larvae were incubated over night in staining solution consisting of 700µl ethanol, 200µl $MgCl_2$ (0.5 M), 50µl Alcian Blue (0.4%), 40µl H_20 and 10µl Alizarin Red (0.5%). On the next day, larvae were washed in H_20 and bleached in 1% KOH/1.5% H_2O_2 for 20 minutes to remove pigmentation. A clearing step in 20% glycerol/0.4% KOH for 30 minutes made the tissue more transparent. For imaging, the viscerocranium was separated from the neurocranium by manual dissection with injection needles and mounted in glycerol on a microscopic slide with cover slip.

2.5.5.2. Live skeletal staining

For life skeletal staining, 0.01% Alizarin Complexone (ALC, Sigma) was dissolved in 1x Danieau's solution and filtered through a 0.22µm pore size filter. Larvae were incubated in staining solution for 2 hours at 30°C in the dark. Subsequently they were rinsed several times in 1x Danieau's solution and mounted for microscopic imaging.

2.5.6. Staining for apoptosis

2.5.6.1. Acridine Orange staining

To identify cell death in living organism, larvae were incubated for 20 min in 5 µg/ml Acridine Orange (Sigma) dissolved in 1x Danieau's solution in the dark. Afterwards, larvae were washed 3 times in 1x Danieau's solution and mounted for imaging.

2.5.6.2. TUNEL assay

For TdT-mediated dUTP-biotin nick end labeling (TUNEL) assay, embryos were fixed in 4% formaldehyde over night. After several washes in PBST they were kept in methanol absolute. The

assay was carried out using the ApopTag® Peroxidase In Situ Apoptosis Detection Kit (Millipore, Temecula, CA) following the provided protocol: Fixed embryos were rehydrated in descending dilutions of methanol in H_2O (75% - 50% - 25%) and washed three times in PBST for 5 minutes each. To quench endogenous peroxidase activity, embryos were incubated in 3% H_2O_2 for 10 minutes followed by two washes in PBST for 1 minute each. Next, incubation in 100µl equilibration buffer for 20 minutes set the conditions for incubation in 50µl reaction solution for 1 hour at 37°C. The process was stopped by replacing with 220µl stop/wash solution for 10 minutes back at room temperature. After three washes in PBST for 1 minute each, embryos were incubated over night in anti-DIG peroxidase conjugate at 4°C. On the next day, embryos were washed three times in PBST for 5 minutes each and subjected to DAB staining (see 2.5.2).

2.6. Preparation of specimen and image acquisition

2.6.1. Preparation of whole mount embryos *in vivo*

For *in vivo* imaging using the stereomicroscope, embryos/larvae were anesthetized in 0.05% Tricaine (Sigma) and immobilized in 3% methylcellulose in 35 mm glass base dishes (Iwaki). The position relative to the objective was adjusted with a fine injection needle. For confocal imaging embryos/larvae were mounted in 1.5% low melting agarose (BioRad) in the same dishes.

2.6.2. Preparation of stained whole mount embryos

For imaging stained whole mount embryos, they were transferred into glycerol through an ascending gradient (33%, 66%, 100%). For imaging, embryos/larvae were mounted in 35mm glass base dishes (see 2.6.1).

2.6.3. Preparation of stained flat mount embryos

For higher resolution flat mount imaging, stained embryos were transferred into glycerol as described in 2.6.2. Yolk platelets were removed with fine injection needles and embryos were

transferred into a fresh drop of glycerol. The embryos were orientated with the needle and covered with a glass cover slip using separate cover slips as spacers.

2.6.4. Manual sections

This part was carried out by Flora Rajaei (Winkler lab; NUS). Stained embryos were transferred into glycerol as described in 2.5.2. With a scalpel, embryos were sliced manually in sections which were mounted in a fresh drop of glycerol on a microscopic slide and covered with a cover slip.

2.6.5. Cryosections

Stained embryos/larvae were embedded in 1.5% agarose/5% sucrose. Blocks containing the specimen were cut out and soaked overnight at 4°C in 30% sucrose. For cryosectioning on a CM1850 cryotome (Leica) blocks were mounted on sectioning stage with tissue freezing medium (Jung, Germany) and plunge frozen in liquid nitrogen. Section diameter was 20-30 µm.

2.6.6. Plastic sections

This part was carried out by Dr. Ann Huysseune (Ghent University, Belgium). Plastic sections of whole mount hybridized specimens were prepared according to Verstraeten et al. (in press). Briefly, whole mount embryos were slowly dehydrated through a graded series of ethanol and embedded in soft epon (epon A:B mixed 3:2, according to Luft, 1961). Serial transverse sections of 4 µm were prepared using a diamond knife mounted on a Prosan HM 360 microtome, mounted with DPX mountant (Sigma) and viewed under Nomarski optics on a Zeiss AxioImager Z1. Photographs were taken with a Zeiss Axiocam MRc videocamera using Axiovision release 4.8 software.

2.6.7. Image acquisition

Image acquisition on *in vivo* transgenic reporter expression was done with a Nikon SMZ1000 stereomicroscope and a Nikon T1-SM inverted microscope with GFP filter set. Bone mineralization stained with ALC and osteoblasts expressing CFP were monitored with the same stereomicroscope with FITC and CFP filter sets. Flat mounted embryos were imaged on a Nikon Eclipse 90i upright microscope and NIS-element BR software (Nikon). More detailed images were taken on an LSM 510 Meta laser scanning confocal microscope (Zeiss). Alexa488 was detected by excitation with an argon multi-line gas laser at 488nm and detection through the BP 505-530nm filter. Alexa568 was detected by excitation with a Helium Neon gas laser at 543nm and detection through the LP 560nm filter. CFP was detected by excitation with an argon multi-line gas laser at 458nm and detection through the LP 475nm filter. ALC was detected by excitation with a Helium Neon gas laser at 543nm and detection through the LP 560nm filter. LSM software (Zeiss) was employed for image processing.

2.6.7. Cell count and statistical analysis

To eable quantitative statements about cell proliferation assays, cells were counted in the acquired images of multiple individuals (n). Therefore, a region of interest (ROI) was defined by framing the area on the images to cover the hindbrain region between rhombomeres 4 to 8. Within this area all positively stained nuclei were counted manually. By means of Microsoft Excel 2011 the calculations for average, standard deviation and *P*-value (Student's T-test) were carried out.

3. RESULTS

3.1. Conditional ablation of osteoblasts in medaka

3.1.1. *osx-positive* osteoblasts of *osx:CFP-NTR* transgenic medaka are sensitive towards Mtz treatment

In the stable transgenic *osx:CFP-NTR* medaka line, a fusion protein of Nitroreductase (Ntr) and Cyan Fluorescent Protein (CFP) is expressed under control of the 4.2kb *osx*-promoter, which has been used previously to visualize early osteoblasts in medaka (Renn and Winkler, 2009; Fig. 3.B). The distinct pattern of CFP fluorescence is identical to the reporter expression of *osx:mCherry* medaka both during early and later stages (Renn and Winkler, 2009). At 20 dpf, CFP can be detected in all skeletal elements, such as cleithrum, operculum and pharyngeal teeth in the head, the fin rays of the caudal fin and in neural and hemal arches as well as the edges of the centra in the axial skeleton (Fig. 3.C-E).

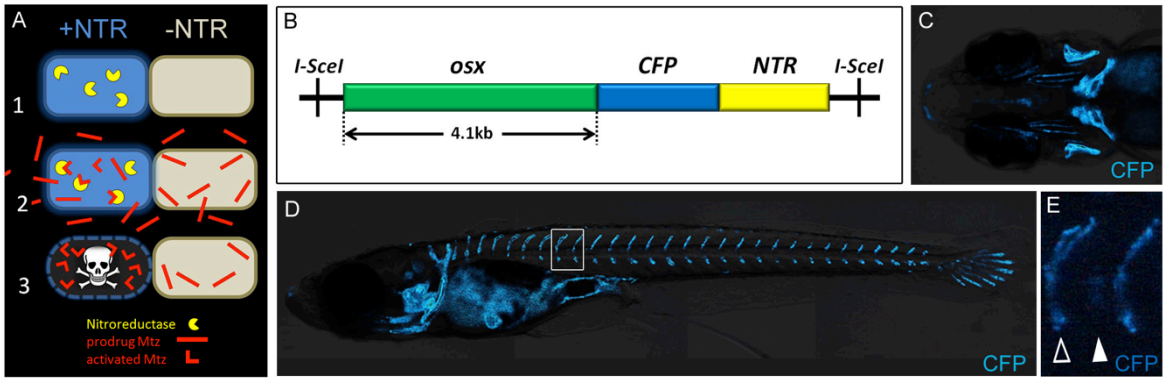

Fig. 3. An *osx:CFP-NTR* transgenic medaka line for osteoblast ablation. (**A**) Mechanism of nitroreductase (NTR) facilitated conditional cell ablation. (**1**) CFP and NTR (yellow cell) are expressed under control of the *osterix* promoter (blue cell). (**2**) Larvae are immersed in the prodrug Mtz (straight red bars). Only those cells that express NTR transform it into the activated Mtz (kinked red bars). (**3**) Activated Mtz is a DNA crosslinking agent that induces apoptosis. (**B**) Schematic diagram of construct used to generate the transgenic *osx:CFP-NTR* line. (**C,D**) *osx:CFP-NTR* larva at 20 dpf showing stable expression of CFP in osteoblasts (C, ventral view of head region; D, lateral view of entire larva). Brightfield image is combined with fluorescent image. Note: Blue signal in the yolk region is due to autofluorescence. (**E**) Higher magnification view of ventral body as boxed in D. Empty arrowhead demarcates anterior edge of centrum, white arrowhead marks posterior edge.

To test whether the reporter expressing *osx*-positive cells are sensitive towards Mtz prodrug treatment, *osx:CFP-NTR* larvae were exposed to 10mM Mtz/0.1% DMSO while the respective control group was incubated in 0.1% DMSO (Fig. 4B). As additional control, the same treatment was conducted on *osx:mCherry* larvae to show that the specificity of cell ablation is linked to NTR/Mtz interaction (Fig. 4A). At 6 dpf, larvae from both transgenic lines were dechorionated, incubated in Mtz and analyzed for fluorescence. At this stage *osx:mCherry* (Fig. 4C,D) and *osx:CFP-NTR* larvae (Fig. 4E,F) showed the typical pattern of fluorescence labeling in skeletal elements as described earlier (Renn and Winkler, 2009). After keeping the larvae in Mtz for 6 days (6-12 dpf) fluorescence was analyzed again. In *osx:mCherry* larvae no difference between Mtz and DMSO treated individuals could be observed (Fig. 4G and H). In contrast, a substantial reduction of fluorescence signal was evident in the skeletal elements of Mtz exposed *osx:CFP-NTR* larvae (Fig. 4J), whereas the DMSO treated larvae showed normal stage-specific CFP pattern (Fig. 4I). This effect was found to be most prominent in the cleithrum and operculum (arrow and arrowhead in Fig. 4J), as well as in the neural arches, whereas some fluorescence signal remained in the ventral craniofacial skeleton e.g. in the branchiostegal rays. Nine repetitions were carried out with the *osx:CFP-NTR* line using a total of 73 DMSO controls while 127 larvae were exposed to Mtz. From the 60 (= 82%) surviving control larvae none showed reduced CFP signal while from the group of 80 (= 63%) surviving Mtz treated larvae all were characterized by substantial loss of fluorescence. In the four repetitions of the *osx:mCherry* control experiment, a total of 31 larvae served as DMSO controls and 48 were exposed to Mtz. After 6 days of treatment (dot), 30 (=97%) of the DMSO controls survived, as did 29 (=60%) of the Mtz treated larvae. Neither in the DMSO group nor in the Mtz group any individual was found with reduced fluorescent reporter signal. Taken together, these data suggest that successful ablation of *osx*-positive cells occurred only after Mtz treatment of NTR transgenic specimen. The regular *osx*-positive cell status in DMSO controls and in Mtz treated *osx:mCherry* larvae supports Mtz target specificity and excludes off target effects of the prodrug.

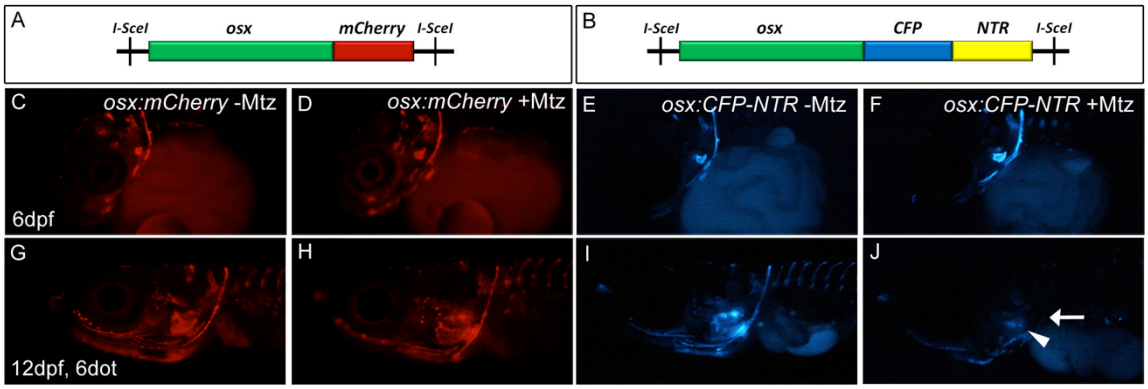

Fig. 4. Osteoblasts of transgenic *osx:CFP-NTR* medaka are sensitive towards treatment with Metronidazole (Mtz). (**A**,**B)** Schematic diagrams of constructs used in transgenic lines. (**C-F**) Larvae before onset of Mtz treatment at 6 dpf (0 dot). Note that all larvae show reporter fluorescence indicating the presence of *osx*-positive osteoblasts. (**G-J)** Larvae at 12 dpf after 6 days of treatment (6 dot). Note that only *osx:CFP-NTR* larvae show reduction in fluorescent signal in skeletal structures, such as cleithrum (arrow) and operculum (arrowhead) indicating cell ablation. Data were obtained from 9 (*osx:CFP-NTR*) and 4 (*osx:mCherry*) independent experiments, representative examples are shown.

3.1.2. *osx*-positive cells undergo apoptosis upon Mtz treatment

Upon reduction by Ntr Mtz becomes a DNA-crosslinking agent and moderates cell ablation by apoptosis (Pisharath et al., 2007; Curado et al., 2008). To confirm that loss of the fluorescent signal is due to cell ablation, two assays for apoptotic cell death were carried out. Acridine Orange (AO) stains nuclei of apoptotic cells *in vivo* in medaka (Yasuda et al., 2008). *osx:CFP-NTR* larvae which underwent Mtz treatment and their respective DMSO controls were stained with AO to assess occurrence and frequency of cell death. The DMSO control showed a normal CFP pattern (Fig. 5A,B) and no AO signal (Fig. 5E,F; n=12 embryos), which is also evident in the CFP/AO merged image (Fig. 5I,J). In contrast, 15 out of 17 Mtz treated larvae, which were characterized by substantial loss of CFP signal at the position of cleithrum, operculum and pharyngeal teeth (Fig. 5C,D), exhibited strong AO signal in the regions of CFP loss (see arrows in Fig. 5G,H). The experiment was repeated using TdT-mediated dUTP-biotin nick end labeling (TUNEL). While no signal could be detected in the DMSO control larvae (Fig. 5M,M',N,N'), TUNEL staining was observed in 11 out of 14 Mtz treated larvae at the positions of operculum

and pharyngeal teeth (arrows in Fig. 5O,P, magnifies views in O',P') consistent with the AO results. Notably, these regions contain *osx* expressing osteoblasts (Fig. 3.D; and Renn and Winkler, 2009). Taken together, these findings support that loss of CFP fluorescence is a consequence of apoptosis due to cytotoxic properties of Ntr catalyzed reduction of Mtz in Ntr-positive cells.

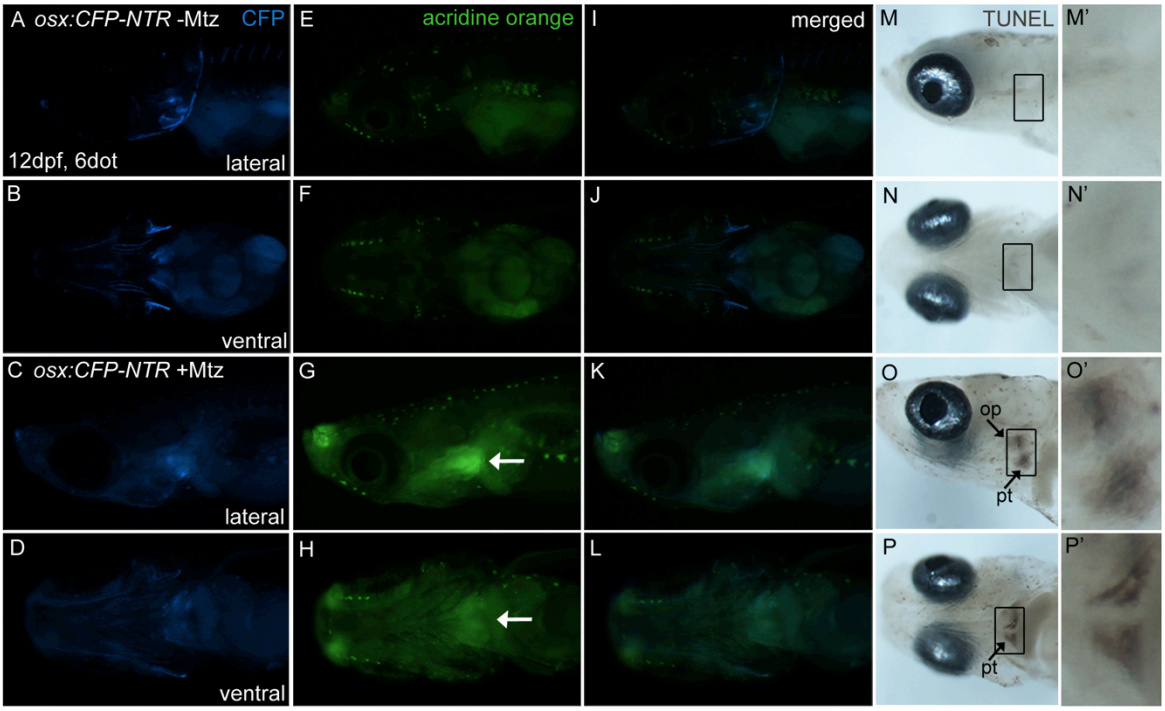

Fig. 5. NTR/Mtz treatment leads to cell apoptosis as evident by Acridine Orange (A-L) and TUNEL assays (M-P) at 12 dpf (6 dot). **(A,B)** *osx:CFP-NTR* DMSO controls with normal pattern of CFP expression in skeletal elements. (**C,D)** Mtz treated *osx:CFP-NTR* larva with loss of *osx*-positive cells in skeletal elements evident by loss of fluorescent signal. (**E,F)** Control larva shows no Acridine Orange (AO) signal. (**G,H)** Mtz treated larva with strong AO staining in regions of skeletal elements. (**I,J)** Merged images of A and E, as well as B and F, respectively. (**K,L)** Merged images of C and G, as well as D and H, respectively. (**M,N)** TUNEL staining reveals no increased apoptosis in DMSO treated control larvae (**M**', **N'** are higher magnification views of regions boxed in M and N). (**O,P)** Mtz treated larvae exhibit TUNEL positive cells in the operculum (op, arrow in O, not visible in P) and pharyngeal teeth (pt, arrow in O,P). (**O',P')** are higher magnification views of regions boxed in O and P. Data were obtained from two (AO) and 1 (TUNEL) independent experiments, representative examples are shown.

3.1.3. Osteoblast loss is confirmed by *osteocalcin* expression analysis

Osteocalcin (*osc*) is expressed in mature osteoblasts (Renn and Winkler, 2010). To verify that Mtz treatment leads to the loss of differentiated osteoblasts, I performed *in situ* hybridization with an *osc* riboprobe on Mtz treated *osx:CFP-NTR* larvae and their respective DMSO controls. At 12 dpf (6 dot), the expression of *osc* appeared normal in DMSO control larvae (Fig. 6A,A') while it was remarkably reduced in Mtz treated individuals (Fig. 6B,B'). This was even more evident at 18 dpf (12 dot), when DMSO controls showed prominent expression in the gill regions (Fig. 6C,C'), while *osc* expression was substantially reduced in 5 out of 6 Mtz treated larvae (Fig. 6D,D'). This further supports the loss of matured osteoblasts in Mtz treated *osx:CFP-NTR* larvae.

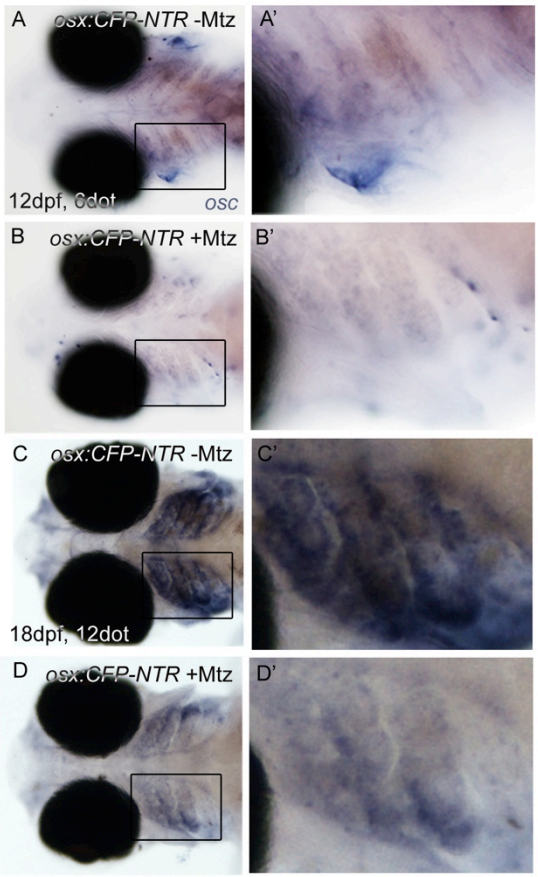

Fig. 6. Confirmation of osteoblast loss by *osc* expression analysis. Ventral view of DMSO controls (**A/A'**, **C/C'**) and Mtz treated larva (**B/B', D/D'**) at 12 dpf (6 dot) and 18 dpf (12 dot), respectively. Note that Mtz treated larvae show less *osteocalcin* (*osc*) expression when compared to controls. A'-D' represent higher magnification views of areas boxed in A-D. Data were obtained from two (12 dpf) and one (18 dpf) independent experiments, representative examples are shown.

3.1.4. Ablation of *osx*-positive osteoblasts results in cranial bone loss and fusion of vertebral centra

To analyze the impact of *osx*-positive cell ablation on the skeleton, Alizarin Complexone (ALC) bone staining was performed *in vivo* on *osx:CFP-NTR* larvae after 12 days of Mtz treatment. In control larvae, the CFP signal overlaps with ALC in the head skeleton (Fig. 7A-G) and in the caudal fin (Fig. 7W). In the vertebral column, the neural arches show overlap of CFP and ALC signal (Fig. 7O-Q). CFP is also visible at the edges of the centra (arrow in Fig. 7O). This pattern is consistent with the spatiotemporal distribution of *osx:mCherry* positive cells reported by Renn and Winkler (2009).

In the head skeleton, I focused my attention on analyzing two structures: the cleithrum and the operculum. These are among the first structures in the cranial skeleton to undergo mineralization and *osx* expression (Renn and Winkler, 2009). In control larvae at 18 dpf, osx-positive cells formed a layer around the mineralized cleithrum (Fig. 7A-D) and operculum (Fig. 7E-G), respectively, as evident by the overlap of CFP and ALC signals (Fig. 7D,G). However, in Mtz treated larvae, the CFP signal was substantially reduced. No *osx*-positive cells could be detected around the cleithrum (Fig. 7H-K) and only few cells remained to cover the operculum (Fig. 7L-N). Furthermore, the cleithrum and operculum showed weaker mineralization compared to controls (Fig. 7C,J and Fig. 7F,M) and the operculum exhibited large furrow shaped structures devoid of any obvious mineralization (Fig. 7M).

In the axial skeleton of controls, *osx*-positive cells are positioned around the neural arches and at the borders of each chordal centrum next to the base of the arches (Fig. 7O-Q). The intervertebral region is located between the centra (arrowheads in Fig. 7P). In Mtz treated larvae, CFP expression was absent (Fig. 7R-T). Mineralization of the neural arches was reduced (compare Fig. 7P,S), and the arches appeared disorganized when compared to controls (arrow in Fig. 7S). Also, no CFP expression could be detected around the centra which indicates that all *osx*-positive cells

also in this region were ablated (Fig. 7R). Interestingly, the size of the intervertebral regions (compare arrowheads in Fig. 7P and S) was strongly reduced and the chordal centra appeared partially fused. Such fusions occurred at various positions along the vertebral column (see Fig. 7W for different larva). ALC staining displayed an over-mineralization in the centra of Mtz treated larvae concomitant with a substantial loss of CFP signal (Fig. 7W,X) compared to their DMSO controls (Fig. 7U,V). Mineralization was extended across the rostrocaudal borders of several centra resulting in a fusion of vertebral bodies. This phenotype was observed in 34% (11 of 32) of analyzed larvae which showed centra fusions at various regions along the vertebral column after 12-16 dot (see Fig. 8 for additional examples). Such over-ossification phenotypes were only observed in Mtz treated *osx:CFP-NTR* larvae but neither in DMSO controls (n=58) nor in *osx:mCherry* transgenic larvae (n=29, DMSO treated; n=16, Mtz treated) or wild type larvae (n=23, DMSO treated; n=17, Mtz treated). This suggests that the phenotype is a direct consequence of NTR/Mtz mediated *osx*-positive cell ablation.

Taken together, these data suggest that depletion of *osx*-positive osteoblasts reduces ossification of early bone structures, such as the cleithrum, operculum and neural arches. Interestingly however, it also leads to over-mineralization in the vertebral column and fusion of centra in a proportion of NTR/Mtz treated embryos. This suggests that *osx*-positive cells possibly have a border defining function in the developing vertebral column, required for the metameric appearance of the vertebral bodies.

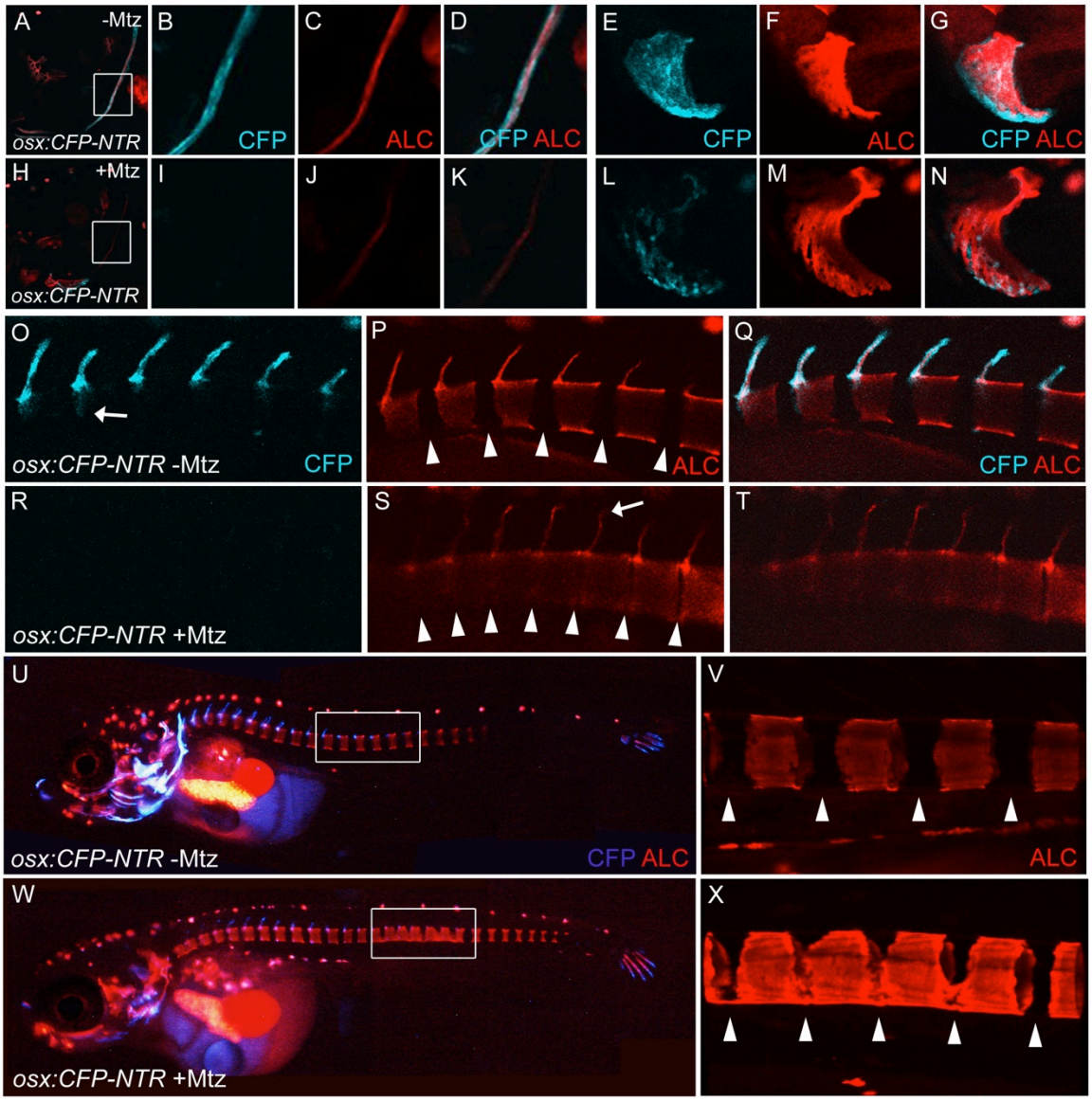

Fig. 7. Ablation of *osx*-positive osteoblasts leads to defective ossification in head and axial skeleton. (**A-N)** Lateral views of head region of DMSO control (A-G) and Mtz treated larva (H-N). B-D and I-K are higher magnification views of cleithrum boxed in A and H, respectively. Operculum of a DMSO control (E-G) and Mtz treated larva (L-N). Note: Loss of CFP and absence of mineralization in cleithrum and operculum of Mtz treated larvae when compared to controls. (**O-T)**. Views on anterior centra in DMSO controls (O-Q) and Mtz treated larvae (R-T). Arrow in O points at CFP positive cells in rostral area of centra. Arrowheads in P and S indicate intervertebral regions. Arrow in S points at disorganized neural arch. Note loss of CFP and fusion of anterior centra in Mtz treated larva. (Q,T) Merged images of O/P and R/S, respectively. (**U-X**) Lateral views on DMSO control (U,V) and Mtz treated larvae (W,X). Note fusion of centra in Mtz treated larva (arrowheads in X compared to V). U and W images were taken with a stereomicroscope, all others with a confocal microscope. V and X are projections of confocal z-stacks, all others are single stack images. All pictures were taken at 18 dpf (12 dot) with anterior to the left. Data were obtained from nine (*osx:CFP-NTR*), four (*osx:Mcherry*) and four (wild-type) independent experiments, representative examples are shown.

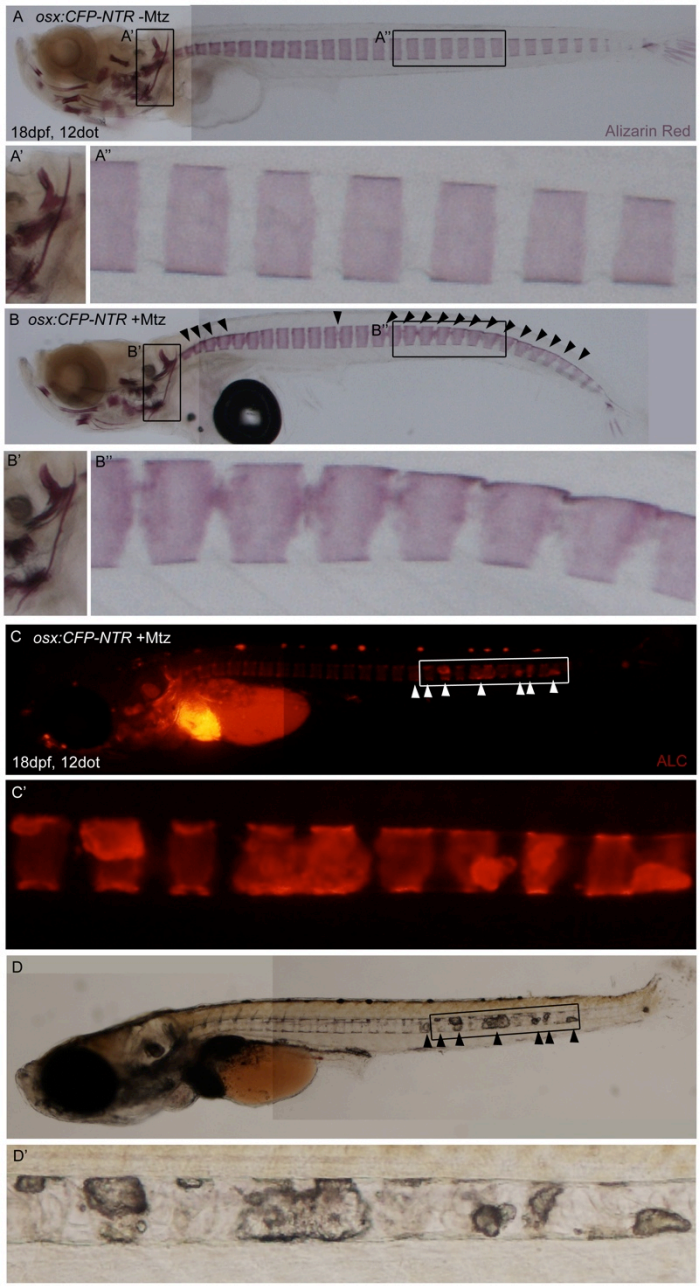

Fig. 8. Additional examples of Mtz treated *osx:CFP-NTR* larvae exhibiting fused centra at 18 dpf (12 dot). (**A,B)** DMSO treated control larva and Mtz treated larva, respectively, stained with Alizarin Red. The cleithrum of Mtz treated larva shows reduced mineralization (**A',B'**). The vertebral column shows fusion of centra at various positions (arrowheads in B). A'/A'' and B'/B'' are higher magnifications of regions boxed in A and B. (**C,C')** Additional example of Mtz treated larvae stained with ALC showing ectopic mineralization in several vertebral bodies (arrowheads). (**D,D')** Same larva as shown in C/C' exhibiting over-mineralization under brightfield illumination (arrowheads). A'-D' are magnifications of frames in A-D. All pictures were taken in lateral view with anterior to the left. Data were obtained from nine independent experiments, representative examples are shown.

3.1.5. *osx*-positive tissue regenerates after Mtz treatment

Next, I addressed whether ablated *osx*-positive cells can be replenished after Mtz treatment to regenerate bone tissue. *osx:CFP-NTR* larvae were subjected to Mtz treatment from 6 dpf to 15 dpf (9 days) to ablate *osx*-positive cells (Fig. 9A). Compared to DMSO controls (Fig. 9B/B'), Mtz treated larvae showed severe reduction of *osx*-positive cell numbers as evident by reduced CFP fluorescence (Fig. 9C/C'). Subsequently, the Mtz solution was removed, larvae were washed several times in Danieau's solution and allowed to recover for 10 more days until 25 dpf. For this, single larvae were kept separated to allow tracking of individual recovery situations. The status of osteoblast regeneration was assessed at day 20 (5 days post treatment; dpt) and day 25 (10 dpt). At 5 dpt, I observed an increase of CFP fluorescence in all 11 Mtz treated larvae (Fig. 9C/C',E/E'). Compared to controls at the identical stage, however, there was still less CFP signal in these larvae (Fig. 9D/D',E/E'). At 10 dpt, over 50% of the Mtz treated larvae showed almost identical CFP signal intensity when compared to controls at 5 dpt (Fig. 9D/D',G/G'). Notably, the size of the operculum after 10 days of regeneration was comparable to controls at 15 dpf (compare Fig. 9G' to B'). Taken together, these data suggest that medaka larvae are able to compensate for the loss of osteoblasts by regeneration in this cell lineage.

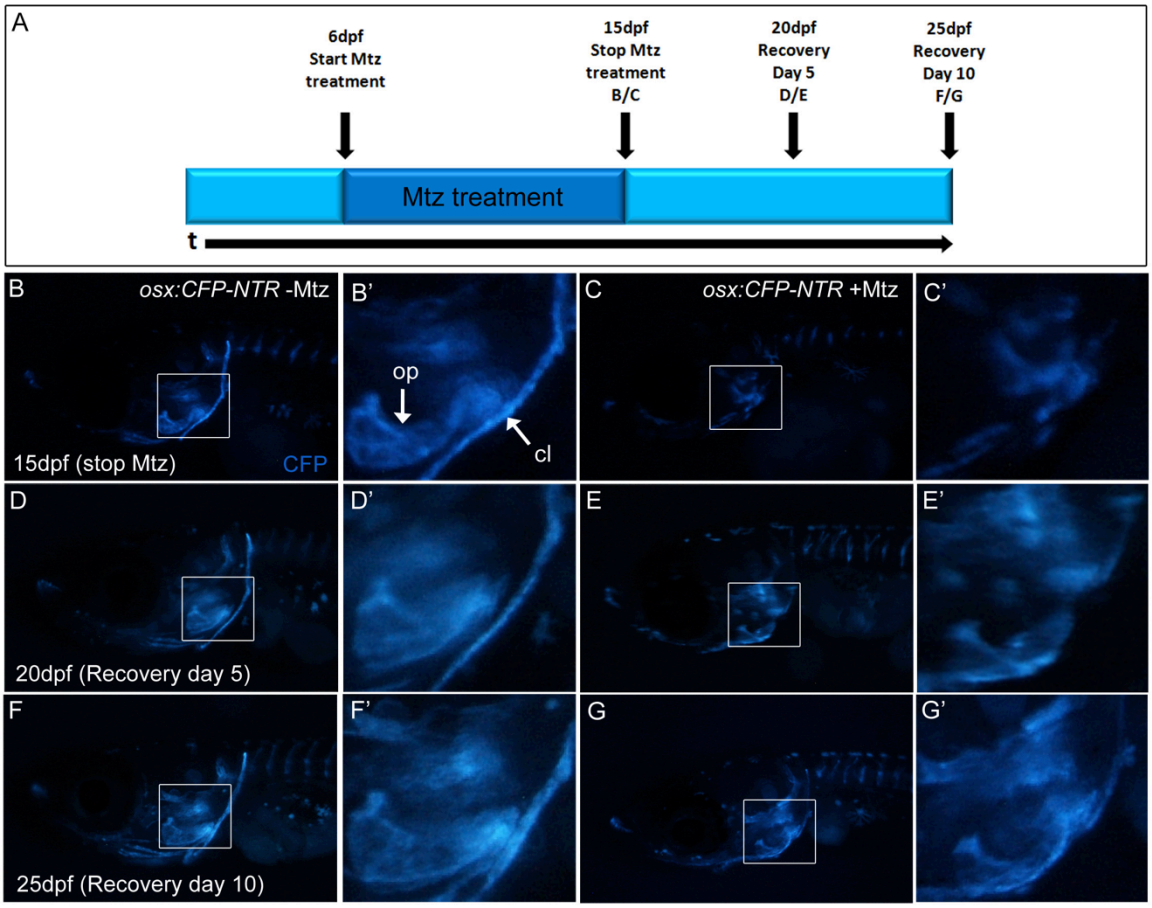

Fig. 9. Regeneration of ablated *osx:CFP-NTR* cells. (**A)** Schematic view of experimental timeline. *osx:CFP-NTR* larvae were incubated in Mtz for the indicated period (6 dpf-15 dpf). Subsequently, larvae were allowed to recover for 10days. Images were taken at time points indicated (15/20/25 dpf). DMSO controls (**B**) and Mtz treated larva after treatment (**C**). Arrows in B' indicate cleithrum (cl) and operculum (op). (**D-G**) CFP expression in controls (D, F) and Mtz treated larva (E, G) after 5 and 10 days recovery, respectively. Note increasing CFP in Mtz treated larvae during recovery. A'-G' show high magnification views of areas boxed in A-G, respectively. All pictures were taken in lateral view with anterior to the left. Data were obtained from three independent experiments, representative examples are shown.

3.2. Functional characterization of Lrp5 and its putative inhibitor Sost during craniofacial skeleton formation

3.2.1. Lrp5 and Sost are conserved at the sequence level

Sequence information for zebrafish *lrp5* and *sost* is available in the Ensembl database (www.ensembl.org). *lrp5* is located on chromosome 25 and annotated as ENSDARG00000006921. It spans a genomic region of over 140 kilobases (kb) (10,854,422-10,981,755), with an open reading frame (orf) of 4845 basepairs (bp) in 24 exons. The deduced amino acid (aa) sequence contains 1615 aa. Using ClustalW multiple alignment (www.ebi.ac.uk/Tools/msa/clustalw2; Chenna et al., 2003) the protein sequence was compared to orthologs in human (HsLrp5; ENSG00000162337), mouse (MmLrp5; ENSMUSG00000024913), Xenopus (XtLrp5; ENSXETG00000010024) and fruitfly (DmArrow; FBgn0000119). Pairwise alignments generated with bl2seq (http://blast.ncbi.nlm.nih.gov; Altschul et al., 1997) revealed sequence identities of 76% with HsLrp5, 75% with MmLrp5, 76% with XtLrp5 and 43% with DmArrow, respectively. A zebrafish *sost* ortholog annotated as ENSDARG00000061259 was identified on chromosome 12, spanning a 4kb region (28,902,441-28,906,682). The size of the orf is 630bp in two exons and the deduced protein consists of 210 aa. The protein alignment of zebrafish Sost (DrSost) with orthologs in human (HsSost; ENSG00000167941), mouse (MmSOST; ENSMUSG00000001494), chicken (GgSost; ENSGALG00000009929) and Xenopus (XtSostdc1; ENSXETG00000022798) showed an overall conservation of Sost (Fig. 10B), which is lower than for Lrp5. However, eight cysteine residues relevant for the tertiary cys-knot structure of Sost (Weidauer et al., 2009) are highly conserved in all species analyzed (Fig. 10B; and data not shown). Pairwise alignments revealed sequence identities of 54% with HsSost, 49% with MmSost, 59% with GgSost and 45% with XtSostdc1, respectively. Taken together, both *lrp5* and *sost* genes are conserved during vertebrate evolution, with an *lrp5* ortholog existing in invertebrates (*arrow*, in Drosophila).

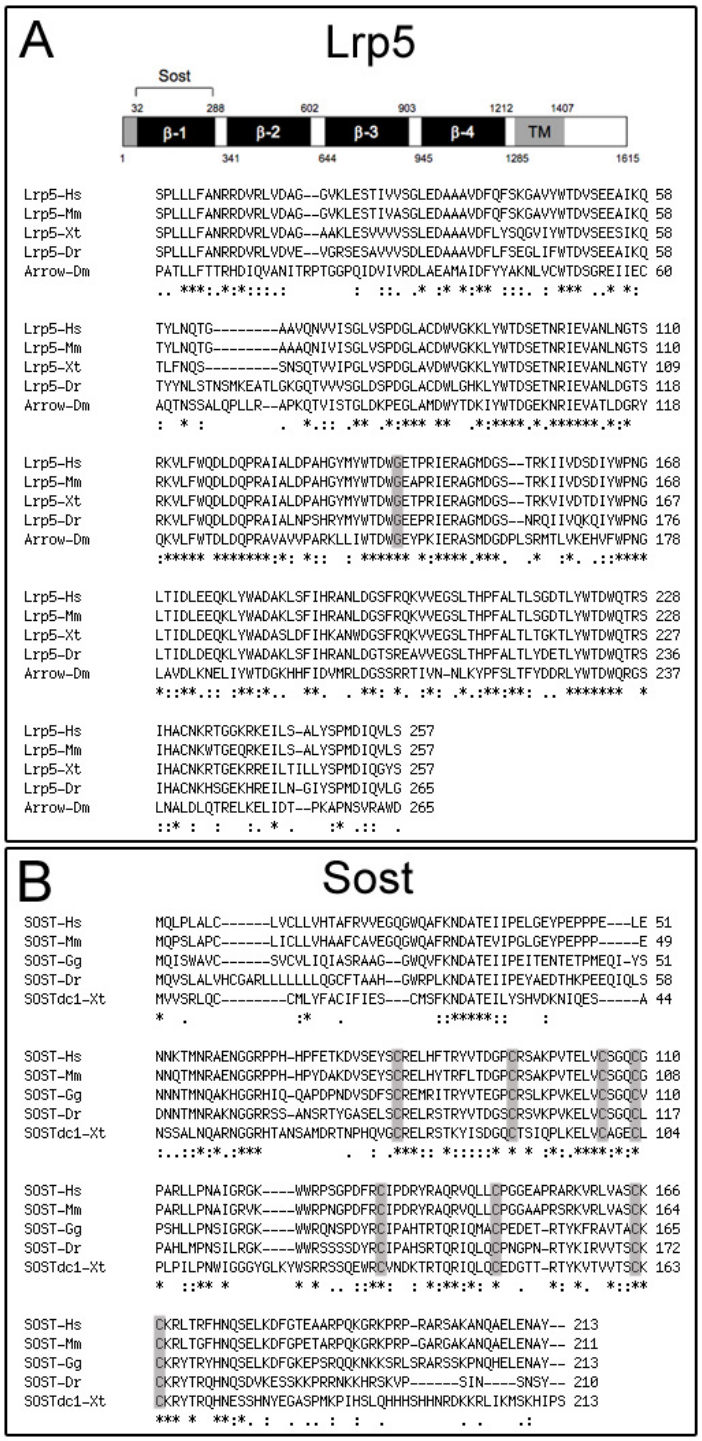

Fig. 10. Lrp5 and Sost are conserved at the sequence level. Alignment of Lrp5 and Sost amino acid sequences. (**A**) Schematic illustration of predicted Lrp5 protein domains (top). Numbers indicate amino acid positions and refer to human Lrp5. Grey boxes represent signal peptide (1-32) and transmembrane domain (TM), respectively. β-1 to β-4 indicate β-propeller domains 1 to 4. The β-1 domain is proposed to bind to Sost. Bottom: Alignment of amino acid sequences in the β-1 domain. Glycine at position 171, which is mutated to valine in human patients with high bone mass phenotypes (Boyden et al., 2002) is highlighted in grey. (**B**) Amino acid alignment of Sost proteins. Cysteine residues at conserved positions are highlighted in grey.

3.2.2. Complementary and overlapping expression of Lrp5 and its putative inhibitor Sost during cranial skeleton development in zebrafish

3.2.2.1. Early expression of zebrafish *lrp5* and *sost*

In situ hybridization with antisense probes targeting *lrp5* and *sost* mRNA indicated that both genes are maternally expressed in zebrafish. At the 8-cell stage, strong staining was observed for *lrp5* (Fig. 11A) and *sost* (Fig. 11F). During late epiboly/bud stage and 10 somite stage (ss/14 hpf) *lrp5* is ubiquitously expressed (Fig. 11B,C). Around 20 ss, the ubiquitous *lrp5* expression gets restricted and becomes concentrated in the CNS (arrowhead in Fig. 11D; Fig. 11E) and tail region (arrow in Fig. 11D). In contrast, zygotic *sost* is not expressed during epiboly stages (Fig. 11G). Earliest embryonic *sost* expression can be detected around 10 ss as two bilateral patches in the posterior head region (arrows in Fig. 11H,I). Subsequently, the pattern is complemented by a medial stripe along the hindbrain that is observed at 25 ss (black arrowheads in Fig. 11J,K; Fig. 11L). At this stage, the lateral stripes fused at the ventral side of the head (white arrowhead in Fig. 11J,K) and *sost* expression can also be seen in ventral mesoderm cells posterior to the yolk extension (arrow in Fig. 11J,K). To illustrate the dynamics of the *sost* expression pattern in the hindbrain during these stages, a series of flat-mount preparations was analyzed between 10 and 25 ss (Fig. 11M*i-vi*). I observed that during successive stages (indicated by body axis growth; Fig. 11M*i-vi*, top), the medial expression intensifies (Fig. 11M*i-iii*) and divides into two bilateral domains (Fig. 11M*iv*), which gradually move into distal directions to surround the hindbrain ventricle (Fig. 11M*v-vi*).

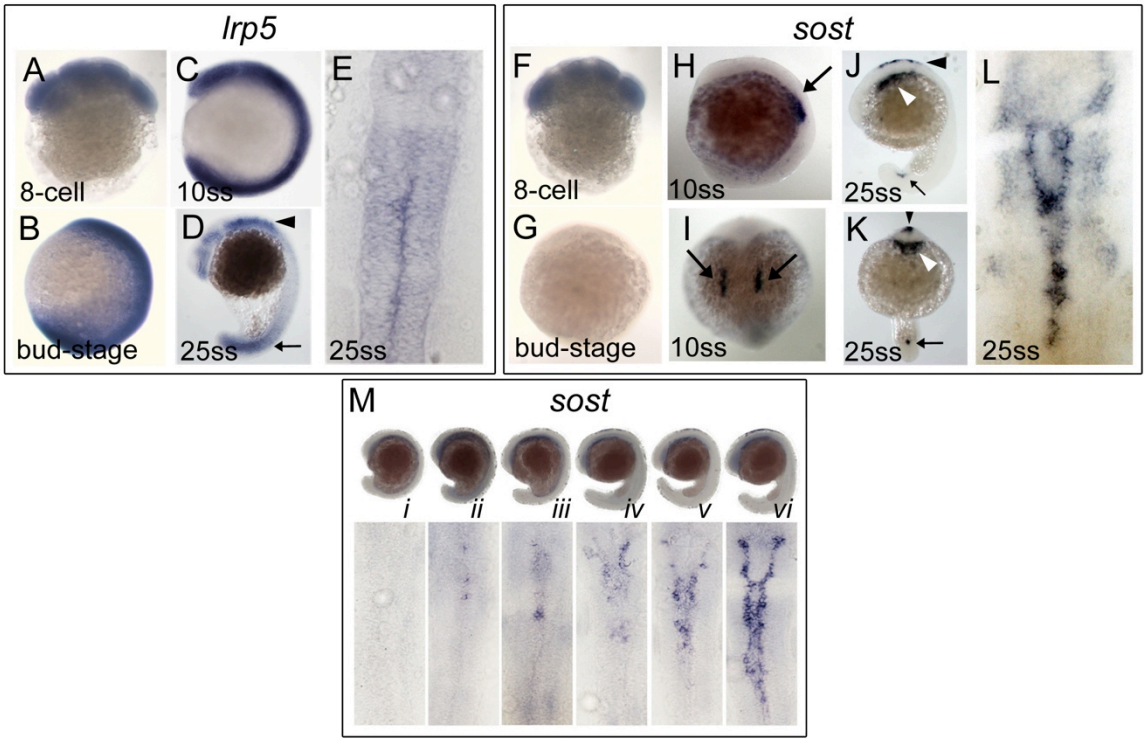

Fig. 11. Early embryonic expression of *lrp5* and *sost*. (**A-D)** Lateral views of embryos showing *lrp5* expression at 8-cell stage (A), bud-stage (B), 10 somite stage (ss) (C), 25 ss (D; arrowhead indicates hindbrain expression, arrow indicates tailbud expression). (**E)** Flat mounted embryo at 25 ss. (**F-K)** Whole mount embryos showing *sost* expression at 8-cell stage (F), bud-stage (G), 10 ss lateral (H) and dorsal (I), 25 ss lateral (J) and frontal (K; black arrowhead indicates hindbrain expression; white arrowhead indicates bilateral ventral expression; arrow indicates ventral mesenchyme). (**L)** Flat mounted embryo at 25 ss. (**M*i*-M*vi*)** Emerging hindbrain expression of *sost* between 12 and 25 ss as whole mounts (top) and flat mounts (bottom). Anterior is to the left in B,C,D,G,H,J,M (top) and to the top in E,I,L,M (bottom).

3.2.2.2. Expression of *lrp5* and *sost* at 24 and 48 hpf

At 24 hpf, expression of *lrp5* is found in the cranial region and in the trunk preferentially in the brain and in the neural tube (Fig. 12A). In the trunk, only weak expression can be detected in the mesoderm and no transcripts are detectable in the notochord and the finfold ectoderm (Fig. 12A'). In the head however, highest levels of expression are found in the hindbrain (Fig. 12B), whereas lower expression is also seen in the diencephalon and the mid-hindbrain boundary region, except in the dorsal-most regions (Fig. 12A). No obvious expression is found in the tectum and telencephalon (Fig. 12A).

Sost expression is evident in a well defined row of cells that lines the hindbrain ventricle dorsally and also in the ventral head region (Fig. 12C). In the trunk, *sost* is expressed ventral to the notochord, with increased levels in the ventral mesenchyme caudal to the yolk extension (Fig. 12C'). The pattern of *sost* expression around the hindbrain ventricle is limited anteriorly by the rhombic lip (Fig. 12D). Intermediate levels of expression are found throughout the entire CNS (Fig. 12C). In the ventral head region, *sost* is expressed in the pharyngeal arch region where postmigratory neural crest cells are located (Fig. 12C,D').

At 48 hpf, strong *lrp5* expression persists in the head region and weaker expression is observed in the trunk (Fig. 12E). Also the pectoral fin buds show *lrp5* expression (arrows in Fig. 12E). *Lrp5* is found broadly expressed in the dorsal neural tube (Fig. 12F, arrow) and ventral to the notochord (arrowhead in Fig. 12F). Broad expression is found throughout the head with elevated levels in the dorsal hindbrain (Fig. 12G,H) and in the diencephalon (arrow in Fig. 12G). In contrast, expression is weak or absent in the tectum and telencephalon. *lrp5* is also strongly expressed in the presumptive ventral mesenchyme (arrowhead in Fig. 12G; Fig. 12G'). The *lrp5* expression pattern in the hindbrain was next analyzed in transverse sections. The cells generating the bilateral domains are positioned in the dorsal-most layer of the hindbrain (Fig. 12H,I) and join at its posterior end (Fig. 12H,J). In both sections, also *lrp5* positive cells in the pharyngeal arches are visible (arrowheads in Fig. 12I,J).

sost expression at the same stage is more restricted and most prominent in the head region (Fig. 12K). Expression of *sost* is also found in a segmental pattern in the trunk (arrowhead in Fig. 12L). Cross-sections revealed that *sost* expressing cells are flanking the neural tube in regions where neural arches develop in later stages (arrowheads in Fig. 12L'). The *sost* expressing cells are also visible in the pharyngeal arches in the anterior section (arrowhead in Fig. 12M and Fig. 12M'). The border-like pattern around the hindbrain persists (Fig. 12M,N). Unlike the broad expression of *lrp5* in this region, *sost* is expressed only in a subset of cells in these *lrp5* domains (compare Fig. 12H to N). Transverse sections show that the *sost* positive cells are also positioned at the

dorsal-most edges of the hindbrain (Fig. 12N,O) and that these domains like for *lrp5* join at the posterior end of the hindbrain (Fig. 12N,P). Notably, in both structures, hindbrain and pharyngeal arches, *lrp5* and *sost* are co-expressed. However, *lrp5* shows a broader expression while *sost* is confined to a few cells within the cluster of *lrp5* positive sells.

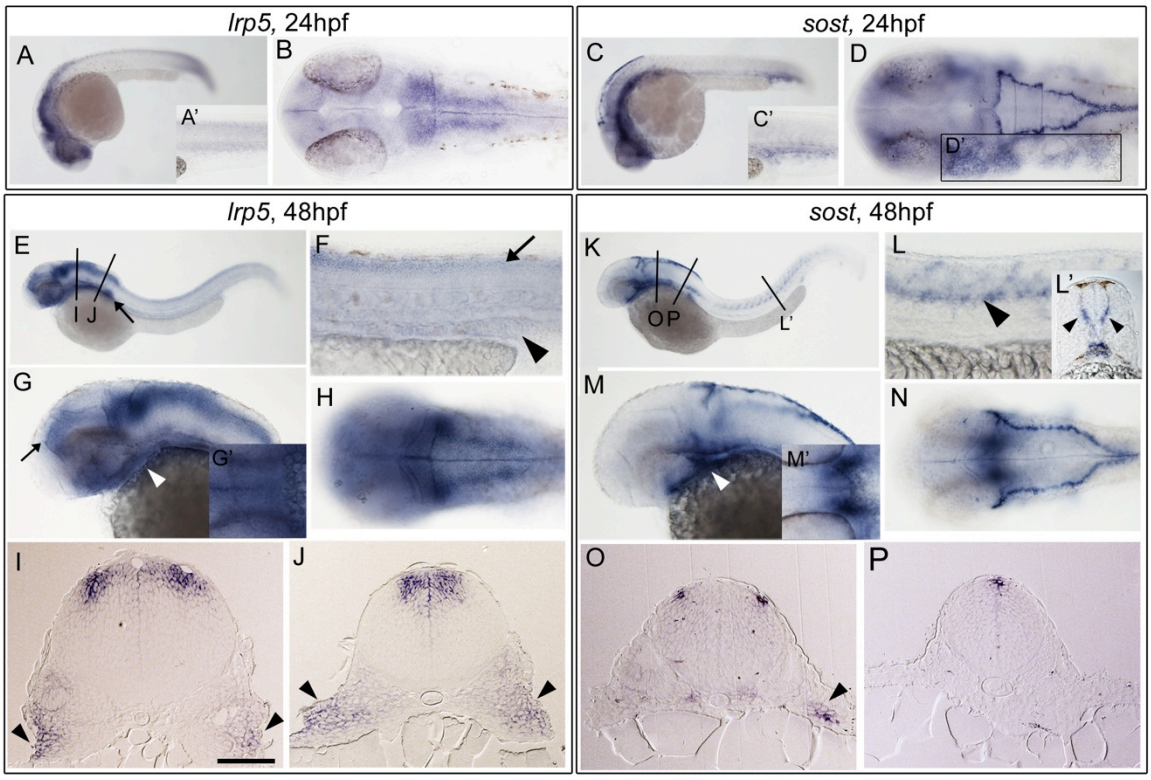

Fig. 12. *lrp5* and *sost* expression at 24 and 48 hpf. (**A**) Lateral view of *lrp5* expression seen in whole mount embryo at 24 hpf. (**A'**) Higher magnification view of trunk region. (**B**) Dorsal view of head. (**C**) Lateral view of *sost* expression at 24 hpf. (**C'**) Trunk region at higher magnification. (**D**) Dorsal view of head. (**D'**) Inset showing plane of focus on post-migratory neural crest streams. (**E-H**) Whole mount embryos showing *lrp5* expression at 48 hpf (E; arrow points to pectoral fin bud). (**F**) Lateral view of trunk at higher magnification (arrow indicates expression in dorsal neural tube; arrowhead points to ventral expression). (**G**) Lateral view of head (arrow indicates epiphysis; arrowhead pharyngeal arch region; inset in G' shows ventral view of pharyngeal arch region). (**H**) Dorsal view of head showing broad distribution of *lrp5* transcripts. (**I,J**) Transverse plastic sections at levels indicated in E, arrowheads point to pharyngeal arches; scalebar in I = 50 µm. (**K-N**) *sost* expression in whole mount embryos. (**L**) Higher magnification of trunk. Inset in (**L'**) shows cryosection at position indicated in K (arrowheads mark *sost* expression adjacent to ventral neural tube). M. lateral view of head (arrowhead indicates *sost* expression in presumptive ventral head mesenchyme; inset in M' shows ventral view of pharyngeal arch region). (**N**) Dorsal view of head. (**O,P**) Transverse plastic sections at levels indicated in K, arrowhead in O points to *sost* expression in pharyngeal arches. Anterior is to the left in all whole mount pictures.

3.2.2.3. Expression of *lrp5* and *sost* at posthatching stages

At 72 hpf, both *lrp5* and *sost* expressions become more restricted to distinct domains. *Lrp5* is strongly expressed in the head (Fig. 13A,B) as well as the pectoral fins (arrows in Fig. 13B). In the head, expression is found prominently in the dorsal hindbrain (white arrowhead in Fig. 13C; arrow D) including the rhombic lip, as well as in the epiphysis (arrow in Fig. 13C). No expression is evident in the tectum and telencephalon. Strong expression is also found throughout the forming pharyngeal skeleton in the ventral head region (black arrowhead in Fig. 13C; Fig. 13C'). Transverse sections show the broad expression of *lrp5* in this region (arrowhead in Fig. 13D). Sections through the hindbrain highlight that this expression persists but appears fainter than at 48 hpf (compare Fig. 13E,F to Fig. 12I,J). The same sections also reveal strong expression of *lrp5* in the pectoral fin (arrowhead in Fig. 13F).

At the same stage, *sost* is no longer expressed in the hindbrain and its expression is limited to the ventral head region (Fig. 13G,H) and the pectoral fin (arrows in Fig. 13H). In contrast to the broad *lrp5* expression, *sost* expression is confined to cartilaginous cranial neural crest cell (CNCC) derivatives. At this stage, the morphogenesis of the ventral cranial skeleton has advanced and single elements are distinguishable as they distinctively express *sost*. Meckel's cartilage (arrow in Fig. 13I), ceratohyal (white arrowhead in Fig. 13I,I') and the distal parts of ceratobranchials (black arrowhead in Fig. 13I,I') are visible. Transverse sections at the level of the ceratobranchials show that *sost* expression is confined to the innermost cartilaginous cells (arrowhead in Fig. 13J). At this stage, sost expression is also found in cartilaginous structures dorsal to the mouth cavity i.e. the palate (arrow in Fig. 13J) More caudal sections confirm that expression in the hindbrain has vanished (Fig. 13K,L,).

At 7 dpf, expression of *lrp5* is found exclusively in the head (Fig. 13M,N). Expression in the dorsal hindbrain persists but has changed its pattern along with the hindbrain morphology. It is visible in the rhombic lip (white arrowhead in Fig. 13O) and epiphysis (arrow in Fig. 13C). Furthermore, broad *lrp5* expression can be found in all structures of the ventral cranial skeleton

(arrowhead in Fig. 13O; Fig. 13O') and the ethmoid plate (asterisk in Fig. 13O). Sagittal (Fig. 13P) and transverse (Fig. 13R) sections through the ceratobranchials show expression of *lrp5* throughout the extensions of these structures (cartilage of the gill filaments). It is not overlaying with cartilaginous elements that directly derive from NCCs as evident by comparison with a DAB stained *sox10:GFP* larva in the same stage (Fig. 13Q). Expression is also evident throughout the pectoral fins and concentrated in a basal line, presumably the scapulocoracoid (Fig. 13S).

Sost expression at this stage is confined to the ventral cranial skeleton in a much more restricted pattern than *lrp5* (Fig. 13T,U). Expression is absent in the hindbrain (Fig. 13V) but strong in parts of Meckel's cartilage (arrow in Fig. 13V) as well as in the ceratobranchials (arrowhead in Fig. 13V; Fig. 13V'). Sagittal (Fig. 13W) and transverse (Fig. 13X) sections show that *sost* expression is confined to cells within the distal tips of the gill filaments comparable to *lrp5* (compare Fig. 13W to P). However, *sost* expression is excluded from the surrounding epithelial cells. In the pectoral fins, *sost* expression is limited to the endochondral disc (Fig. 13Y).

Taken together, the spatiotemporal expression ananlysis of *lrp5* and *sost* suggest that both genes functionally interact also in zebrafish as has been shown in mammals. However, in zebrafish, the embryonic expression patterns in the brain, ventral head mesenchyme and its derivatives suggest that their function might also be required for mechanisms in early cranial morphogenesis, other than in mammals where both factors have been implicated in bone homeostasis. Interestingly, the spatial correlation of the expression patterns seems to follow a general principle: *lrp5* is expressed in broader domains while its putative inhibitor *sost* is confined to smaller domains overlapping with *lrp5* expression.

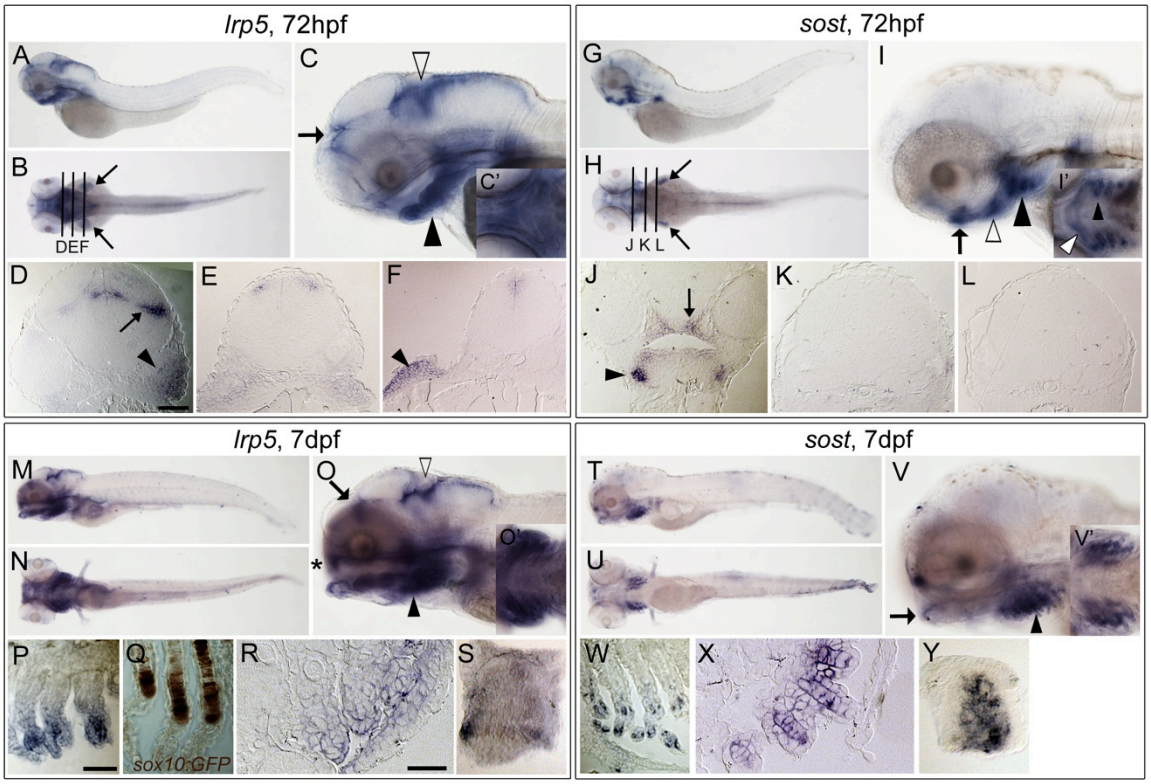

Fig. 13. Expression of *lrp5* and *sost* at 72 hpf and 7 dpf. (**A-C)** *lrp5* expression in whole mount embryos at 72 hpf; lateral view in A, dorsal view in B (arrows point to pectoral fin buds), higher magnification lateral view of head in C (arrow points to epiphysis; white arrowhead to mid-hindbrain boundary and black arrowhead to jaw). (**C')** Ventral view of pharyngeal arch region. (**D-F)** Transverse plastic sections at levels indicated in B (arrow in D points at rhombic lip; arrowhead on ventral mesenchyme; arrowhead in F indicates pectoral fin bud; scalebar in D = 50 µm). (**G-I)** *sost* expression in whole mount embryos at 72 hpf (arrows in H point to pectoral fin buds). (**I)** Lateral view of head (arrow indicates Meckel's cartilage; white arrowhead ceratohyal; black arrowhead ceratobranchials). I'. Higher magnification ventral view of pharyngeal arch region (arrowheads as in I). (**J-L)** Transverse plastic sections at levels indicated in H (arrowhead in J points on forming ceratobranchial; arrow on palate). (**M-S)** *lrp5* expression at 7 dpf. (**M)** Lateral view. (**N)** Ventral view. (**O)** Lateral view of head at higher magnification (asterisk indicates ethmoid plate; arrow points to epiphysis; white arrowhead to mid-hindbrain boundary and black arrowhead to gills). Inset (**O')** shows higher magnification view of ventral head region. (**P,Q)** Sagittal cryosections through pharyngeal arch region showing *lrp5* expression (P; scalebar = 10 µm), and GFP immunostaining in neural crest derived cartilage in a *sox10:GFP*-larva (Q). (**R)** Transverse plastic section at level of ceratobranchials showing *lrp5* expression; scalebar = 20 µm. (**S)** Flat mounted pectoral fin. (**T-Y)** *sost* expression at 7 dpf in lateral (T) and ventral view (U), and as higher magnification view of head (V; arrow shows Meckel's cartilage; arrowhead points to pharyngeal arches; V' magnification of ventral head region). Cryo sagittal (W) and plastic transverse (X) sections through the ceratobranchials. (Y). Flat mounted pectoral fin.

3.2.3. *sost* but not *lrp5* expression is controlled by FGF signaling

In order to test whether *lrp5* or *sost* expression is regulated by FGF, embryos were treated with the FGF inhibitor SU5402 (Mohammadi et al., 1997) for 3 hours between the 14 and 20 ss. Subsequently, larvae were fixed and subjected to *in situ* hybridization to check for alterations in the expression patterns of *lrp5* and *sost*. No changes in the *lrp5* expression pattern could be observed in SU5402 treated embryos (Fig. 14B; n = 26) compared to DMSO controls (Fig. 14A; n = 24). However, for *sost* expression significant differences were observed. 100% of DMSO treated embryos (n = 69) showed wild-type expression of *sost* (Fig. 14C,E-G), while 94% of SU5402 treated embryos (n = 82) showed a substantial reduction of the ventral *sost* domain (compare asterisks in Fig. 14D,H to arrows in Fig. 14C,E), whereas the dorsal stripe remained unaffected in most cases (compare arrowheads in Fig. 14C,E to Fig. 14D,H). Detailed views of the hindbrain (compare Fig. 14F,I) show no alteration while close-ups of the ventral part (compare Fig. 14G,J) indicate the loss of ventral *sost* expression upon SU5402 treatment.

Taken together, these experiments suggest that *sost* expression but not *lrp5* expression is controlled by Fgf signaling. This is particularly intersting, since Fgf signaling has been shown to be one of the key players in craniofacial morphogenesis (Crump et al., 2004; Hall et al., 2006; Walshe and Mason, 2003). Furthermore, these data suggest a novel link between Wnt and Fgf signaling in this process. Thus, the presented results will allow further insight into the complex signal transduction cascades that drive cranial morphogenetic events.

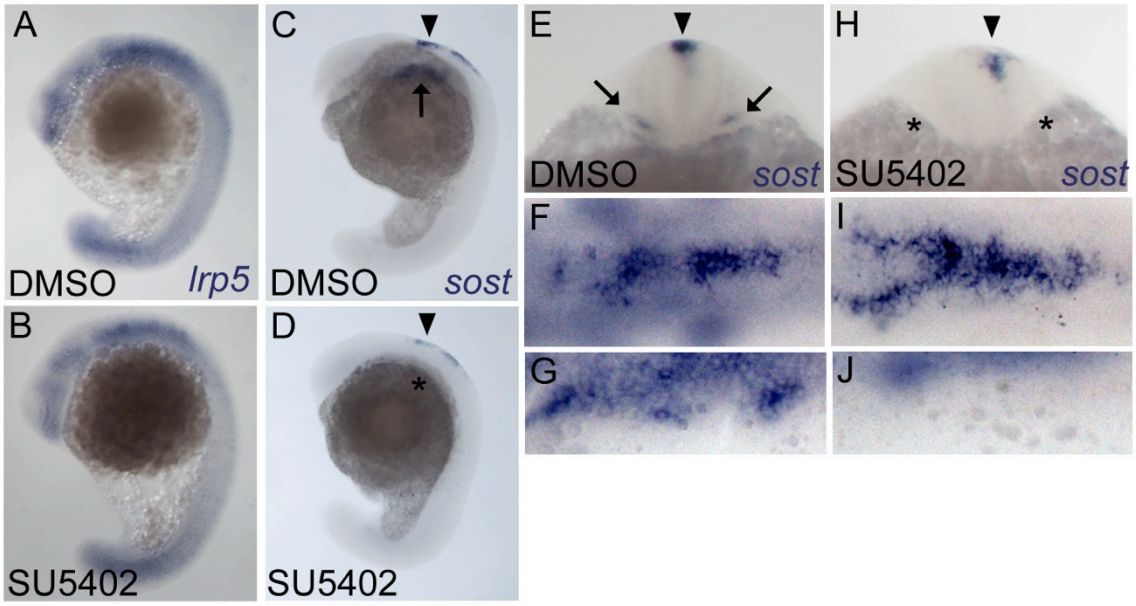

Fig. 14. *sost* but not *lrp5* expression is dependent on Fgf signaling. (**A,B)** *lrp5* expression in whole mount embryos at 20 ss. DMSO control (A) and SU5402 treated embryo (B). Note that controls and treated individuals show no difference in *lrp5* expression. (**C-J)** *sost* expression in embryos at 20 ss. Lateral (C,D) and frontal (E,H) views of whole mount preparations. F,I,G,J show higher magnification dorsal views with focal plane on dorsal (F,I) and ventral (G,J) *sost* expression domains in head. C,E-G. DMSO treated control embryos. D,H-J. SU5402 treated embryos. Note reduced *sost* expression in ventral but not dorsal domains in SU5402 treated embryo. Data were obtained from three independent experiments, representative examples are shown.

3.2.4. *lrp5* gene knock-down leads to defects in hindbrain and CNCCs

To analyze the role of *lrp5* during zebrafish embryogenesis, I carried out a Morpholino oligonucleotide (Mo) knock-down approach. Different combinations and concentrations of Mos targeting the splice donor site of the 2nd intron (*lrp5*MoUp) as well as the splice acceptor site (*lrp5*MoDown, Fig. 16A) were tested for efficacy. All used Mo combinations resulted in distinct phenotypes (Fig. 16H,I; see page 65 for detailed explanation) in a concentration dependent manner (Fig. 15; Table 2). The most efficient approach was a combination of *lrp5*MoUp and *lrp5*MoDown both in a concentration of 0.3 mM as it resulted in the highest ratio of classI defective embryos (Fig. 15). This setting was used for all experiments described below and henceforth addressed as *lrp5*Mo. Individual injection of *lrp5*MoUp as well as *lrp5*MoDown also

resulted in a similar phenotype (Fig. 15 column 4,5,7,8; Table 2). This is further proof arguing in favor of the specificity of the knock-down as the probability for the same off-target effects caused by two independent Morpholinos is low. As an additional control, a mismatch Mo with five base replacements to the original sequence of *lrp5*MoUp was designed (*lrp5*MoUpMM). Injection of *lrp5*MoUpMM did not lead to any obvious morphological defects (Fig. 15 column 6; Table 2).

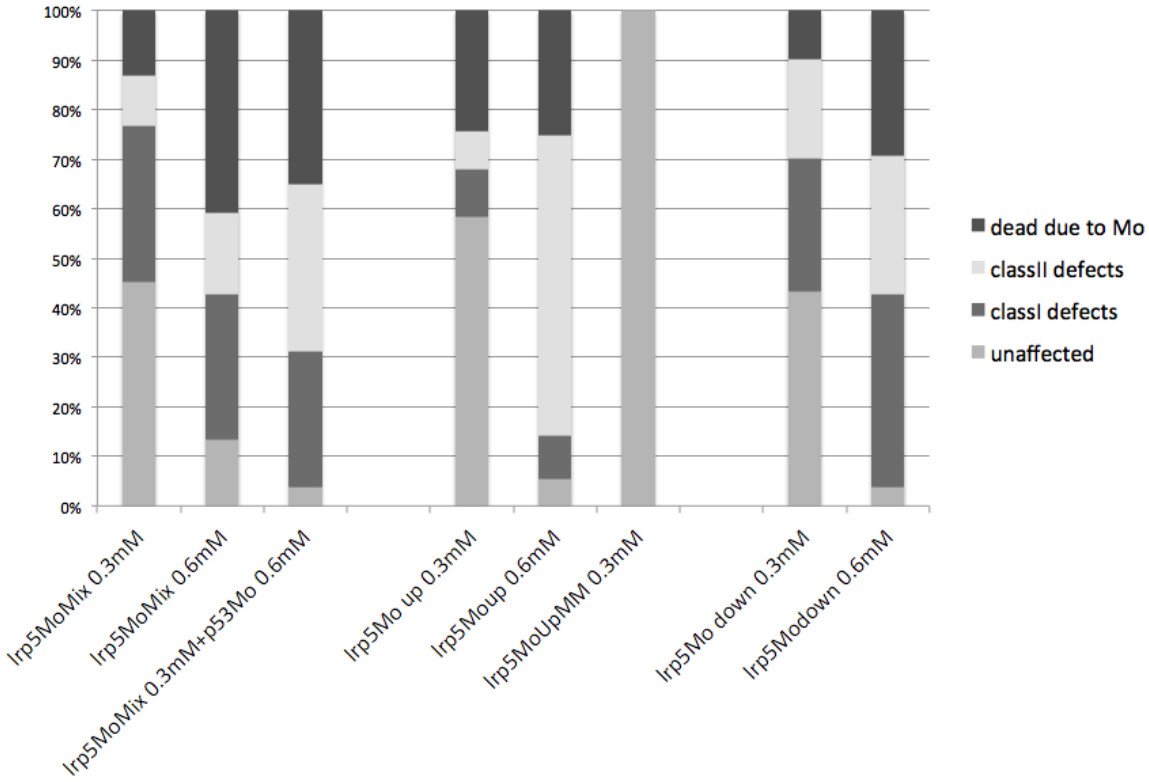

Fig. 15. Knock-down of *lrp5* is dependent on morpholino dose. Graphical interpretation of statistics of *lrp5*Mo injections. For definition of classI and classII defects see page 65 and Fig. 16H,I. For exact numbers see table 2 in appendix on page 95.

To determine efficiency of the Mo mediated knock-down, I used RT-PCR for semi-quantitative analysis of transcript levels (Fig 16B). Choosing a primer combination (primer up + primer down2 in Fig. 16A) to amplify a region of cDNA that covers Exon2 and Exon3 revealed reduced levels of correctly spliced *lrp5* cDNA in the morphant (lane 3 in Fig. 16B) compared to wild-type

(lane 1 in Fig. 16B) and control morphant (*mm*Mo; lane 2 in Fig. 16B). Moreover, a second weaker band at slightly higher position became visible in the morphant lane, suggesting an alternatively spliced product. Additionally, the same cDNAs were tested for quantities of unspliced transcripts using the primer combination primer up and primer down1 (Fig. 16A). In this case, the amount of PCR product was substantially higher in the morphant situation (lane 6 in Fig. 16B) compared to wild-type (lane 4 in Fig. 1B) and mismatch Mo (lane 5 in Fig. 16B). No changes were seen between the levels of β-actin cDNA in the different entities (lane 7-9 in Fig. 16B).

Consistent with the expression of *lrp5* in the hindbrain (see 3.2.1; 3.2.2), I found this organ severely affected in *lrp5* morphant embryos at 48 hpf. Compared to the wild-type control (Fig. 16C), *lrp5* morphants were characterized by widely inflated hindbrain ventricles (Fig. 16D).

CNCCs are known to originate in the dorsal hindbrain and form substantial parts of the cranial skeleton. Hence, I checked for the morphology of the ventral cranial skeleton structures at advanced larval stages by bone/cartilage staining. While the wild-type (Fig. 16F) and mismatch morphant skeletons (Fig. 16G) appeared normally developed (compare to schematic illustration in Fig. 16E), *lrp5* morphants exhibited severe malformations (Fig. 16H,I). I distinguished between two classes of severity (see injection statistics in Table 2 and Fig. 15). ClassI morphants were characterized by complete loss of ceratobranchials 1-4 (arrowhead in Fig. 16H) and a reverse oriented ceratohyal. The 5th ceratobranchials with attached pharyngeal teeth was still present (arrow in Fig. 16H). In the more affected classII morphants, only rudiments of the ventral craniofacial skeletal structures such as Meckel's cartilage or ceratohyal remained while the 1st till 5th ceratobranchials were completely missing (arrowhead in Fig. 16I).

Recent reports about unspecific apoptosis in the course of Mo mediated knock-down experiments (Robu et al., 2007) raised the necessity to assess possible off-target effects in the *lrp5* knock-down situation. It has been shown that unspecific apoptosis is mainly mediated by the cell cycle

master regulator p53 and consequently knock-down by *p53*Mo can reduce or rescue this effect. To ensure that the *lrp5* loss-of-function phenotype is specific, I also checked for the structure of the cranial skeleton after compound knock-down of *lrp5* and *p53*. As evident by cartilage staining, the same defects can be seen (Fig. 16J) in a comparable statistical distribution as occurs upon normal *lrp5*Mo injection (Table 2 and Fig. 15; row/column 3). Thus, the observed *lrp5* morphant phenotype is specific and not caused by off-target defects due to Morpholino injection. A more detailed analysis was undertaken using toluidine blue stained cross sections through wild-type and classI morphant larvae (Fig. 16K-N) at 5 dpf. Wild-type larvae showed well differentiated cartilaginous arches at this stage (Fig. 16K). In the morphant situation, however, although pharyngeal cartilages are present and well differentiated in some areas, their number, shape and position seems to be aberrant and hence their identification is difficult, with exception of the hyosymplectic (Fig. 16L). In terms of dentition, cross sections interestingly showed no malformations in these structures in the morphants. According to the classification by Huysseune et el. (1998) wild-type larvae at 5 dpf (Fig. 16M) have $3V^1$, $4V^1$ and $5V^1$ tooth structures on each side, with $4V^1$ attached and possessing a replacement tooth, $4V^2$, in early cytodifferentiation. Teeth $3V^1$ and $5V^1$ are in a similar stage at late cytodifferentiation, and do not have a replacement tooth, yet. In *lrp5* morphants (Fig. 16N), the same three teeth are present: $3V^1$, $4V^1$ and $5V^1$. Individuals with tooth $4V^1$ in late cytodifferentiation have teeth $3V^1$ and $5V^1$in morphogenesis stage; individuals with tooth $4V^1$ still in early cytodifferentiation stage have teeth $3V^1$ and $5V^1$ in initiation stage only. Tooth $4V^1$ displays no replacement tooth, but this is not to be expected given that a replacement tooth develops only once its predecessor is attached, which is not yet the case. Thus, analyzing the tooth organization revealed that not all ventral head structures are generally affected in the *lrp5* morphants. Rather, while tooth development was apparently normal, the cartilage elements of the head skeleton, which are CNCC derived, were strongly affected. This opens the possibility that Lrp5 is solely required for morphogenesis of CNCC derived craniofacial structures.

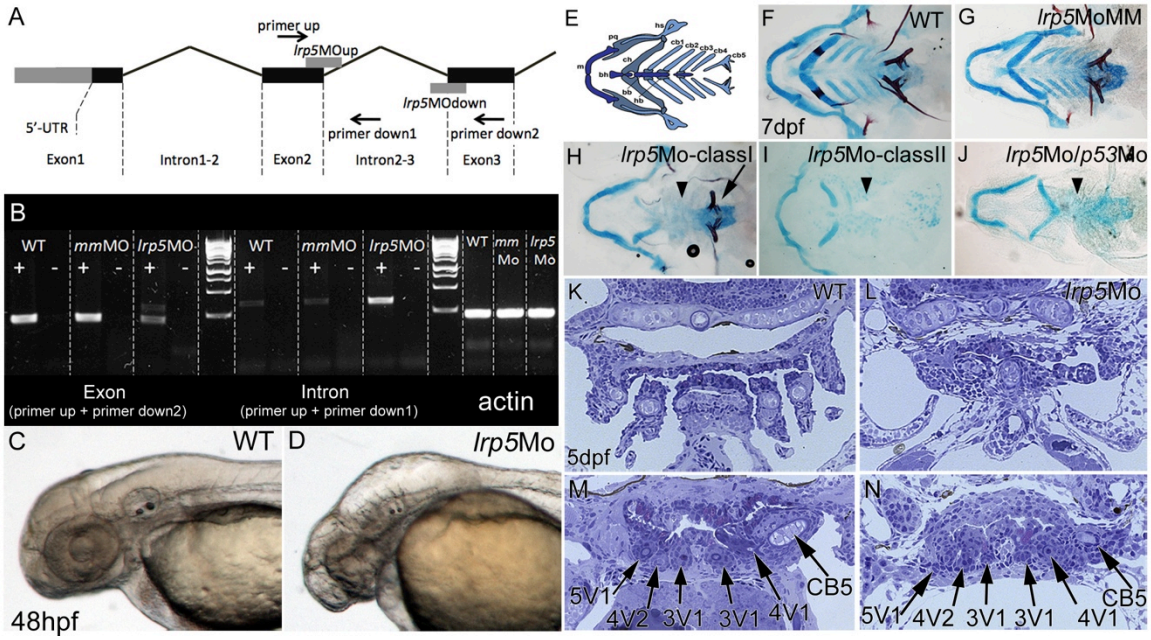

Fig. 16. Knock-down of *lrp5* leads to defects in the craniofacial skeleton, but not the teeth. (**A)** Schematic representation of the *lrp5* transcript and the chosen Mo knock-down strategy. (**B**) RT-PCR on mRNA isolated from morphant embryos, +/- indicates presence or absence of RT enzyme. For use of primercombinations see 3.2.5.3 (**C,D**) Morphology of wild-type vs. *lrp5* morphant embryo at 48 hpf. Note the inflated hindbrain in morphant. (**E**) schematic illustration of viscerocranial skeleton. (**F-J**) Combined bone and cartilage staining at 7 dpf of wild-type (F), *lrp5*MM morphant (G), *lrp5* morphant classI (H), classII (I) and *lrp5/p53* compound morphant (J). Note that morphants show absence of ceratobranchials (arrowheads) while 5th ceratobranchial and pharyngeal teeth (arrow) are present in classI morphants. (**K-N**) cross sections through 5 dpf larvae. Wild-type (K) shows clear distribution of ceratobranchials which is lost in *lrp5* morphant (L). More posterior sections show that both, wild-type (M) and lrp5 morphants (N) have normal establishment of pharyngeal teeth (arrows). Anterior is to the left in C-J.

3.2.5. Knock-down of *lrp5* reduces canonical Wnt signaling activity

According to the proposed function of Lrp5 as a Wnt co-receptor I tested whether reduction of functional Lrp5 would lead to reduced intensity of Wnt signal transduction. TOPdGFP transgenic zebrafish carry a construct expressing destabilized GFP under control of a Lef1/β-catenin responsive promoter (Dorsky et al., 2002). Hence, this line is used as a tool to measure activity of canonical Wnt signal transduction. At around 20 ss, all observed transgenic embryos (n=33) showed strong reporter activity in the midbrain-hindbrain boundary (MHB) region, as well as in the hindbrain and the presomitic mesoderm (PSM) in the tailbud as seen by *in situ* hybridization

using antisense riboprobes against *gfp* transcripts (Fig. 17A,B; see also Dorsky et al., 2002). In *lrp5* morphants, however, 80% (n=51) showed decreased GFP expression in all body parts (Fig. 17C,D), suggesting substantial down regulation of Wnt activity.

To confirm this finding and to specify that Wnt signaling is reduced in neural crest cells, I also examined transcript levels of *lymphoid enhancer-binding factor 1* (*lef1*), a key downstream player in Wnt signal transduction (MacDonald et al., 2009), thus being a suitable indicator of Wnt signaling activity. Importantly, at around 20 ss it is expressed in migratory CNCCs as well as in the tailbud (Fig. 17E). The CNCC expression appears in two bilateral stripes adjacent to the hindbrain (Fig. 17F) as reported earlier (Dorsky et al., 1999). 73% (n=80) of *lrp5*Mo injected embryos showed a substantial reduction in *lef1* expression in all expression domains (Fig. 17G). Especially in the CNCCs *lef1* expression was strongly reduced (Fig. 17H).

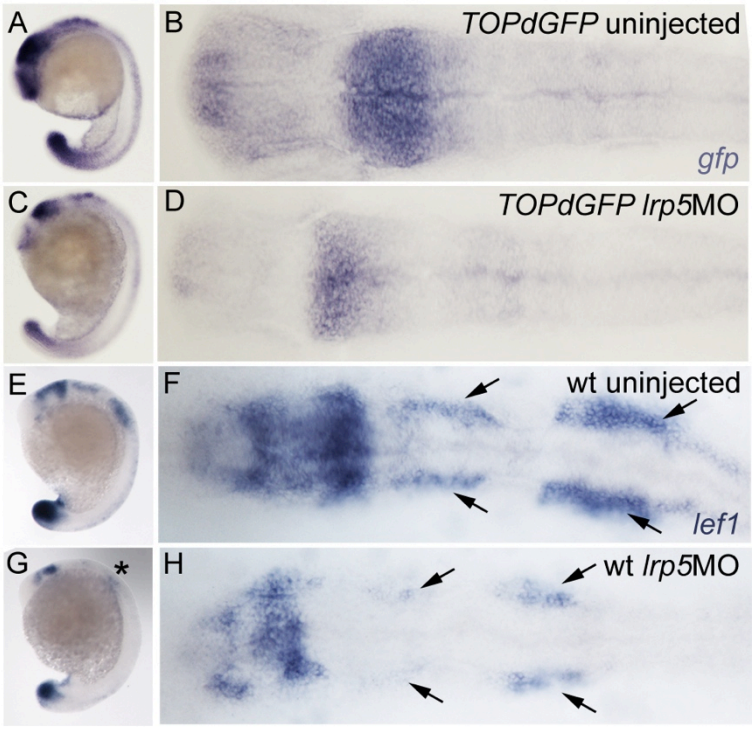

Fig. 17. Knock-down of *lrp5* reduces canonical Wnt signaling activity. (**A-D**) TOPdGFP embryos at around 20 ss stained for *gfp* transcripts. (A,B) Uninjected control, (C,D) *lrp5* morphant. Note that *gfp* expression is downregulated in morphant. (**E-H**) 20 ss embryos stained for *lef1* transcripts. (E,F) Wild-type embryo, (G,H) *lrp5* morphant. Note that *lef1* expression is downregulated in morphant, especially in CNCC regions (see asterisk in G and arrows in F,H). Anterior is to the left in all pictures.

3.2.6. Lrp5 knock-down does not affect induction of CNCCs

Wnt signaling has been shown to play multiple roles in neural crest induction, migration and differentiation (Lewis et al., 2003). In order to examine, whether Lrp5 is important for neural crest induction, I checked for alterations in expression of the early CNCC marker gene *forkhead box d3* (*foxd3*; Kelsh et al., 2000). At 10 ss, premigratory CNCCs express *foxd3* and are found bilaterally to as well as overlying the neuroepithelium at a more caudal part of the hindbrain (Fig. 18A,B). No difference in the expression level or pattern of *foxd3* was observed in *lrp5* morphant embryos (100%, n=28; Fig. 18C,D) compared to the respective wild-type controls (n=32; Fig. 18A,B), indicating that Lrp5 is not involved in early CNCC induction.

3.2.7. Knock-down of *lrp5* affects CNCC migration

Next, I wanted to analyze whether the migratory behavior and pattern of CNCCs is altered by knock-down of *lrp5*. At around 14-15 hpf CNCCs start migrating in three distinct streams lateral to rhombomeres 2, 4 and 6 from dorsal to ventral towards the pharyngeal arch region. At around 20 ss, cells in these streams can be identified by their expression of *distal-less homeobox 2a* (*dlx2a*; Fig. 18E-I; Akimenko et al., 1994) while no expression can be seen in the neuroepithelium (arrow in Fig. 18G and cross-section I). Knock-down of *lrp5* drastically changed the pattern of migratory CNCCs, as streams appeared substantially reduced and disorganized in 45% of morphant embryos (n=64; Fig. 18J,K). Importantly, a patch of *dlx2a* positive cells appeared ectopically on top of the neuroepithelium as evident in cross sections, between the branchial stream of migratory CNCCs at rhombomere 6 (Fig. 18 asterisk in J; K; arrow in L and asterisk in cross-section N). This stream furthermore appeared severely reduced in size (Fig. 18M) compared to wild-type control (Fig. 18H). No changes in the *dlx2a* expression pattern could be found in *lrp5*MoUpMM morphants (n=59; Fig. 24E,F). This experiment suggests that migration of CNCCs in the branchial stream seems to be disturbed by loss of Lrp5 function.

To confirm this finding, migratory CNCCs were also examined by staining for the pan-neural crest marker *crestin* (Luo et al., 2001). In wild-type embryos *crestin* is expressed in cranial and trunk neural crest cells (Fig. 18O). Around 20 ss no stained cells could be seen on top of the neuroepithelium (arrow in Fig. 18Q) but in the two bilateral streams of migratory NCCs (Fig. 18P,Q,R and cross section S). In 55% (n=64) of the *lrp5* morphant embryos, however, the *crestin* expression pattern shows a comparable defect as observed by *dlx2a* staining: Clusters of *crestin* positive NCCs are located on top of the neuroepithelium (arrow in Fig. 18V; asterisk in cross section X) whereas the branchial clusters of *crestin* positive migratory CNCCs appear substantially reduced in size and cell number (Fig. 18W) compared to the wild-type situation (Fig. 18R). No changes in the *crestin* expression pattern could be found in *lrp5*MoUpMM morphants (n=54; Fig. 24G,H).

The effect of *lrp5* knock-down on migratory CNCCs was further confirmed by similar results obtained in *in vivo* experiments using *lrp5* morphants in a *sox10*:GFP transgenic background (Dutton et al., 2008). In this transgenic line, cells of the neural crest lineage are detectable by reporter expression positioned in the migratory streams around 20 ss, while no cells are found in the dorsal hindbrain region (arrow in Fig. 18Y). In contrast, 54% of *lrp5*Mo injected embryos (n=74) showed clusters of ectopic GFP positive cells on the neuroepithelium (arrow in Fig. 18Z) comparable to the results obtained by staining for *dlx2a/crestin* transcripts. Accordingly, the caudal clusters of migratory CNCCs are of smaller size than in the wild-type controls.

Taken together, all three observations indicate that a knock-down of *lrp5* results in alterations of the migratory behavior of CNCCs, while their induction is not affected. Although the observed ectopic cells have some migratory CNCC character as evident by *dlx2a* expression, not all of them join and follow the migratory streams but seem to be retained in the dorsal neuroepithelium where branchial CNCCs are known to originate (Berndt and Halloran, 2006).

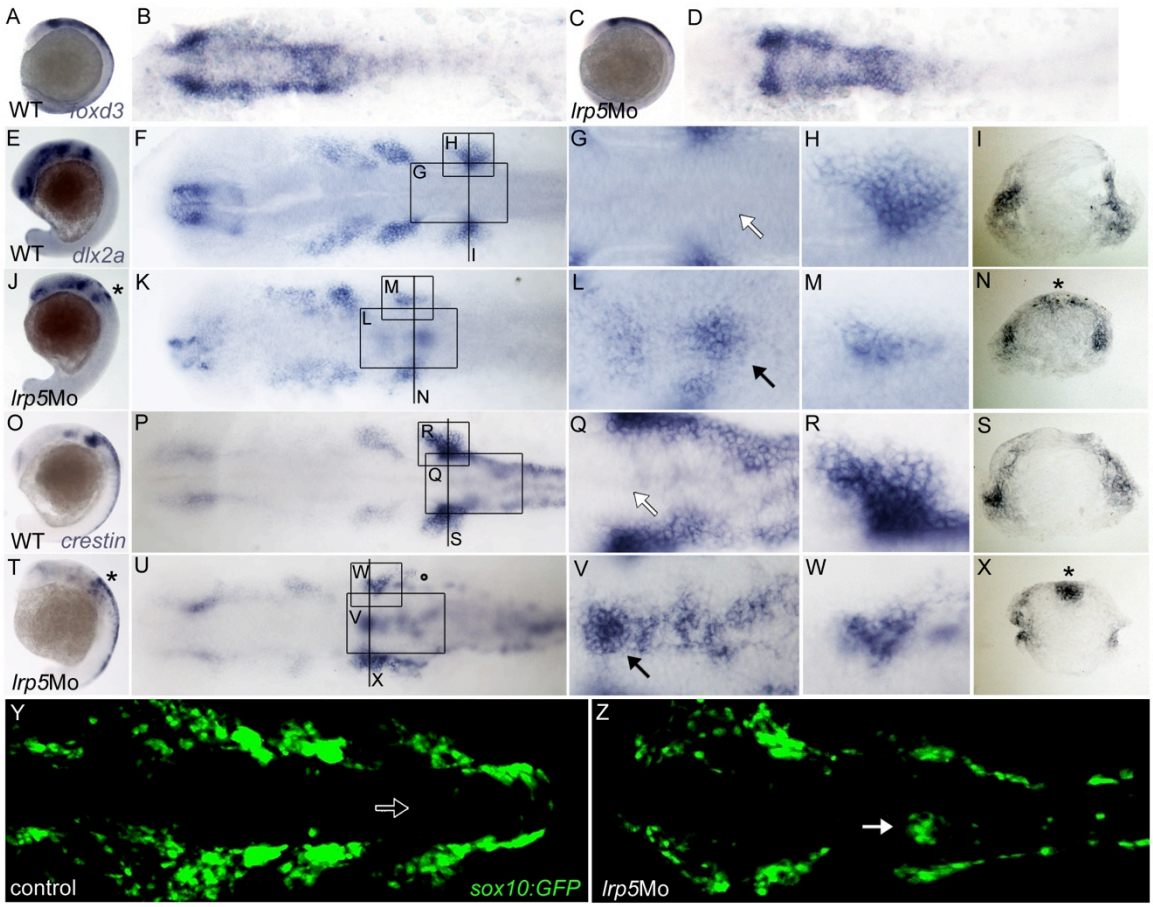

Fig. 18. *lrp5* morphants display normal induction but defective migration of CNCCs. (**A-D**) Embryos at 10 ss stained for *foxd3* transcripts. (A,B) Wild-type embryo, (C,D) *lrp5* morphant. Note that no alteration in *foxd3* expression can be seen. (**E-N**) Embryos at 20 ss stained for *dlx2a* transcripts. (E-I) Wild-type embryo, (J-N) *lrp5* morphant. Note that ectopic *dlx2a* expression is present at the dorsal neuroepithelium of rhombomere 6 in *lrp5* morphants (asterisk in J,N; arrow in L) and the streams of branchial migratory CNCCs are reduced in size (M). (**O-X**) Embryos at 20 ss stained for *crestin* transcripts. (O-S) Wild-type embryo, (T-X) *lrp5* morphant. Note that ectopic *crestin* expression is present at the dorsal neuroepithelium of rhombomere 6 in *lrp5* morphants (asterisk in T,X; arrow in V) and the streams of branchial migratory CNCCs are reduced in cell number (M). (**Y,Z**) Confocal projections of *sox10*:GFP embryos at 20ss showing reporter expression in CNCCs. (Y) Uninjected control embryo, (Z) *lrp5* morphant. Note that ectopic GFP+ cells are present at the dorsal neuroepithelium of rhombomere 6 in *lrp5* morphants (arrow) and the streams of branchial migratory CNCCs are reduced in cell number. Anterior is to the left in all pictures, except cross section. Magnifications in G,H,L,M,Q,R,V,W are indicated by boxed areas in F,K,P,U. Positions of cross sections in I,N,S,X are indicated by lines in F,K,P,U.

3.2.8. Proliferation of premigratory CNCCs is affected by knock-down of *lrp5*

From the previous findings it was not conclusive if knock-down of *lrp5* only affected the migratory behavior of CNCCs or also their total number. Premigratory NCCs are highly proliferative and canonical Wnt signaling has been shown to control the NCC cell cycle (Burstyn-Cohen et al., 2004). Furthermore, it has been reported that avian NCC delamination is tightly synchronized with the cell cycle (Burstyn Cohen and Kalcheim, 2002). I assessed the proliferative status of neuroepithelium cells in rhombomeres 4 to 8 in *lrp5* morphant embryos at 20 ss by immunohistochemical staining for phosphorylated Histone 3 (pH3), which is a marker for M-phase nuclei (Fig. 19A,A',B,B'). In *lrp5* morphant embryos the number of positively stained nuclei was reduced by an average of 37% compared to wild-type controls ($P<10^{-6}$; n=11) in the respective region of interest (roi; Fig. 19C).

To get a better picture about the situation of cells in the DNA synthesis (S) phase of the cell cycle I checked for Bromodeoxyuridine (BrdU) incorporation in *lrp5* morphants at the same developmental stage. As it had been reported in chicken, NCCs synchronize in S-phase for delamination from the neuroepithelium (Burstyn Cohen and Kalcheim, 2002), thus being a prerequisite for the migratory process. In *lrp5* morphants, I found significantly less cells staining positive for incorporated BrdU (Fig. 19D,D',E,E'). In the area between rhombomere 4-8, I determined a 36% reduction of S-phase nuclei ($P=1.05\text{x}10^{-6}$; n=11; Fig. 19F).

In order to further examine which phase of the cell cycle is affected by *lrp5* knock-down I checked for *cyclin d1* (*ccnd1*) transcript levels. *ccnd1* is expressed in G1 phase and is responsible for G1/S-transition. It has been shown to be expressed under transcriptional control of Wnt signaling (Tetsu and McCormick, 1999), also in the zebrafish neural crest (Berndt and Halloran, 2006). Surprisingly, *ccnd1* was substantially up-regulated in the hindbrains of 68% (n=22) of *lrp5* morphant embryos (Fig. 19G-J). Despite a possible conflict with previous reports, this experiment nevertheless strongly supports my previous data and suggests a possible G1 cell cycle

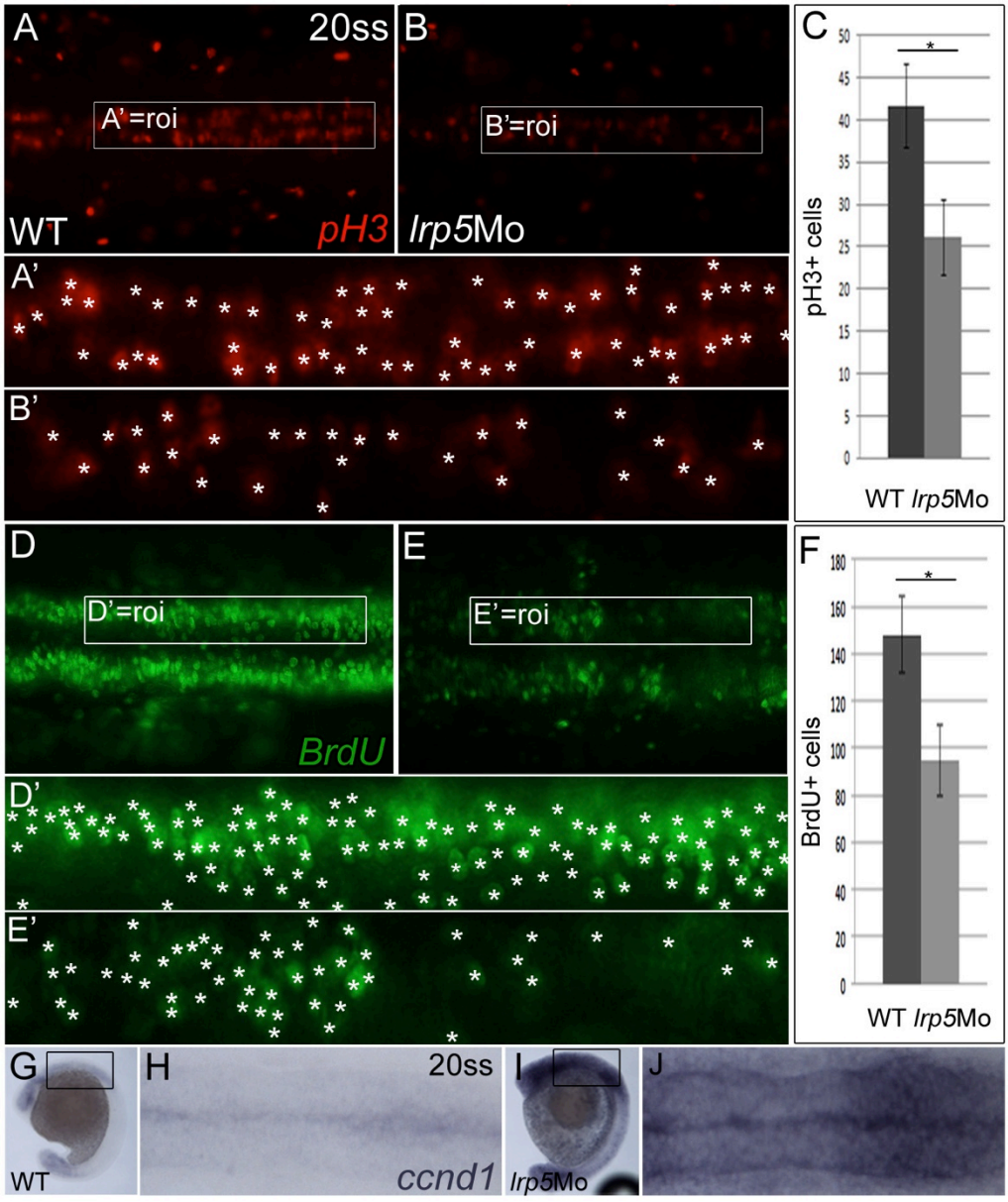

Fig. 19. Proliferation of premigratory CNCCs is affected by knock-down of *lrp5*. (**A,B***)* 20 ss embryos stained for pH3+ cells in M-phase. (A) Wild-type embryo, (B) *lrp5* morphant. Frames demarcate area of cell count (roi, region of interest) and are magnified in (**A',B'**) to examplify counting mode (cells indicated by asterisks). Note that in the *lrp5* morphant pH3+ cells are reduced in number. (**C**) Quantification of pH3+ cell numbers in the neuroepithelium of rhombomeres 4-6. n=9/11 (wild-type/*lrp5* morphant). **P*<10^{-6}, *t*-test. (**D,E**) 20 ss embryos stained for BrdU incorporation. (D) Wild-type embryo, (E) *lrp5* morphant. Frames demarcate area of cell count (roi) and are magnified in (**D',E'**) to examplify counting mode (cells indicated by asterisks). Note that in the *lrp5* morphant BrdU+ cells are reduced in number. (**F**) Quantification of BrdU+ cell numbers in one unilateral neuroepithelium of rhombomeres 4-6. n=9/11 (wild-type/*lrp5* morphant). **P*=1.05x10^{-6}, *t*-test. (**G-J**) 20 ss embryos stained for *ccnd1* transcripts. (G,H) Wild-type embryo, (I,J) *lrp5* morphant. Note that *ccnd1* is enhanced in *lrp5* morphants. Frames in G,H indicate magnified area in flatmount H,J. Anterior is to the left in all pictures.

arrest in hindbrain cells of *lrp5* morphants as evident by accumulation of *ccnd1*. Consequently, this would lead to the reduction of S-phase cells, which is exactly what was seen in the *lrp5* morphants (Fig. 19E).

3.2.9. Absence of postmigratory CNCCs due to *lrp5* knock-down results in cranial skeleton malformation

The head skeleton emerges from derivatives of the cranial neural crest. It was expected that the observed failure of CNCC proliferation and migration (see 2.4 and Fig. 3) would result in reduced numbers of postmigratory cells in the pouches of the pharyngeal arches. To test this hypothesis, I examined *lrp5* morphants in the *fli1*:EGFP transgenic background (Lawson and Weinstein et al., 2002). This transgenic line shows reporter expression under control of the *friend leukemia inhibitor1*-promoter, expressed in vascular endothelial cells as well as in CNCC derivatives. Thus, at around 30 hpf the mandibular (md), the hyoid (hy) and the three branchial (br) patches of postmigratory CNCCs can be identified in the lateral head region of wild-type embryos (Fig. 20A,A'). In contrast, in 65% of *lrp5*Mo injected embryos (n=32), these structures were absent or strongly reduced (Fig. 20B,B'). I followed the affected embryos during further development and analyzed morphogenesis and positions of GFP positive CNCC derivatives. At 48 hpf, the pharyngeal arches in the uninjected control were well established as visible by the five clearly distinguishable columns of GFP positive cells (Fig. 20C,C') oriented bilaterally in the caudal head region (Fig. 20E,E'). In contrast, the *lrp5* morphants failed to establish proper pharyngeal arch morphology. Only a group of disorganized GFP+ cells at the posterior end could possibly be identified as 5th branchial arch (ba5?; Fig. 20D,D',F,F'). By 72 hpf, the morphogenetic processes have directed the gross of neural crest derivatives to their morphogenetic destinations so that the GFP-positive cells resemble the main architecture of the mature ventral cranial skeleton and structures like Meckel's cartilage (mc), the ceratohyal (ch) and the five ceratobranchials (cb) are

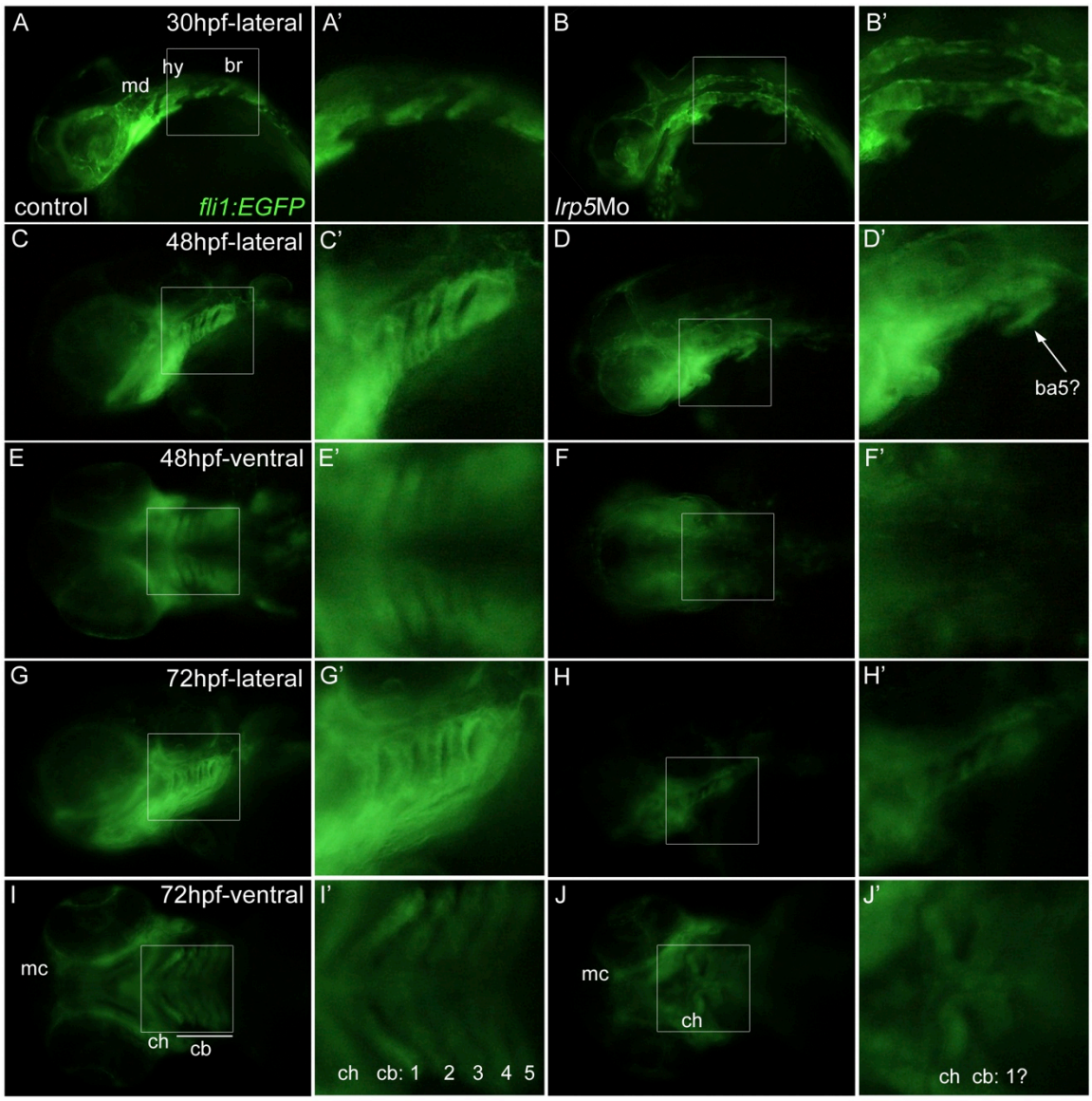

Fig. 20. Absence of postmigratory CNCCs due to *lrp5* knock-down results in cranial skeleton malformation. (**A-B'**) *fli1*:EGFP transgenic embryos at 30 hpf. (A,A') Uninjected control embryo, (B,B') *lrp5* morphant. Note that the mandibular (md), hyoid (hy) and three branchial (br) patches of postmigratory CNCCs are well defined in wild-type but missing in *lrp5* morphants. (**C-F'**) *fli1*:EGFP transgenic ambryos at 48 hpf. (C,C') Uninjected control embryo lateral view, (D,D') *lrp5* morphant lateral view, (E,E') uninjected control embryo dorsal view (F,F') *lrp5* morphant dorsal view. Note that metameric morphology of pharyngeal arches is absent in *lrp5* morphant. Only the 5th branchial arch seems to be present (ba5?). (**G-J'**) *fli1*:EGFP transgenic ambryos at 72 hpf. (G,G') Uninjected control embryo lateral view, (H,H') *lrp5* morphant lateral view, (I,I') uninjected control embryo dorsal view (J,J') *lrp5* morphant dorsal view. Note that in wild-type skeletal elements like Meckel's Cartilage (mc), ceratohyal (ch) and 1st till 5th ceratobranchials (cb 1-5) can be distinguished at this stage, whereas in *lrp5* morphant only the mc and ch are recognized while the cbs are undefined. Anterior is to the left in all images. Boxed areas in X are magnified in X'.

distinguishable (Fig. 20G,G',I,I'; compare to Fig. 1H). In the *lrp5* morphants, however, the absence of pharyngeal arches leads to severe malformation in the morphology of the cranial skeleton. Some rudiments of the caudal pharyngeal arches are visible in the lateral view (Fig. 20H,H'). While most parts of the anterior skeleton such as Meckel's cartilage (mc) are visible in the ventral view (Fig. 20J,J') only rudiments of the ceratohyal can be identified (ch) and the morphology of the ceratobranchials (cb) is hardly established. Taken together these data illustrate how the morphogenetic process from postmigratory NCCs to distinct structures of the cranial skeleton takes place in the course of development and how initial absence of postmigratory CNCCs in *lrp5* morphants leads to the morphological defects that are detectable by cartilage staining, eventually.

3.2.10. Knock-down of *sost* phenocopies knock-down of *lrp5*

Zebrafish *sost*, encoding a putative inhibitor of Lrp5 in Wnt signaling, is expressed at the critical stages of CNCC migration (around 20 ss) in the posterior hindbrain neuroepithelium (see Fig. 11) and in neural crest derivatives at later stages of development (Fig. 12 and Fig. 13). For a targeted gene knock-down approach to inhibit functional Sost, I designed a set of splice site Mos. Several concentrations of combined Mos targeting the splice donor (*sost*MoUp) and splice acceptor (*sost*MoDown) sites of the only intron in the *sost* gene were tested for efficiency. All experiments resulted in distinct phenotypes in a concentration dependent manner (Fig. 21; Fig. 22B; Table 3). The best results in terms of ratios of specifically affected embryos in morphant batches were seen by combined injection of 0.15mM *sost*MoUp and *sost*MoDown. This concentration was used for all experiments and is henceforth addressed as *sost*Mo. A mismatch Mo with five random nucleotide replacements was used as additional control and did not result in any defects (*sost*MoUpMM; see Fig. 21, column 5; Table 3). *sost*Mo injection specifically prevented correct splicing of *sost* pre-mRNA as evident by reduced amounts of PCR product using an intron

spanning primer pair on cDNA of injected embryos compared to wild-type (compare lane 4 to lane 3 in Fig. 22A). β-catenin was used as a control to ensure same cDNA concentration in the compared entities (see lane 1 and 2 in Fig. 22A).

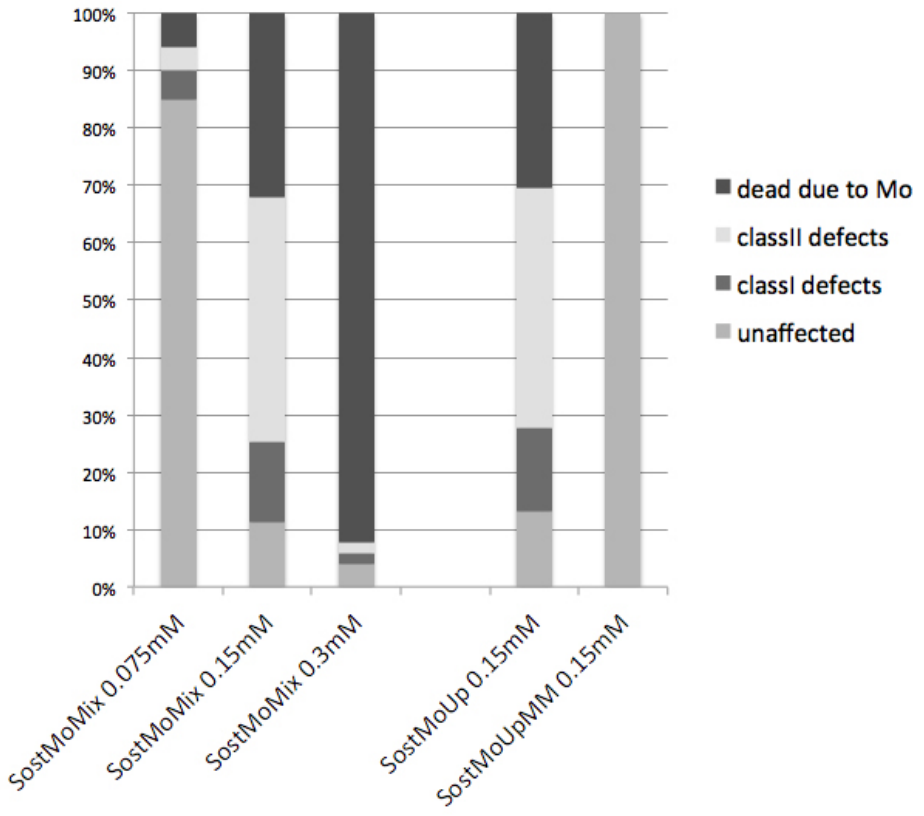

Fig. 21. Knock-down of *sost* is dependent on morpholino dose. Graphical interpretation of statistics of *sost*Mo injections. For definition of classI and classII defects see page 65 and Fig. 16H,I; Fig. 22B. For exact numbers see table 3 in appendix on page 95.

*sost*Mo injection resulted in severe malformations of the ventral cranial skeleton comparable to the situation after knock-down of *lrp5* (Fig. 16). Cartilage staining at 7 dpf revealed a complete absence of ceratobranchials in morphant larvae (Fig. 22B, arrowhead) and a reduced and reversed ceratohyal. Rudiments of the 5th ceratobranchials are visible (Fig. 22B, arrow).

Next, I wanted to check whether the observed craniofacial defects result from comparable defects as seen in the *lrp5* morphant situation. For this, I assessed the proliferative status of neuroepithelial cells in rhombomeres 4 to 6 in *sost* morphant embryos at 20 ss by immunohistochemical staining for pH3+ nuclei (Fig. 22C,D). In *sost* morphant embryos the number of positively stained nuclei was reduced by an average of 36% compared to wild-type controls ($P<10^{-6}$; n=11) in the respective area (Fig. 22E).

Accordingly, I analyzed gene expression patterns of the migratory CNCC marker *dlx2a* and the pan-neural crest marker *crestin*. The same defective distribution of CNCCs was found in *sost* morphants as earlier observed for *lrp5* morphants. In 20% of morphants (n=82), NCCs positive for *dlx2a* were found partially retained in the dorsal hindbrain and reduced in number especially in the caudal migratory streams of CNCCs compared to wild-type and mismatch controls (Fig. 22F-I; Fig. 24I,J; n=65). The same situation was observed by staining for *crestin* positive cells in 24% of the morphants (n=75; Fig. 22J-M). No alterations in the *crestin* expression pattern was found in *sost*MoUpMM morphants (n=47; Fig. 24K,L).

In line with these findings, *fli1*:EGFP positive postmigratory CNCCs were substantially reduced in number at around 30 hpf in 54% of *sost* morphant embryos (compare morphants in Fig. 22O with wild-type in N). Accordingly, at 3 dpf, when the CNCC derivatives demarcate the architecture of the ventral craniofacial skeleton in the wild-type (Fig. 22P) the number of *fli1*:EGFP positive cells in *sost* morphants was substantially reduced especially in the caudal part (Fig. 22Q).

Taken together, these data suggest that knock-down of *sost* results in morphological defects that are very similar to those obtained after knock-down of *lrp5*.

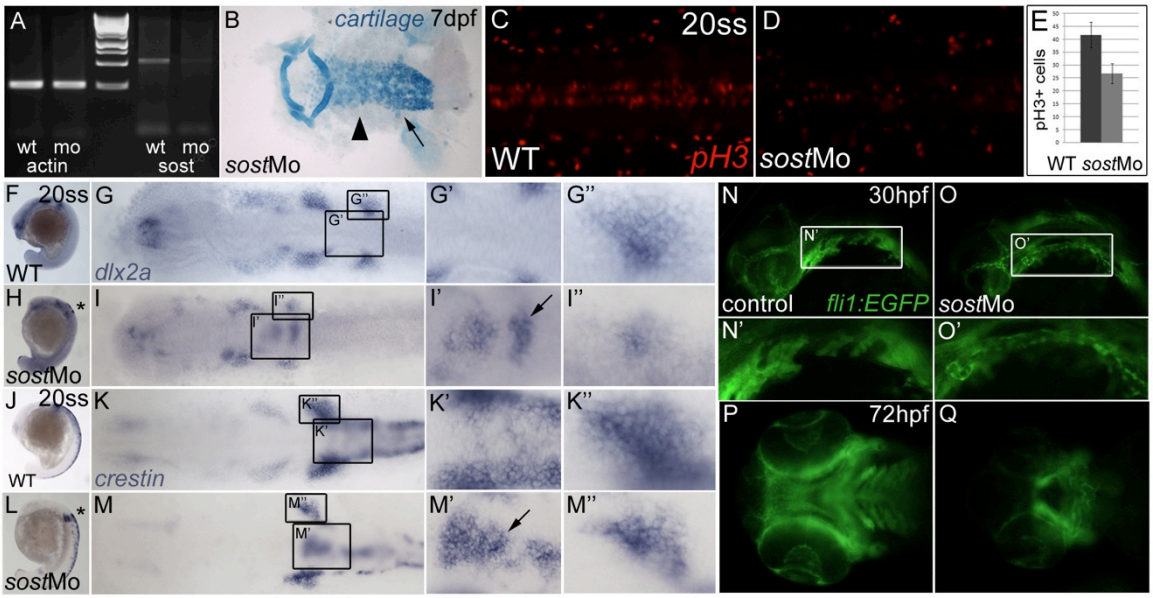

Fig. 22. Knock-down of *sost* phenocopies knock-down of *lrp5*. (**A**) RT-PCR with mRNA from wild-type (wt) and *sost* morphants (mo). (**B**) Cartilage staining of 7 dpf *sost* morphant larva. (**C,D**) 20 ss embryos stained for pH3+ mitotic cells. (C) Wild-type embryo, (D) *sost* morphant. Note that in the *sost* morphant pH3+ cells are reduced in number. (**E**) Quantification of pH3+ cell numbers in the neuroepithelium of rhombomeres 4-6. n=9/11 (wild-type/*lrp5* morphant). **P*<10^{-6}, *t*-test. (**F-I**) Embryos at 20 ss stained for *dlx2a* transcripts. (F,G) Wild-type embryo, (H,I) *sost* morphant. Note that ectopic *dlx2a* expression is present at the dorsal neuroepithelium of rhombomere 6 in *sost* morphants (asterisk in H; arrow in I') and the streams of branchial migratory CNCCs are reduced in cell number (I''). (**J-M**) Embryos at 20 ss stained for *crestin* transcripts. (J,K) wild-type embryo, (L,M) *sost* morphant. Note that ectopic *crestin* expression is present at the dorsal neuroepithelium of rhombomere 6 in *sost* morphants (asterisk in L; arrow in M') and the streams of branchial migratory CNCCs are reduced in cell number (T). (**N-Q**) *fli1*:EGFP embryos showing reporter expression in postmigratory CNCCs and their derivatives. (N) Uninjected control embryo at 30 hpf, (O) *sost* morphant at 30 hpf. Note that postmigratory CNCCs are missing in *sost* morphant. (P) Uninjected control at 72 hpf, (Q) *sost* morphant at 72 hpf. Note that ceratobranchials are absent in *sost* morphant. X' and X'' are magnifications of boxed areas in X. Anterior is to the left in all images.

4. DISCUSSION

4.1 Conditional cell ablation in medaka

To gain new insights into the role of osteoblasts in development of the vertebral column, I generated the *osx:CFP-NTR* transgenic line. This approch enabled conditional ablation of the osteoblast cell lineage which was evident by reduced reporter and marker gene expression as well as enhanced apoptosis in skeletal elements and resulted in reduced mineralization of cranial bone structures and vetrebral spines. In contrast, vertebral bodies were found fused, which suggests a new and additional function of osteoblasts in defining vertebral borders. Additionally, regenerative properties of osteoblasts could be seen by gradual reappearance of reporter expression after withdrawal of drug treatment.

This study shows for the first time the successful application of the NTR/Mtz cell ablation system in medaka. In the past, this system has been used to enable tissue specific cell ablation in mouse cell cultures (Bridgewater et al., 1995) with CB1954 as prodrug and also in zebrafish. In this model successful ablation of heart muscle cells, β-cells, liver cells, retinal cells, testicular cells and epidermal cells has been carried out (Pisharath et al., 2007; Curado et al., 2008, Zhao et al., 2009; Hsu et al., 2009; Chen et al., 2011). To efficiently ablate osteoblasts in our *osx:CFP-NTR* medaka model, where the NTR is expressed under control of the osteoblast specific *osx* promoter, I had to modify previously described protocols. In my experiments, only homozygous individuals showed efficient cell ablation, while heterozygous did not (data not shown) indicating the requirement of a critical threshold of NTR. In previous reports using transgenic zebrafish expressing tissue specific NTR, substantial cell ablation has been detected after 24 hours exposure to 10 mM Mtz (Pisharath et al., 2007; Curado et al., 2008). For an efficient ablation of osteoblasts in *osx:CFP-NTR* medaka, however, larvae needed to be exposed to 10 mM Mtz for at least 6 days. We hypothesize that it takes a higher dose of Mtz to reach the osteoblasts that are generally surrounded by dense extracellular matrix. In addition, also higher levels of NTR-metabolized Mtz

might be needed to exert any toxic effect on osteoblasts. Unfortunately, a detailed study testing the effect of Mtz on different cell types is lacking, but we assume that osteoblasts might be more resilient than e.g. liver cells as described before. After 6 dot, cell ablation was only observed in skeletal elements that showed CFP-NTR expression already at the start of treatment, namely the cleithrum and operculum. Here, cells metabolized Mtz throughout the entire incubation period, which eventually resulted in ablation. In contrast, CFP at 6 dot was also observed in elements which contain cells with a later onset of endogenous *osx* expression, i.e. the hyosymplectic, the quadrate or the branchiostegal rays (Renn and Winkler, 2009). In these bones, Mtz was only metabolized for shorter periods due to the later onset of *osx*-promoter driven CFP-NTR expression suggesting that accumulation of the cytotoxic drug might not have reached toxic levels in the analyzed time window.

The frequently observed death of *osx:CFP-NTR* and *osx:mCherry*/wild-type control larvae after long time Mtz exposure suggests that also non-processed Mtz has some unspecific toxic effects. In addition, survival rates of Mtz exposed *osx:CFP-NTR* larvae (25%) were lower than those of *osx:mCherry* (33%) and wild-type larvae (53%) suggesting off target toxicity also of Ntr metabolized Mtz during long time exposure. Consistently, increase of Mtz concentration to 20 mM resulted in even lower survival rates (data not shown). Increase of temperature to 37°C, on the other hand, did not enhance NTR/Mtz specific cell ablation, as expected from earlier reports (Emptage et al., 2009). The reasons for the different observations made in medaka and zebrafish studies are not clear but might be due to species and/or tissue-specific differences and/or different promoter efficiencies. All successful NTR approaches in zebrafish published so far report efficient cell ablation within 24 h of exposure, suggesting that the resilience might be due to species specific features, rather than a particular tissue.

Using Acridine Orange and TUNEL assays, we could show that the loss of osteoblasts is due to apoptosis. This is in line with previous reports on the mode of NTR/Mtz facilitated cell ablation

(Pisharath et al., 2007; Curado et al., 2008). However, due to the rather slow cell ablation process apoptosis was only detectable in areas of highest osteoblast density, such as the operculum and the pharyngeal teeth. Onset of *osc* expression occurs later than *osx* in the process of osteoblast maturation. *osc* is expressed in mature osteoblasts (Renn and Winkler, 2010) and secreted into the extracellular bone matrix (Hauschka et al., 1989). We could show that *osc* transcription is reduced in Mtr treated larvae confirming cell ablation of mature and ossifying osteoblasts.

The impact of osteoblast ablation on bone mineralization was assessed by live skeletal staining with ALC in Mtz treated *osx:CFP-NTR* larvae. The cleithrum and operculum as cranial bones showed reduction of mineralization suggesting a discontinued deposition of extracellular bone matrix after ablation of the majority of osteoblasts in these elements. The remaining mineralized structures are probably deposits made by osteoblasts before the Ntr/Mtz driven ablation occurred or from remaining osteoblasts not targeted by Mtz. In neural arches, osteoblast ablation also resulted in reduced mineralization. These arches were characterized by irregular shapes possibly due to mechanical effects exerted from tissue growing around the mineralized arches.

Surprisingly, a fusion of centra and excess mineralization was observed in 32% of individuals treated with Mtz for 12-16 days. We speculate that this fusion is caused by the ablation of osteoblasts positioned at the edges of the rostro-caudally extending chordal centra. This might result in the aberrant outgrowth and fusion of centra at the expense of intervertebral regions. Studies in zebrafish and Atlantic salmon have proposed a direct role for notochord cells in mineralizing the notochordal sheath, the innermost layer of the centra (Fleming et al., 2004; Grotmol et al., 2005). Hence, it remains to be tested whether notochord cells, upon ablation of osteoblasts at the edges of the extending centra, become activated to produce excess mineralized notochordal sheath. Alternatively, it has been reported that sclerotome derived osteoblasts are situated around the notochordal sheath and secrete minerals to form the perichordal centrum and extend this structure in rostrocaudal direction (Inohaya et al., 2007). Interestingly, Spoorendonk

and colleagues (2008) suggested the presence of *osx*-negative osteoblasts to be implicated in this process. This opens the possibility that *osx*-negative osteoblasts could be responsible for the centra fusion observed after ablation of *osx*-positive cells. Unfortunately, however, such *osx*-negative osteoblasts remain speculative and still await identification and characterization. Our lab has recently identified a novel marker that labels these proposed *osx*-negative osteoblasts (J. Renn, personal communication) therefore providing further support for my model. Importantly, how a metameric pattern is generated in the teleost vertebral column still remains unclear. We show that *osx*-positive cells first appear at the anterior and posterior edges of each centrum and that their ablation leads to fusion of the centra. Therefore, it is possible that the presence of these osteoblasts is necessary to prevent outgrowth of the centra into the intervertebral space. Hence, *osx*-positive cells could have a function in defining the borders of the forming centra thus contributing to the segmental pattern of the vertebral column.

We could show that the osteoblast lineage is capable of regenerating after Ntr/Mtz induced cell ablation. In all observed larvae, the CFP signal gradually reappeared in skeletal elements after previous cell ablation. Therefore, we assume that this lineage actively compensates for the severe loss of osteoblasts. However, further studies are required to clarify the underlying mechanisms and the origin of newly formed osteoblasts. The field of regeneration biology has recognized the potential of fish as model for heart (Poss, 2007), liver (Sadler et al., 2007) or appendage regeneration (Iovine, 2007; Knopf et al., 2011). In the future, studying osteoblast regeneration in medaka via *osx:CFP-NTR* can help to gain a better understanding of the processes involved in maintaining the equilibrium between osteoblasts and osteoclasts as well as osteoblast reactivation and growth. These mechanisms are vital for bone homeostasis and often disturbed in human bone diseases. Thus, this could eventually lead to new therapeutic strategies to counteract osteoporosis in human patients as well as enhance regeneration of bone mass in the process of fracture healing.

4.2. Overlapping expression of Lrp5 and its putative inhibitor Sost during cranial skeleton development in zebrafish

Next, I sought to study aspects of craniofacial skeleton morphogenesis, in particular its molecular control by Wnt signaling. Thereofore, I focused on Lrp5 in zebrafish. Knock-down of these factors seemed a better approach for modulation of Wnt signal transduction than targeting one or several of the 15 different Wnt ligands and 11 Fz receptors in zebrafish. Furthermore, I was interested in studying the role of Sost in zebrafish, which has been described as an inhibitory factor of Wnt signaling in more recent vertebrates and is suggested to exert its function through binding to Lrp5.

The tight spatiotemporal correlation of *lrp5* and *sost* expression suggests a possible functional interaction in zebrafish as has been described in mammalian bone metabolism. In contrast to the situation in mammals, however, restricted expression of both genes was found in distinct regions of the brain and ventral cranial skeleton during early and late stages of embryogenesis. In general, we find that in zebrafish *lrp5* is expressed in broader domains while its putative inhibitor *sost* is confined to more restricted domains overlapping with or directly adjacent to *lrp5* expression.

In mammals, a detailed embryonic expression of *lrp5* and *sost* has never been assessed. However, the distinct bone associated phenotypes in knock-out mice and human patients suggested a role of the two genes in osteoblasts, and an additional function of Lrp5 in eye vascularisation (Gong et al., 2001; Kato et al., 2002).

Head cartilage formation in zebrafish has been reported to be dependent on FGF signaling, however a link between Fgf and Wnt signaling in this process had so far not been established (Crump et al., 2004; Hall et al., 2006; Walshe and Mason, 2003). The results from my SU5402 mediated Fgf inhibition experiments clearly suggest that *sost* expression is controlled by Fgf signaling. I observed that down-regulation of *sost* was limited to the ventral expression domain in the developing embryo around 20 ss. Interestingly, we noticed that expression of *pea3*, which

encodes an ETS-domain transcription factor mediator of Fgf signaling (Besser et al., 1995), overlaps with this ventral *sost* expression in 20ss embryos (Munchberg et al., 1999) but not with the emerging hindbrain expression which remains unaffected. This suggests that Fgf control over *sost* transcriptional activity could be mediated through Pea3.

Crosstalk between Fgf and Wnt signaling is important throughout many aspects of embryonic development (reviewed by Dailey et al., 2005). To explain the underlying mechanisms how both pathways are integrated, previous models have been focusing on the intracellular components of the two pathways. Our observation of Fgf control of *sost* transcription therefore adds a novel aspect to this cross-talk as it involves an extracellular factor in the interaction between Fgf and Wnt signaling.

Mammalian cell culture experiments have shown that *Sost* expression is positively regulated by bone morphogenetic proteins (BMPs), retinoic acid and vitamin D or abolished by dexamethasone (Winkler et al., 2003; Ohyama et al., 2004; Sutherland et al., 2004). Moreover, *Sost* expression is directly suppressed by parathyroid hormone (PTH), both *in vitro* and *in vivo*, via PTH receptor type 1 (PTH1R; Keller and Kneissel, 2005). Two master regulators of osteoblast differentiation, Runx2 and Osterix, have been analyzed for their role in regulating *sost* expression. Sost appears to be a component of the Runx2 autoregulatory circuit (Sevetson et al., 2004). Suppression of Osterix mRNA by small interfering RNA (siRNA) resulted in down-regulation of SOST mRNA expression in primary osteoblast cells suggesting a positive role for Osterix in SOST regulation (Ohyama et al., 2004). With our data obtained *in vivo* in zebrafish, we present FGF signaling as a possible novel upstream regulator of *sost* expression.

4.3. A role for Lrp5 and Sost in morphogenesis of the craniofacial skeleton in zebrafish

The results presented in this thesis suggest a novel role for Lrp5 and Sost in early patterning events during vertebrate embryogenesis.

In zebrafish with knock-down of Lrp5 as well as Sost I observed the strongest defects during craniofacial development occurring in ceratobranchials 1-4, while the 5th ceratobranchial and the pharyngeal teeth appear unaffected at least in classI morphants. This was also evident by the pattern of *sox10*:GFP positive cells in 7 dpf larvae (not shown). Only few GFP+ cells are present in the 5th ceratobranchials demonstrating that this structure is mostly of non-CNCC origin. This explains why this element is not affected by loss of Lrp5 function. The pharyngeal teeth are a product of the pharyngeal epithelium posterior of ceratobranchials 5 (Huysseune et al., 1998) and no *sox10*:GFP+ cells can be found in this region. Consequently, the dentition in *lrp5* morphants looks normal: teeth are in the correct position, they display proper alignment relative to each other, and appear in the exact order, as judged from their developmental stage. The dentition appears to be slightly delayed with respect to wild-type, and corresponds to the dentition of specimens aged between 56 and 72 hpf. Taken together, the absence of ceratobranchials 1-4 with the 5th one and dentition being unaffected shows that the effect of the morphant phenotype is limited to CNCC derivatives in the ventral cranial skeleton.

We were able to show that the observed skeletal defects result from events that take place earlier in development. Wnt signaling is known to be involved in different steps of NCC development, including induction as it has also been shown in zebrafish (Lewis et al., 2004). However, although *lrp5* is expressed in the areas of NCC induction at the corresponding stages, it seems not to be involved in the process, as the number and pattern of premigratory CNCCs was not affected in the morphant situation. This is particularly interesting, since in Xenopus miss-expression of a truncated dominant-negative variant of Lrp6 leads to reduced NCC induction (Tamai *et al*., 2000). Importantly, *sost* is not yet expressed at the developmental stage of NCC induction. In both morphants, however, I observed aberrant localization of migratory CNCCs in embryos at advanced stages. Around 20 ss, when CNCCs have already evaded from the neuroepithelium in wild-type embryos, cells of the branchial stream were found left behind in the dorsal part of

rhombomere 6 (see model in Fig. 23A). These cells were unambiguously identified as NCCs as they were positive for the marker genes *crestin*, *sox10* and *dlx2a*. Interestingly, *dlx2a* is only expressed in migratory CNCCs. This finding suggests that these cells in the morphants had already undergone EMT but failed to pursue migration towards the pouches of the pharyngeal arches. Canonical Wnt signaling has been shown to be indispensable for NCC migration *in vitro* (de Melker et al., 2004). In zebrafish, it has been shown that Wnt signaling is linked to N-cadherin by Ovo1 and thereby regulates NCC migration (Piloto and Schilling, 2010). Wnts are also activators of *snail,* which is a repressor of E-cadherin (Vallin et al., 2001). Thus, the observation that CNCC migration is disturbed in *lrp5*/*sost* morphant zebrafish embryos adds an additional aspect to the understanding how cell migration in the cranial neural crest is regulated by Wnts.

As it has been shown in chick embryos, delamination of NCCs is tightly intertwined with their cell cycle and synchronized in S-phase. Moreover, this process has been shown to be mediated by Wnt signals (Burstyn-Cohen et al., 2004). In *lrp5* and *sost* morphants, the cell cycle of premigratory CNCCs appears arrested, as I found reduced numbers of nuclei in M-phase and S-phase in the relevant rhombomeres, where CNCCs originate. This suggests involvement of Lrp5/Sost also in cell cycle control of premigratory CNCCs. Such a role for Wnt signaling had been suggested earlier by Berndt and Halloran (2006). They showed comparable phenotypes by employing heatshock driven expression of dominant-negative TCF to inhibit Wnt signal transduction. In this study, they also reported reduced numbers of S-phase nuclei in premigratory CNCCs. However, which Wnt components were responsible for this defect remained unknown.

Wnt signals regulate the cell cycle directly through transcriptional control over *ccnd1* and thereby control G1/S-phase transition (Tetsu and McCormick, 1999). This mechanism has been shown to also apply to the zebrafish neural crest (Berndt and Halloran, 2006). However, I found that in the *lrp5* morphants, the transcriptional level of *ccnd1* was substantially increased. One possible

explanation for this surprising finding could be that Lrp5 mediated Wnt signaling might exert additional effects on the cell cycle that are dysfunctional in the knock-down situation. Thus, elevated levels of *ccnd1* transcripts in parallel with reduced BrdU incorporation could be interpreted as a sign of blocked G1/S-phase transition. Possibly, these arrested cells could keep feeding back on the *ccnd1* promoter so that transcripts accumulate due to lack of checkpoint signals. Interestingly and supporting this idea, a comparable situation has been described in serum deprived mouse osteoblast cell cultures, in which RNAi mediated downregulation of LEF1 also resulted in the upregulation of Cyclin D1 (Galindo et al., 2007).

Noteworthy, migrational defects such as observed in my experiments are not necessarily a direct consequence of reduced proliferation of premigratory CNCCs and impaired S-phase synchronization. Knock-down of Semaphorin3D in zebrafish was shown to result in reduced proliferation of premigratory CNCCs (Berndt and Halloran, 2006). As a consequence migratory CNCCs were found reduced in number yet importantly did not show loss of migratory behavior. This suggests that migratory properties of CNCCs are not directly linked to preceding proliferation and delamination, and that the migration defects observed in my experiments can also be explained by an additional migratory function of Lrp5.

Taken together, Lrp5/Sost mediated Wnt signaling might be essential for multiple steps in this process, i.e. proliferation of premigratory CNCCs and therefore S-phase synchronized EMT as well as subsequent migration of delaminated CNCCs (Fig. 23B). This model is in line with the fact that Wnt signaling has been shown to play multiple roles in the different phases of NCC development (Lewis et al., 2004). Furthermore, the finding that Lrp5 and Sost are involved in proliferation but not in specification of CNCCs is comparable to the reported function of mouse Lrp5, which is responsible for proliferation of osteoblasts but not for their differentiation (Kato et al. 2002). Similar but yet unknown intracellular mechanisms could possibly be involved.

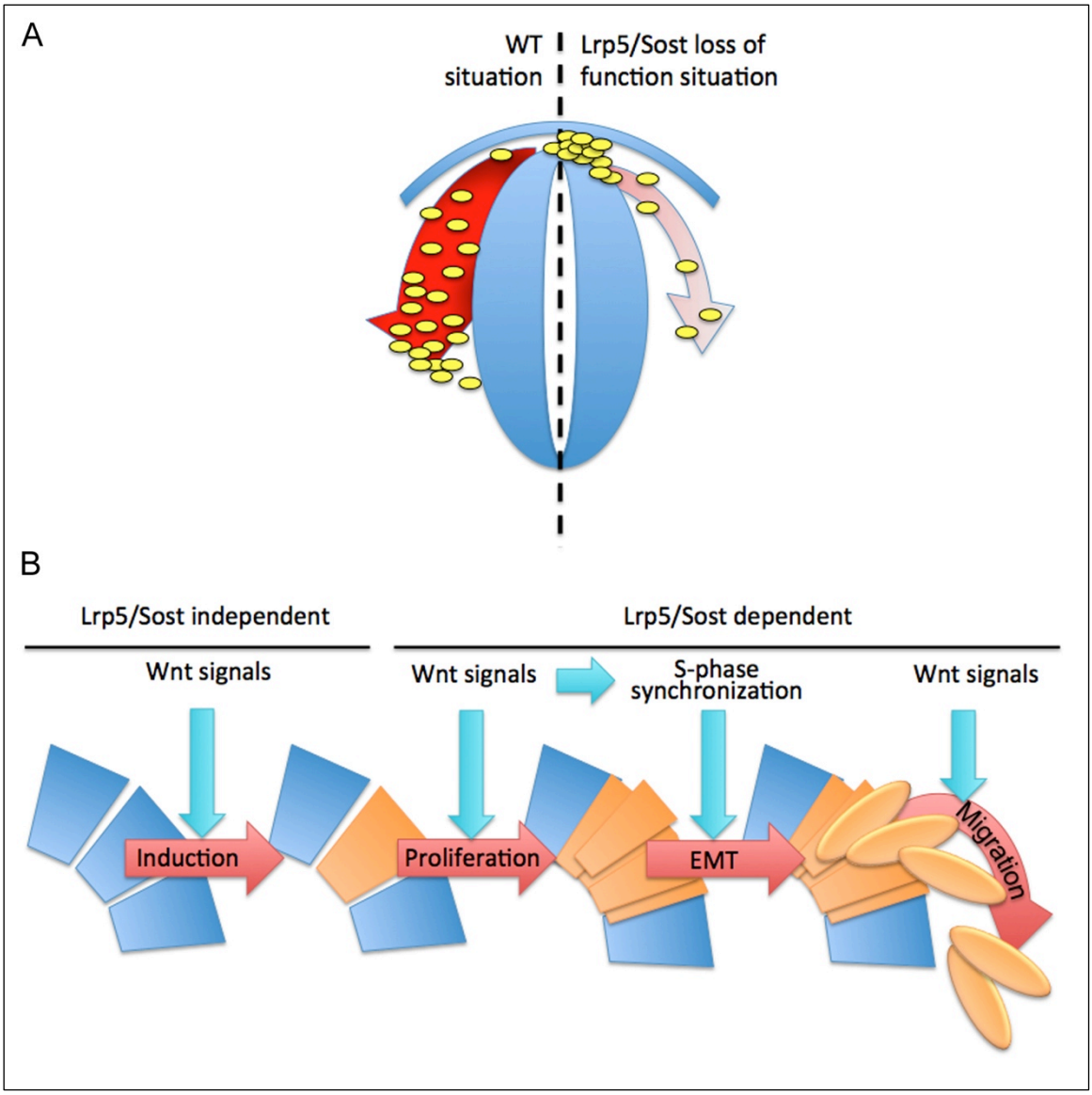

Fig. 23. Schematic interpretation of proposed model. (**A**) Comparison between wild-type (WT) and Lrp5/Sost loss-of-function situation. Whereas in wild-type cells migrate, in *lrp5/sost* morphants they are trapped dorsally. (**B**) Wnt signaling is known to be involved in all steps of NCC development. Nevertheless, induction of NCCs (orange cells) seems to work independent of Lrp5/Sost. Proliferation and migration seems directly dependent of Lrp5/Sost mediated Wnt signaling, and EMT could indirectly depend on Lrp5/Sost mediated cell cycle control.

Sost is known to be an inhibitory factor of canonical Wnt signaling. Its loss-of-function should therefore result in reduced inhibition of Wnt signal transduction in contrast to down-regulation by loss of Lrp5 function. Most surprisingly, the phenotypes obtained after *sost* knock-down showed appealing similarities with the described *lrp5* morphant phenotypes. I therefore suggest that Sost

exerts its function through binding to Lrp5 in zebrafish similar to what has been described in mouse (Ellies et al., 2006; Li et al., 2005; Semenov et al., 2005). Additionally, we suggest that zebrafish Sost is involved in the same developmental processes as Lrp5. The observed defects in the same cellular aspects of CNCC development suggest that Lrp5/Sost interaction might enable some kind of fine-tuning of canonical Wnt signal transduction to tightly control the level of activation of downstream targets implicated in cell cycle progression and migratory behavior of CNCCs. An alteration of this balanced activity in any direction might lead to similar defects as observed in the *lrp5* and *sost* morphants.

The morphogenetic fates of individual streams of migratory CNCCs have been described earlier (reviewed by Kimmel et al., 2001). I employed the *fli1*:EGFP transgenic line to follow the fate of postmigratory cells to their morphogenetic destinations in the craniofacial skeleton and to compare this process in the morphant situation. In contrast to the *sox10*:GFP line, where GFP expression is limited to NCCs, the *fli1* line shows EGFP reporter expression not only in NCCs but in the entire pharyngeal arches. Thus, this line gives more information about the overall morphology of these developing structures. I could confirm the previous findings and also show how the lack of branchial CNCCs results in failure of ceratobranchial morphogenesis. Also, morphogenesis of the 5th ceratobranchials could be followed and seemed less affected than the other four in the *lrp5* morphant situation. This confirmed the observations made by skeletal staining at 7dpf.

lrp5 and *sost* are expressed in and around derivatives of CNCCs throughout development, which suggests additional functions throughout morphogenesis. However, since the described defects occured already at relatively early stages we can only speculate about extended functions in the progressing craniofacial morphogenesis as well as later bone homeostasis.

4.4. A teleost specific function for Lrp5 in craniofacial development?

Previously, the functions described for Lrp5 and Sost were limited to bone metabolism (Gong et al., 2001; Balemans et al., 2001) with an additional role for Lrp5 in eye vascularization. Loss-of-function mutations in Lrp5 manifested as osteoporosis pseudoglioma (OPPG) syndrome. The same defects were also found in Lrp5 loss-of-function mutant mice (Kato et al., 2002). Interestingly however, no craniofacial deficiencies or any other forms of neural crest related abnormalities have been reported. However, observations in human patients suffering from genetically inherited LRP5 gain-of-function mutations reported mild aberrations in the skull anatomy. From early age onwards, some of these patients are characterized by abnormally thickened jaws or lobulated palates (Boyden et al., 2002). Young patients with a specific gain-of-function mutation (A214T) also suffered from craniosynostosis (Kwee et al. 2005). The early onset of these deformations suggests that they are not a result of a progressive sclerosteosis as described in all other Lrp5 gain-of-function mutants. Furthermore, it is well established that the jaw, palate and skull are derivatives of the human neural crest. Thus, one could speculate that the observations made in the human patients are a result of neural crest aberrations that occurred during embryonic development. An additional defect in humans carrying LRP5 loss-of-function mutations was shown in the eye vasculature. It was reported in mice that during embryonic development the transient hyaloid blood vessels fail to undergo macrophage induced apoptosis (Kato et al., 2002). Interestingly, it could be shown through fate mapping studies that also the hyaloid blood vessels partially originate from CNCCs (Gage et al., 2005). Thus, it could be possible that the eye vasculature defect observed in humans and mice is a result of losing a putative early Lrp5 function in CNCC developmental in mammals. In the zebrafish *lrp5* knock-down situation, I observed reduced eye size. However, this organ has not been in the focus of my experiments and could be subject to additional experiments in the future.

The manifestation of Sost loss-of-function mutations, on the other hand, was described as so

called van Buchem disease (Balemans et al., 2002) and sclerosteosis (Balemans et al., 2001), both characterized by progressively sclerosing limbs and skull. Although developmental defects are evident as syndactyly in sclerosteosis patients they cannot be directly linked to impaired CNCC development.

4.5. An evolutionary comparison of Lrp5 function

Notably, our observations indicate a more important role for Lrp5 during craniofacial morphogenesis in zebrafish than compared to the situation in mammals. Loss-of-function in fish leads to more severe craniofacial defects compared to the defects described for human gain-of-function mutations. I therefore speculate that in non-mammalian vertebrate species Lrp5 might play a more crucial role in this process compared to mammals. My experiments also indicate that the most affected structures in the craniofacial skeleton are the ceratobranchials that build up the gills. These structures derive from the branchial streams of CNCCs that have shifted their morphogenetic destination in the course of vertebrate evolution. In amphibians, they generate cells that eventually build up the bones of the skull proper (Olsson & Hanken 1996). However, in human embryonic development branchial NCCs play a minor role as they build up craniofacial elements such as the squamosal, alisphenoid or the hyoid bone (reviewed by Santagati and Rijli, 2003). None of these elements have been shown to be affected in Lrp5 gain of function mutants.

Nonetheless, it is tempting to speculate that the evolutionary shift of branchial migratory NCC morphogenetic destinations came together with a restructuring of Lrp5 function from a role in overall craniofacial development to a merely rudimental role.

Due to experimental limitations of our Mo mediated knock-down approach we could not make any conclusion about a possible role of zebrafish Lrp5/Sost in juvenile or adult bone mass regulation. Since Mos only exert their function during embryonic and early larval development in addition to the early death of morphant larvae due to lack of gills, other experimental strategies, such as mutant analysis or zinc finger nuclease approaches, will have to be employed to address

these questions.

Knock-down of *lrp5*/*sost* in zebrafish does not only affect the craniofacial skeleton. The hindbrain also seems to be strongly affected as its ventricle appears widely inflated. This is in line with the *lrp5*/*sost* expression pattern. We therefore suspect that Lrp5 and Sot might also have additional roles in neurogenesis, which was not subject of experiments in the presented study and will have to be assessed in the future.

Appendix

Table 2. Statistics of *lrp5*Mo injections. For definition of classI and classII defects see page 65 and Fig. 16H,I.

	total		unaffected		classI defects		classII defects		dead due to Mo		number of
	n	ratio	n	ratio	n	ratio	n	ratio	n	ratio	experiments
*lrp5*MoMix 0.3mM	261	100	118	45.2%	82	31.4%	27	10.3%	34	13.0%	4
*lrp5*MoMix 0.6mM	286	100	38	13.3%	84	29.4%	47	16.4%	117	40.9%	5
*lrp5*MoMix 0.3mM+*p53*Mo 0.6mM	80	100	3	3.8%	22	27.5%	27	33.8%	28	35.0%	2
*lrp5*MoUp 0.3mM	266	100	155	58.3%	26	9.8%	20	7.5%	65	24.4%	4
*lrp5*MoUp 0.6mM	91	100	5	5.5%	8	8.8%	55	60.4%	23	25.3%	2
*lrp5*MoUpMM 0.3mM	104	100	104	100.0%	0	0.0%	0	0.0%	0	0.0%	2
*lrp5*MoDown 0.3mM	134	100	58	43.3%	36	26.9%	27	20.1%	13	9.7%	3
*lrp5*MoDown 0.6mM	82	100	3	3.7%	32	39.0%	23	28.0%	24	29.3%	1

Table 3. Statistics of *sost*Mo injections. For definition of classI and classII defects see page 65 and Fig. 16H,I; Fig. 22B.

	total		unaffected		classI defects		classII defects		dead due to Mo		number of
	n	ratio	n	ratio	n	ratio	n	ratio	n	ratio	experiments
*sost*MoMix 0.075mM	120	100%	102	85.0%	6	5.0%	5	4.2%	7	5.8%	2
*sost*MoMix 0.15mM	115	100%	13	11.3%	16	13.9%	49	42.6%	37	32.2%	2
*sost*MoMix 0.3mM	52	100%	2	3.8%	1	1.9%	1	1.9%	48	92.3%	1
*sost*MoUp 0.15mM	115	100%	15	13.0%	17	14.8%	48	41.7%	35	30.4%	2
*sost*MoUpMM 0.15mM	135	100%	135	100.0%	0	0.0%	0	0.0%	0	0.0%	2

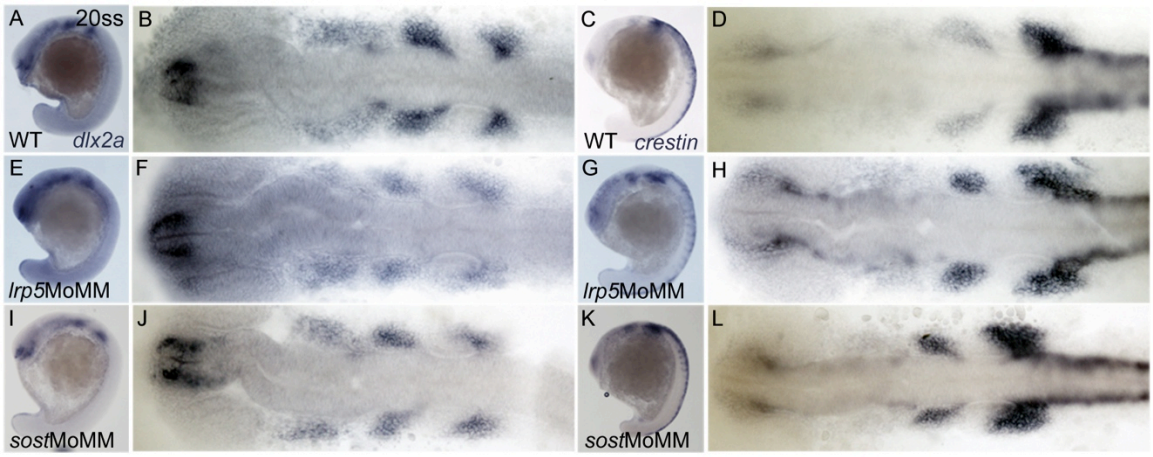

Fig. 24. Mismatch morphant control experiments. **(A,B)** Wild-type embryo stained for *dlx2a*. **(C,D)** Wild-type embryo stained for *crestin*. **(E,F)** *lrp5* mismatch morphant stained for *dlx2a*. **(G,H)** *lrp5* mismatch morphant embryo stained for *crestin*. **(I,J)** *sost* mismatch morphant stained for *dlx2a*. **(K,L)** *sost* mismatch morphant embryo stained for *crestin*. Note that mismatch Mo injection does not result in alterations of *dlx2a/crestin* expression patterns. Anterior is to the left in all images.

Bibliography

Aberle, H., Bauer, A., Stappert, J., Kispert, A. and Kemler, R., 1997. b-Catenin is a target for the ubiquitin-proteasome pathway. EMBO J 16, 3797–3804.

Ai, M., Holmen, S.L., Van Hul, W., Williams, B.O., Warman, M.L., 2005. Reduced affinity to and inhibition by DKK1 form a common mechanism by which high bone mass-associated missense mutations in LRP5 affect canonical Wnt signaling. Mol Cell Biol 25, 4946-4955.

Akimenko, M.A., Ekker, M., Wegner, J., Lin, W., Westerfield, M., 1994. Combinatorial expression of three zebrafish genes related to distal-less: part of a homeobox gene code for the head. J Neurosci 14, 3475-3486.

Altschul, S.F., Madden, T.L., Schaffer, A.A., Zhang, J., Zhang, Z., Miller, W., Lipman, D.J., 1997. Gapped BLAST and PSI-BLAST: a new generation of protein database search programs. Nucleic Acids Res 25, 3389-3402.

Balemans, W., Ebeling, M., Patel, N., Van Hul, E., Olson, P., Dioszegi, M., Lacza, C., Wuyts, W., Van Den Ende, J., Willems, P., Paes-Alves, A.F., Hill, S., Bueno, M., Ramos, F.J., Tacconi, P., Dikkers, F.G., Stratakis, C., Lindpaintner, K., Vickery, B., Foernzler, D., Van Hul, W., 2001. Increased bone density in sclerosteosis is due to the deficiency of a novel secreted protein (SOST). Hum Mol Genet 10, 537-543.

Balemans, W., Patel, N., Ebeling, M., van Hul, E., Wuyts, W., Lacza, C., Dioszegi, M., Dikkers, F.G., Hildering, P., Willems, P.J., Verheij, J.B., Lindpaintner, K., Vickery, B., Foernzler, D., van Hul, W., 2002. Identification of a 52 kb deletion downstream of the SOST gene in patients with van Buchem disease. J Med Genet 39, 91–97.

Berndt, J.D., Halloran, M.C., 2006. Semaphorin 3d promotes cell proliferation and neural crest cell development downstream of TCF in the zebrafish hindbrain. Development 133, 3983-3992.

Besser, D., Presta, M., Nagamine, Y., 1995. Elucidation of a signaling pathway induced by FGF-2 leading to uPA gene expression in NIH 3T3 fibroblasts. Cell Growth Differ 6, 1009-1017.

Bird, N.C. and Mabee, P.M. (2003) Developmental morphology of the axial skeleton of the zebrafish, Danio rerio (Ostariophysi: Cyprinidae). Dev Dyn 228, 337-57.

Boyden, L.M., Mao, J., Belsky, J., Mitzner, L., Farhi, A., Mitnick, M.A., Wu, D., Insogna, K., Lifton, R.P., 2002. High bone density due to a mutation in LDL-receptor-related protein 5. N Engl J Med 346, 1513-1521.

Bridgewater, J. A., Springer, C. J., Knox, R. J., Minton, N. P., Michael, N. P., Collins, M. K., 1995. Expression of the bacterial nitroreductase enzyme in mammalian cells renders them selectively sensitive to killing by the prodrug CB1954. Eur J Cancer. 31A**,** 2362-70.

Bryant, C., Hubbard, L., McElroy, W. D., 1991. Cloning, nucleotide sequence, and expression of the nitroreductase gene from Enterobacter cloacae. J Biol Chem. 266**,** 4126-30.

Bronner-Fraser, M., 1994. Neural crest cell formation and migration in the developing embryo. FASEB J 8, 699–706.

Brunkow, M.E., Gardner, J.C., Van Ness, J., Paeper, B.W., Kovacevich, B.R., Proll, S., Skonier, J.E., Zhao, L., Sabo, P.J., Fu, Y., Alisch, R.S., Gillett, L., Colbert, T., Tacconi, P., Galas, D., Hamersma, H., Beighton, P., Mulligan, J., 2001. Bone dysplasia sclerosteosis results from loss of the SOST gene product, a novel cystine knot-containing protein. Am J Hum Genet 68, 577-589.

Burstyn-Cohen, T., Kalcheim, C., 2002. Association between the cell cycle and neural crest delamination through specific regulation of G1/S transition. Dev Cell 3, 383-395.

Burstyn-Cohen, T., Stanleigh, J., Sela-Donenfeld, D., Kalcheim, C., 2004. Canonical Wnt activity regulates trunk neural crest delamination linking BMP/noggin signaling with G1/S transition. Development 131, 5327-5339.

Cadigan, K. M. and Nusse, R., 1997. Wnt signaling: a common theme in animal development Genes & Dev 11, 3286-3305

Chan, T., Kondow, A., Hosoya, A., Hitachi, K., Yukita, A., Okabayashi, K., Nakamura, H.,

Ozawa, H., Kiyonari, H., Michiue, T., Ito, Y., Asashima, M., 2007. Ripply2 is essential for precise somite formation during mouse early development. FEBS Lett. 581**,** 2691-6.

Chen, C. F., Chu, C. Y., Chen, T. H., Lee, S. J., Shen, C. N., Hsiao, C. D., 2011. Establishment of a Transgenic Zebrafish Line for Superficial Skin Ablation and Functional Validation of Apoptosis Modulators In Vivo. PLoS ONE 6, e20654.

Chenna, R., Sugawara, H., Koike, T., Lopez, R., Gibson, T.J., Higgins, D.G., Thompson, J.D., 2003. Multiple sequence alignment with the Clustal series of programs. Nucleic Acids Res 31, 3497-3500.

Christ, B., Huang, R., Scaal, M., 2004. Formation and differentiation of the avian sclerotome. Anat Embryol (Berl). 208**,** 333-50.

Cohn, M.J. and Tickle, C., 1996. Limbs: a model for pattern formation within the vertebrate body plan. Trends Genet 12, 253–57.

Cui, Y., Niziolek, P.J., Macdonald, B.T., Zylstra, C.R., Alenina, N., Robinson, D.R., Zhong, Z., Matthes, S., Jacobsen, C.M., Conlon, R.A., Brommage, R., Liu, Q., Mseeh, F., Powell, D.R., Yang, Q.M., Zambrowicz, B., Gerrits, H., Gossen, J.A., He, X., Bader, M., Williams, B.O., Warman, M.L., Robling, A.G., Lrp5 functions in bone to regulate bone mass. Nat Med 17, 684-691.

Curado, S., Stainier, D. Y., Anderson, R. M., 2008. Nitroreductase-mediated cell/tissue ablation in zebrafish: a spatially and temporally controlled ablation method with applications in developmental and regeneration studies. Nat Protoc. 3**,** 948-54.

Dailey, L., Ambrosetti, D., Mansukhani, A., Basilico, C., 2005. Mechanisms underlying differential responses to FGF signaling. Cytokine Growth Factor Rev 16, 233-247.

de Melker, A.A., Desban, N., Duband, J.L., 2004. Cellular localization and signaling activity of beta-catenin in migrating neural crest cells. Dev Dyn 230, 708-726.

Dorsky, R.I., Sheldahl, L.C., Moon, R.T., 2002a. A transgenic Lef1/beta-catenin-dependent reporter is expressed in spatially restricted domains throughout zebrafish development. Developmental biology 241, 229-237.

Dorsky, R.I., Snyder, A., Cretekos, C.J., Grunwald, D.J., Geisler, R., Haffter, P., Moon, R.T., Raible, D.W., 1999. Maternal and embryonic expression of zebrafish lef1. Mech Dev 86, 147-150.

Dutton, J.R., Antonellis, A., Carney, T.J., Rodrigues, F.S., Pavan, W.J., Ward, A., Kelsh, R.N., 2008. An evolutionarily conserved intronic region controls the spatiotemporal expression of the transcription factor Sox10. BMC Dev Biol 8, 105.

Ekanayake, S. and Hall, B. K. (1987). The development of acellularity of the vertebral bone of the Japanese medaka, Oryzias latipes (Teleostei; Cyprinidontidae). J Morphol 193, 253- 261.

Ellies, D.L., Viviano, B., McCarthy, J., Rey, J.P., Itasaki, N., Saunders, S., Krumlauf, R., 2006. Bone density ligand, Sclerostin, directly interacts with LRP5 but not LRP5G171V to modulate Wnt activity. J Bone Miner Res 21, 1738-1749.

Emptage, C. D., Knox, R. J., Danson, M. J., Hough, D. W., 2009. Nitroreductase from Bacillus licheniformis: a stable enzyme for prodrug activation. Biochem Pharmacol. 77**,** 21-9.

Erlebacher, A., Filvaroff, E. H., Gitelman, S. E. and Derynck, R., 1995. Toward a molecular understanding of skeletal development. Cell 80, 371–78.

Fanto, M. and McNeill, H., 2004. Planar polarity from flies to vertebrates. J Cell Sci 117, 527-533 Fleming, A., Keynes, R., Tannahill, D., 2004. A central role for the notochord in vertebral patterning. Development. 131**,** 873-80.

Galindo, M., Kahler, R.A., Teplyuk, N.M., Stein, J.L., Lian, J.B., Stein, G.S., Westendorf, J.J., van Wijnen, A.J., 2007. Cell cycle related modulations in Runx2 protein levels are independent of lymphocyte enhancer-binding factor 1 (Lef1) in proliferating osteoblasts. J Mol Histol 38, 501-506.

Gage, P.J., Rhoades, W., Prucka, S.K., Hjalt, T., 2005. Fate Maps of Neural Crest and Mesoderm in the Mammalian Eye. Investigative Ophthalmology & Visual Science 46, 4200-4208.

Gong, Y., Slee, R.B., Fukai, N., Rawadi, G., Roman-Roman, S., Reginato, A.M., Wang, H., Cundy, T., Glorieux, F.H., Lev, D., Zacharin, M., Oexle, K., Marcelino, J., Suwairi, W., Heeger, S., Sabatakos, G., Apte, S., Adkins, W.N., Allgrove, J., Arslan-Kirchner, M., Batch, J.A., Beighton, P., Black, G.C., Boles, R.G., Boon, L.M., Borrone, C., Brunner, H.G., Carle, G.F., Dallapiccola, B., De Paepe, A., Floege, B., Halfhide, M.L., Hall, B., Hennekam, R.C., Hirose, T., Jans, A., Juppner, H., Kim, C.A., Keppler-Noreuil, K., Kohlschuetter, A., LaCombe, D., Lambert, M., Lemyre, E., Letteboer, T., Peltonen, L., Ramesar, R.S., Romanengo, M., Somer, H., Steichen-Gersdorf, E., Steinmann, B., Sullivan, B., Superti-Furga, A., Swoboda, W., van den Boogaard, M.J., Van Hul, W., Vikkula, M., Votruba, M., Zabel, B., Garcia, T., Baron, R., Olsen, B.R., Warman, M.L., 2001. LDL receptor-related protein 5 (LRP5) affects bone accrual and eye development. Cell 107, 513-523.

Grotmol, S., Nordvik, K., Kryvi, H., Totland, G. K., 2005. A segmental pattern of alkaline phosphatase activity within the notochord coincides with the initial formation of the vertebral bodies. J Anat. 206**,** 427-36.

Hanken, J., Gross, J.B., 2005. Evolution of cranial development and the role of neural crest: insights from amphibians. Journal of anatomy 207, 437-446.

Hauschka, P. V., Lian, J. B., Cole, D. E., Gundberg, C. M., 1989. Osteocalcin and matrix Gla protein: vitamin K-dependent proteins in bone. Physiol Rev. 69**,** 990-1047.

He, X., Semenov, M., Tamai, K. and Zeng, X., 2004. LDL receptor-related proteins 5 and 6 in Wnt/beta-catenin signaling: arrows point the way. Development 131, 1663-1677.

Hinck, L., Nelson, W. J. and Papkoff, J., 1994. Wnt-1 modulates cell-cell adhesion in mammalian cells by stabilizing bcateninbinding to the cell adhesion protein cadherin. J Cell Biol 124, 729–741.

Horton, W. A., Campbell, D., Machado, M. A. and Chou, J., 1989. Type II collagen screening in the human chondrodysplasias. Am J Med Genet 34(4), 579-83.

Houston, D.W., Wylie, C., 2002. Cloning and expression of Xenopus Lrp5 and Lrp6 genes. Mech Dev 117, 337-342.

Hsu, C. C., Hou, M. F., Hong, J. R., Wu, J. L., Her, G. M., 2010. Inducible Male Infertility by Targeted Cell Ablation in Zebrafish Testis. Mar Biotechnology 12, 466–478.

Huber, A. H., Nelson, W. J. and Weis, W. I., 1997. Three-dimensional structure of the armadillo repeat region of b-catenin. Cell 90, 871–882.

Huysseune, A., Sire, J.Y., 1998. Evolution of patterns and processes in teeth and tooth-related tissues in non-mammalian vertebrates. Eur J Oral Sci 106 Suppl 1, 437-481.

Inohaya, K., Takano, Y., Kudo, A., 2010. Production of Wnt4b by floor plate cells is essential for the segmental patterning of the vertebral column in medaka. Development. 137**,** 1807-13.

Inohaya, K., Takano, Y., Kudo, A., 2007. The teleost intervertebral region acts as a growth center of the centrum: in vivo visualization of osteoblasts and their progenitors in transgenic fish. Dev Dyn. 236**,** 3031-46.

Iovine, M. K., 2007. Conserved mechanisms regulate outgrowth in zebrafish fins. Nat Chem Biol. 3**,** 613-8.

Kanda, T., Yoshida, Y., Izu, Y., Nifuji, A., Ezura, Y., Nakashima, K., Noda, M., 2007. PlexinD1 deficiency induces defects in axial skeletal morphogenesis. J Cell Biochem. 101**,** 1329-37.

Kato, M., Patel, M.S., Levasseur, R., Lobov, I., Chang, B.H., Glass, D.A., 2nd, Hartmann, C., Li, L., Hwang, T.H., Brayton, C.F., Lang, R.A., Karsenty, G., Chan, L., 2002. Cbfa1-independent decrease in osteoblast proliferation, osteopenia, and persistent embryonic eye vascularization in mice deficient in Lrp5, a Wnt coreceptor. J Cell Biol 157, 303-314.

Keller, H., Kneissel, M., 2005. SOST is a target gene for PTH in bone. Bone. 37, 148-58.

Kelsh, R.N., Dutton, K., Medlin, J., Eisen, J.S., 2000. Expression of zebrafish fkd6 in neural crest-derived glia. Mech Dev 93, 161-164.

Kimmel, C.B., Ballard, W.W., Kimmel, S.R., Ullmann, B., Schilling, T.F., 1995. Stages of embryonic development of the zebrafish. Dev Dyn 203, 253-310.

Kimmel, C.B., Miller, C.T., Keynes, R.J., 2001. Neural crest patterning and the evolution of the jaw. J Anat 199, 105-120.

Kimmel, C.B., Miller, C.T., Moens, C.B., 2001. Specification and Morphogenesis of the Zebrafish Larval Head Skeleton. Dev Biol 233, 239–257.

Klingensmith, J., Nusse, R. and Perrimon, N., 1994. The Drosophila segment polarity gene dishevelled encodes a novel protein required for response to the wingless signal. Genes Dev. 8, 118-130.

Knopf, F., Hammond, C., Chekuru, A., Kurth, T., Hans, S., Weber, C. W., Mahatma, G., Fisher, S., Brand, M., Schulte-Merker, S., Weidinger, G., 2011. Bone Regenerates via Dedifferentiation of Osteoblasts in the Zebrafish Fin. Dev Cell. 20**,** 713-24.

Koay, M.A. and Brown, M.A., 2000. Genetic disorders of the LRP5-Wnt signalling pathway affecting the skeleton. Trends Mol Med 11, 129-137.

Kohn, A. D. and Moon, R. T., 2005. Wnt and calcium signaling: beta-Cateninin dependent pathways. Cell Calcium 38, 439-446.

Komori, T., Yagi, H., Nomura, S., Yamaguchi, A. and Sasaki, K., 1997. Targeted disruption of Cbfa1 results in a complete lack of bone formation owing to maturational arrest of osteoblasts. Cell 89, 755–64.

Korinek, V., Barker, N., Morin, P. J., vanWichen, D., deWeger, R., Kinzler, K. W., Vogelstein, B. and Clevers, H., 1997. Constitutive transcriptional activation by a b-catenin-Tcf complex in APC(–/–) colon carcinoma. Science 275, 1784–1787.

Krieger, M., Herz, J., 1994. Structures and functions of multiligand lipoprotein receptors: macrophage scavenger receptors and LDL receptor-related protein (LRP). Annu Rev Biochem 63, 601-37.

Kwee, M.L., Balemans, W., Cleiren, E., Gille, J.J., Van Der Blij, F., Sepers, J.M., Van Hul, W., 2005. An autosomal dominant high bone mass phenotype in association with craniosynostosis in an extended family is caused by an LRP5 missense mutation. J Bone Miner Res 20, 1254-1260.

Lawson, N.D., Weinstein, B.M., 2002. In vivo imaging of embryonic vascular development using transgenic zebrafish. Developmental biology 248, 307-318.

Langeland, J.A., Kimmel, C.B., 1997. Chapter 19, Fishes. In: Gilbert SF and Raunio AM (ed.), Embryology Constructing the Organism. SINAUER ASSOCIATES, Inc. Publishers, Sunderland, MA 01375 U.S.A., 383-408.

Langille, R. M. and Hall, B. K., 1987. Development of the head skeleton of the Japanese Medaka, Oryzias latipes (Teleostei). J Morphol 193, 135–158.

Levasseur, R., Lacombe, D. and de Vernejoul, M.C., 2005. LRP5 mutations in osteoporosis-pseudoglioma syndrome and high-bone-mass disorders. Joint Bone Spine 72, 207-214.

Lewis, J.L., Bonner, J., Modrell, M., Ragland, J.W., Moon, R.T., Dorsky, R.I., Raible, D.W., 2004. Reiterated Wnt signaling during zebrafish neural crest development. Development 131, 1299-1308.

Li, X., Zhang, Y., Kang, H., Liu, W., Liu, P., Zhang, J., Harris, S.E., Wu, D., 2005. Sclerostin binds to LRP5/6 and antagonizes canonical Wnt signaling. J Biol Chem 280, 19883-19887.

Li, X., Ominsky, M.S., Niu, Q.T., Sun, N., Daugherty, B., D'Agostin, D., Kurahara, C., Gao, Y., Cao, J., Gong, J., Asuncion, F., Barrero, M., Warmington, K., Dwyer, D., Stolina, M., Morony, S., Sarosi, I., Kostenuik, P.J., Lacey, D.L., Simonet, W.S., Ke, H.Z., Paszty, C., 2008. Targeted deletion of the sclerostin gene in mice results in increased bone formation and bone strength. J Bone Miner Res 23, 860-869.

Lister, J.A., Cooper, C., Nguyen, K., Modrell, M., Grant, K., Raible, D.W., 2006. Zebrafish Foxd3 is required for development of a subset of neural crest derivatives. Dev Biol 290, 92– 104.
Little, R.D., Recker, R.R., Johnson, M.L., 2002. High bone density due to a mutation in LDL-receptor-related protein 5. N Engl J Med 347, 943-944; author reply 943-944.

Liu, G., Bafico, A., Harris, V. K. and Aaronson, S. A., 2003. A novel mechanism for Wnt activation of canonical signaling through the LRP6 receptor. Mol Cell Biol 23, 5825-5835.

Logan, C. Y. and Nusse, R., 2004. The Wnt signaling pathway in development and disease. Annu Rev Cell Dev Biol 20, 781-810.

Lowry, W. E., Blanpain, C., Nowak, J. A., Guasch, G., Lewis, L. and Fuchs, E., 2005. Defining the impact of beta-catenin/Tcf transactivation on epithelial stem cells. Genes Dev. 19, 1596-1611.
Luo, R., An, M., Arduini, B.L., Henion, P.D., 2001. Specific pan-neural crest expression of zebrafish Crestin throughout embryonic development. Dev Dyn 220, 169-174.

MacDonald, B.T., Tamai, K., He, X., 2009. Wnt/beta-catenin signaling: components, mechanisms, and diseases. Dev Cell 17, 9-26.

Mao, J., Wang, J., Liu, B., Pan, W., Farr, G. H. 3rd, Flynn, C., Yuan, H., Takada, S., Kimelman, D., Li, L., Wu, D., 2001a. Low-density lipoprotein receptor-related protein-5 binds to Axin and regulates the canonical Wnt signaling pathway. Mol Cell 7(4), 801-9.

Mao, B., Wu, W., Li, Y., Hoppe, D., Stannek, P., Glinka, A., Niehrs, C. 2001b. LDL-receptor-related protein 6 is a receptor for Dickkopf proteins. Nature 411, 321-325.

McCrea, P.D., C.W. Turck, and B. Gumbiner., 1991. A homolog of the Drosophila protein armadillo (Plakoglobin) associates with E-cadherin. Science 254, 1359–1361.

Meulemans, D., Bronner-Fraser, M., 2004. Gene-regulatory interactions in neural crest evolution and development. Dev Cell 7, 291–299.

Mohammadi, M., McMahon, G., Sun, L., Tang, C., Hirth, P., Yeh, B.K., Hubbard, S.R., Schlessinger, J., 1997. Structures of the tyrosine kinase domain of fibroblast growth factor receptor in complex with inhibitors. Science 276, 955-960.

Molenaar, M., Van de Wetering, M., Oosterwegel, M., Petersonmaduro, J., Godsave, S., Korinek, V., Roose, J., Destree, O. and Clevers, H., 1996. XTcf-3 transcription factor mediates bcatenin-induced axis formation in Xenopus embryos. Cell 86, 391–399.

Morin, P. J., Sparks, A. B., Korinek, V., Barker, N., Clevers, H., Vogelstein, B. and Kinzler, K. W., 1997. Activation of b-catenin-Tcf signaling in colon cancer by mutations in b-catenin or APC. Science 275, 1787–1790.

Mullis, K., Faloona, F., Scharf, S., Saiki, R., Horn, G., Erlich, H., 1986. Specific enzymatic amplification of DNA in vitro: the polymerase chain reaction. Cold Spring Harb Symp Quant Biol. 51, 263-273.

Munchberg, S.R., Ober, E.A., Steinbeisser, H., 1999. Expression of the Ets transcription factors erm and pea3 in early zebrafish development. Mech Dev 88, 233-236.

Nakashima, K., Zhou, X., Kunkel, G., Zhang, Z., Deng, J. M., Behringer, R. R., de Crombrugghe, B., 2002. The novel zinc finger-containing transcription factor osterix is required for osteoblast differentiation and bone formation. Cell. 108**,** 17-29.

Noden, D. M., 1991. Cell movements and control of patterned tissue assembly during craniofacial development. J Craniofac Genet Dev Biol 11, 192–213.

Nikaido, M., Kawakami, A., Sawada, A., Furutani-Seiki, M., Takeda, H., Araki, K., 2002. Tbx24, encoding a T-box protein, is mutated in the zebrafish somite-segmentation mutant fused somites. Nat Genet. 31**,** 195-9.

Nykjaer, A. and Willnow, T. E. (2002). The low-density lipoprotein receptor gene family: a cellular Swiss army knife? Trends Cell Biol 12(6), 273-80.

Ohyama, Y., Nifuji, A., Maeda, Y., Amagasa, T., Noda, M., 2004. Spaciotemporal association and bone morphogenetic protein regulation of sclerostin and osterix expression during embryonic

osteogenesis. Endocrinology, 145, 4685-92.

Piloto, S., Schilling, T.F., 2010. Ovo1 links Wnt signaling with N-cadherin localization during neural crest migration. Development, 137, 1981-90.

Pinson, K.I., Brennan, J., Monkley, S., Avery, B.J. and Skarnes, W.C.,2000. An LDL-receptor-related protein mediates Wnt signalling in mice. Nature 407, 535-538

Pinto, D. and Clevers, H., 2005. Wnt control of stem cells and differentiation in the intestinal epithelium. Exp Cell Res 306(2), 357-63.

Pisharath, H., Rhee, J. M., Swanson, M. A., Leach, S. D., Parsons, M. J., 2007. Targeted ablation of beta cells in the embryonic zebrafish pancreas using E. coli nitroreductase. Mech Dev. 124**,** 218-29.

Poss, K. D., 2007. Getting to the heart of regeneration in zebrafish. Semin Cell Dev Biol. 18**,** 36-45.

Ragland, R., 3rd, Moukoko, D., Ezaki, M., Carter, P.R., Mills, J., 2005. Forearm compartment syndrome in the newborn: report of 24 cases. J Hand Surg Am 30, 997-1003.

Raible, D.W. Ragland, J.W., 2005. ReiteratedWnt and BMP signals in neuralcrest development. SeminarsinCell& DevelopmentalBiology 16, 673–682.

Rembold, M., Lahiri, K., Foulkes, N. S., Wittbrodt, J., 2006. Transgenesis in fish: efficient selection of transgenic fish by co-injection with a fluorescent reporter construct. Nat Protoc. 1**,** 1133-9.

Renn, J., Winkler, C., Schartl, M., Fischer, R., and Goerlich, R., 2006. Zebrafish and medaka as models for bone research including implications regarding space-related issues. Protoplasma 229, 209–214.

Renn, J., Winkler, C., 2009. Osterix-mCherry transgenic medaka for in vivo imaging of bone formation. Dev Dyn. 238**,** 241-8.

Renn, J., Winkler, C., 2010. Characterization of collagen type 10a1 and osteocalcin in early and mature osteoblasts during skeleton formation in Medaka. J. Appl. Ichthyol. 26, 196–201.

Reya, T., Duncan, A. W., Ailles, L., Domen, J., Scherer, D. C., Willert, K., Hintz, L., Nusse, R. and Weissman, I.L., 2003. A role for Wnt signalling in self-renewal of haematopoietic stem cells. Nature 423, 409-414.

Robu, M.E., Larson, J.D., Nasevicius, A., Beiraghi, S., Brenner, C., Farber, S.A., Ekker, S.C., 2007. p53 activation by knockdown technologies. PLoS Genet 3, e78.

Sadler, K. C., Krahn, K. N., Gaur, N. A., Ukomadu, C., 2007. Liver growth in the embryo and during liver regeneration in zebrafish requires the cell cycle regulator, uhrf1. Proc Natl Acad Sci U S A. 104**,** 1570-5.

Santagati, F., Rijli, F.M., 2003. Cranial neural crest and the building of the vertebrate head. Nat Rev Neurosci 4, 806-818.

Satoh, W., Gotoh, T., Tsunematsu, Y., Aizawa, S., Shimono, A., 2006 Sfrp1 and Sfrp2 regulate anteroposterior axis elongation and somite segmentation during mouse embryogenesis. Development 133, 989-999.

Semenov, M., Tamai, K., He, X., 2005. SOST is a ligand for LRP5/LRP6 and a Wnt signaling inhibitor. J Biol Chem 280, 26770-26775.

Sevetson, B., Taylor, S., Pan, Y., 2004. Cbfa1/RUNX2 directs specific expression of the sclerosteosis gene (SOST). J Biol Chem. 2004 279, 13849-58.

Spoorendonk, K. M., Peterson-Maduro, J., Renn, J., Trowe, T., Kranenbarg, S., Winkler, C., Schulte-Merker, S., 2008. Retinoic acid and Cyp26b1 are critical regulators of osteogenesis in the axial skeleton. Development. 135**,** 3765-74.

St Amand, T. R., Zhang, Y., Semina, E.V., Zhao, X. and Hu, Y., 2000. Antagonistic signals between BMP4 and FGF8 define the expression of Pitx1 and Pitx2 in mouse toothforming anlage. Dev Biol 217, 323–32.

St-Arnaud, R., Moir, J. M., 1993. Wnt-1-inducing factor-1: a novel G/C box-binding transcription factor regulating the expression of Wnt-1 during neuroectodermal differentiation. Mol Cell Biol 13(3), 1590-8.

Strickland, D.K., Gonias, S. L., Argraves, W. S., 2002. Diverse roles for the LDL receptor family. Trends Endocrinol Metab 13(2), 66-74.

Sutherland, M.K., Geoghegan, J.C., Yu, C., Winkler, D.G., Latham, J.A., 2004. Unique regulation of SOST, the sclerosteosis gene, by BMPs and steroid hormones in human osteoblasts. Bone. 35, 448-54.

Tam, P. P. and Trainor, P. A., 1994. Specification and segmentation of the paraxial mesoderm. Anat Embryol 189, 275–305.

Tamai, K., Semenov, M., Kato, Y., Spokony, R., Liu, C., Katsuyama, Y., Hess, F., Saint-Jeannet, J. P. and He, X., 2000. LDL-receptor-related proteins in Wnt signal transduction. Nature 407, 530-535.

Tamai, K., Zeng, X., Liu, C., Zhang, X., Harada, Y., Chang, Z. and He, X., 2004. A mechanism for Wnt Coreceptor Activation. Mol Cell 13, 149-156.

Tamura, K., Dudley, J., Nei, M., Kumar, S., 2007. MEGA4: Molecular Evolutionary Genetics Analysis (MEGA) software version 4.0. Mol Biol Evol 24, 1596-1599.

Tetsu, O., McCormick, F., 1999. Beta-catenin regulates expression of cyclin D1 in colon carcinoma cells. Nature 398, 422-426.

Thisse, C., Thisse, B., 2008. High-resolution in situ hybridization to whole-mount zebrafish embryos. Nat Protoc. 3**,** 59-69.

Vallin, J., Thuret, R., Giacomello, E., Faraldo, M. M., Thiery, J. P. and Broders, F., 2001. Cloning and characterization of three Xenopus slug promoters reveal direct regulation by Lef/beta-catenin signaling. J. Biol. Chem. 276, 30350- 30358.

van Bezooijen, R.L., ten Dijke, P., Papapoulos, S.E., Lowik, C.W., 2005. SOST/sclerostin, an osteocyte-derived negative regulator of bone formation. Cytokine Growth Factor Rev 16, 319-327.

van Eeden, F. J., Granato, M., Schach, U., Brand, M., Furutani-Seiki, M., Haffter, P., Hammerschmidt, M., Heisenberg, C. P., Jiang, Y. J., Kane, D. A., Kelsh, R. N., Mullins, M. C., Odenthal, J., Warga, R. M., Allende, M. L., Weinberg, E. S., Nusslein-Volhard, C., 1996. Mutations affecting somite formation and patterning in the zebrafish, Danio rerio. Development. 123**,** 153-64.

Van Leeuwen, F., Harryman Samos, C. and Nusse, R., 1994. Biological activity of soluble wingless protein in cultured Drosophila imaginal disc cells. Nature 368, 342–344.

Veeman, M.T., Axelrod, J.D. and Moon, R.T., 2003. A second canon. Functions and mechanisms of beta-catenin-independent Wnt signaling. Dev Cell 5, 367-377.

Verstraeten, B., Sanders, E. and Huysseune, A., 2011. Whole mount immunohistochemistry and in situ hybridization of larval and adult zebrafish dental tissues. In Kioussi, C. ed. Methods in Odontogenesis. In: Methods in Molecular Biology, Humana Press, USA (in press)

Veverka, V., Henry, A.J., Slocombe, P.M., Ventom, A., Mulloy, B., Muskett, F.W., Muzylak, M., Greenslade, K., Moore, A.R., Zhang, L., Gong, J., Qian, X., Paszty, C., Taylor, R.J., Robinson, M.K., Carr, M.D., 2009. Characterization of the structural features and interactions of sclerostin: molecular insight into a key regulator of Wnt- mediated bone formation. J Biol Chem 284, 10890–10900.

Villalobos, S. A., Hamm, J. T., Teh, S. J., Hinton, D. E., 2000. Thiobencarb-induced embryotoxicity in medaka (Oryzias latipes): stage-specific toxicity and the protective role of chorion. Aquat Toxicol. 48**,** 309-326.

Vinson, C. R., Conover, S. and Adler, P. N., 1989. A Drosophila tissue polarity locus encodes a protein containing seven potential transmembrane domains. Nature 338, 263-264.

Walker, M. B., Kimmel, C. B., 2007. A two-color acid-free cartilage and bone stain for zebrafish larvae. Biotech Histochem. 82**,** 23-8.

Walshe, J., Mason, I., 2003. Fgf signalling is required for formation of cartilage in the head. Dev Biol 264, 522-536.

Wehrli, M., Dougan, S.T., Caldwell, K., O'Keefe, L., Schwartz, S., Vaizel-Ohayon, D., Schejter, E., Tomlinson, A., DiNardo, S., 2000. arrow encodes an LDL-receptor-related protein essential for Wingless signalling. Nature 407, 527-530.

Weidauer, S.E., Schmieder, P., Beerbaum, M., Schmitz, W., Oschkinat, H., Mueller, T.D., 2009. NMR structure of the Wnt modulator protein Sclerostin. Biochem Biophys Res Commun 380, 160-165.

Wieschaus, E., Riggleman, B., 1987. Autonomous requirements for the segment polarity gene armadillo during Drosophila embryogenesis. Cell 49, 177-184.

Willert, K., Brown, J. D., Danenberg, E., Duncan, A. W., Weissman, I. L., Reya, T., Yates, J. R. 3rd and Nusse, R., 2003. Wnt proteins are lipid-modified and can act as stem cell growth factors. Nature 423(6938), 448-52.

Winkler, D.G., Sutherland, M.K., Geoghegan, J.C., Yu, C., Hayes, T., Skonier, J.E., Shpektor, D., Jonas, M., Kovacevich, B.R., Staehling-Hampton, K., Appleby, M., Brunkow, M.E., Latham, J.A., 2003. Osteocyte control of bone formation via sclerostin, a novel BMP antagonist. EMBO J. 23, 6267-76.

Witten, P. E., Villwock, W., Peters, N. and Hall, B. K., 2000. Bone resorption and bone remodelling in juvenile carp, Cyprinus carpio L. J Appl Ichthyol 16, 254–261.

Witten, P. E., Hanson, A. and Hall, B. K., 2001. Features of mono- and multinucleated bone resorbing cells of the zebrafish Danio rerio and their contribution to skeletal develoment, remodeling, and growth. J Morphol 250, 197–207.

Wodarz, A., Nusse, R., 1998. Mechanisms of Wnt signaling in development. Annu Rev Cell Dev Biol 14, 59-88.

Wu, J., Yang, J., Klein, P.S., 2005. Neural crest induction by the canonical Wnt pathway can be dissociated from anterior-posterior neural patterning in Xenopus. Developmental biology 279, 220-232.

Yadav, V. K., Ryu, J. H., Suda, N., Tanaka, K. F., Gingrich, J. A., Schütz, G., Glorieux, F. H., Chiang, C. Y., Zajac, J.D., Insogna, K.L., Mann, J. J., Hen, R., Ducy, P., Karsenty, G., 2008. Lrp5 controls bone formation by inhibiting serotonin synthesis in the duodenum. Cell. 135, 825-37.

Yasuda, T., Yoshimoto, M., Maeda, K., Matsumoto, A., Maruyama, K., Ishikawa, Y., 2008. Rapid and simple method for quantitative evaluation of neurocytotoxic effects of radiation on developing medaka brain. J Radiat Res (Tokyo). 49**,** 533-40.

Zhao, X. F., Ellingsen, S., Fjose, A., 2009. Labelling and targeted ablation of specific bipolar cell types in the zebrafish retina. BMC Neuroscience 10, 107.

Zeng, X., Tamai, K., Doble, B., Li, S., Huang, H., Habas, R., Okamura, H., Woodgett, J., He, X., 2005. A dual-kinase mechanism for Wnt co-receptor phosphorylation and activation. Nature 438(8), 873-877.

Zorn, A. M., 2001. Wnt signalling: antagonistic Dickkopfs. Curr Biol 11(15), R592 5.